Journal of Medicinal Chemistry

pubs.acs.org/jmc

Article

# Discovery of LT-1339−553 as a Potent RIPK1 Inhibitor for Schistosomiasis-Induced Hepatic Fibrosis

*Published as part of Journal of Medicinal Chemistry special issue "Celebrating the 90th Anniversary of China Pharmaceutical University".*

Ju-Lu Lu,[#] Qin-Di He,[#] Yi-Han Yang,[#] Jing-Ping Li,[#] Si-Rui Mo, Li Liang, Ya-Qi Zhang, Si-Ming Jia, Zi-Tian Cheng, Jie Cheng, Pei Yang, Hong-Mei Li, Tao Lu, Ya-Dong Chen,* Li-Jun Song,* and Shuai Lu*

Cite This: https://doi.org/10.1021/acs.jmedchem.5c03775

Read Online

ACCESS | Metrics & More | Article Recommendations | Supporting Information

**ABSTRACT:** Hepatic fibrosis, a key pathological driver of chronic liver disease progression, lacks effective targeted therapies. Receptor-interacting protein kinase 1 (RIPK1) has emerged as a promising therapeutic target. Herein, we developed a highly potent and selective RIPK1 inhibitor, LT-1339−553 (**30**), through structure-based optimization. Compound **30** exhibited potent RIPK1 inhibition ($IC_{50}$ = 4.32 nM) and cellular antinecroptotic activity ($EC_{50}$ = 14.43 nM). In a murine model of hepatic fibrosis, **30** significantly alleviated liver injury, inflammation, and collagen deposition. Mechanistic studies revealed that its antifibrotic effects were associated with suppression of the AKT/PI3K/NF-κB and IL-17 pathways. Furthermore, **30** demonstrated good oral bioavailability and a favorable safety profile. These results position **30** as a promising candidate for the treatment of hepatic fibrosis.

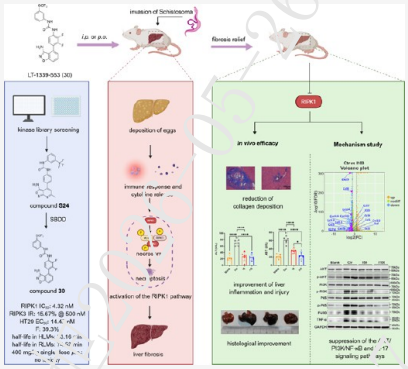

## 1. INTRODUCTION

Chronic liver injury culminates in hepatic fibrosis, a pathological state characterized by excessive extracellular matrix (ECM) deposition that can progress to cirrhosis and organ failure.[1] As a pathological repair response to chronic inflammatory injury, hepatic fibrosis represents a critical transitional stage in the progression of various chronic liver diseases toward irreversible cirrhosis and hepatocellular carcinoma.[2] This condition is frequently complicated by portal hypertension, ascites, and other sequelae that substantially compromise patient health.[3] Although early stage hepatic fibrosis is theoretically reversible, no targeted therapy is currently approved for clinical use, underscoring the urgent need to identify novel drug targets and therapeutic agents.[4] Against this backdrop, elucidating the molecular drivers of fibrosis has become a research priority. In recent years, necroptosis, a lytic and pro-inflammatory form of programmed cell death distinct from apoptosis, has emerged as a critical mechanism linking tissue injury, inflammation, autoimmunity and fibrotic progression.

Necroptosis is typically initiated under conditions of apoptotic suppression, upon engagement of death receptors (e.g., TNFR1) or pattern recognition receptors (e.g., TLR3/4).[5,6] This triggers a well-defined signaling cascade centered on receptor-interacting protein kinase 1 (RIPK1). Through its kinase activity, RIPK1 associates with RIPK3 to form the "necrosome" complex, which in turn phosphorylates and activates mixed lineage kinase domain-like protein (MLKL). Activated MLKL oligomerizes, translocate to the plasma membrane, and induce membrane permeabilization, leading to the release of damage-associated molecular patterns (DAMPs) and the instigation of potent local and systemic inflammation.[7−9] The resulting persistent inflammatory microenvironment acts as a key driver of fibrogenesis.[10] In the liver, sustained release of pro-inflammatory cytokines and growth factors (e.g., TNF-$\alpha$, IL-1$\beta$, and TGF-$\beta$) from immune cells chronically activates hepatic stellate cells (HSCs).[11] Once activated, HSCs undergo transdifferentiation into myofibroblasts,[12] which exhibit upregulated ECM synthesis (e.g., collagen) alongside suppressed matrix metalloproteinase (MMP) activity.[13] This imbalance promotes net ECM accumulation, ultimately culminating in fibrosis.[14] Thus, necroptosis potentially represents a key pathogenic driver of fibrosis, primarily through its role in amplifying inflammation. Given their pivotal roles in necroptosis, RIPK1 and RIPK3 have emerged as attractive

Received: December 22, 2025
Revised: April 12, 2026
Accepted: May 4, 2026

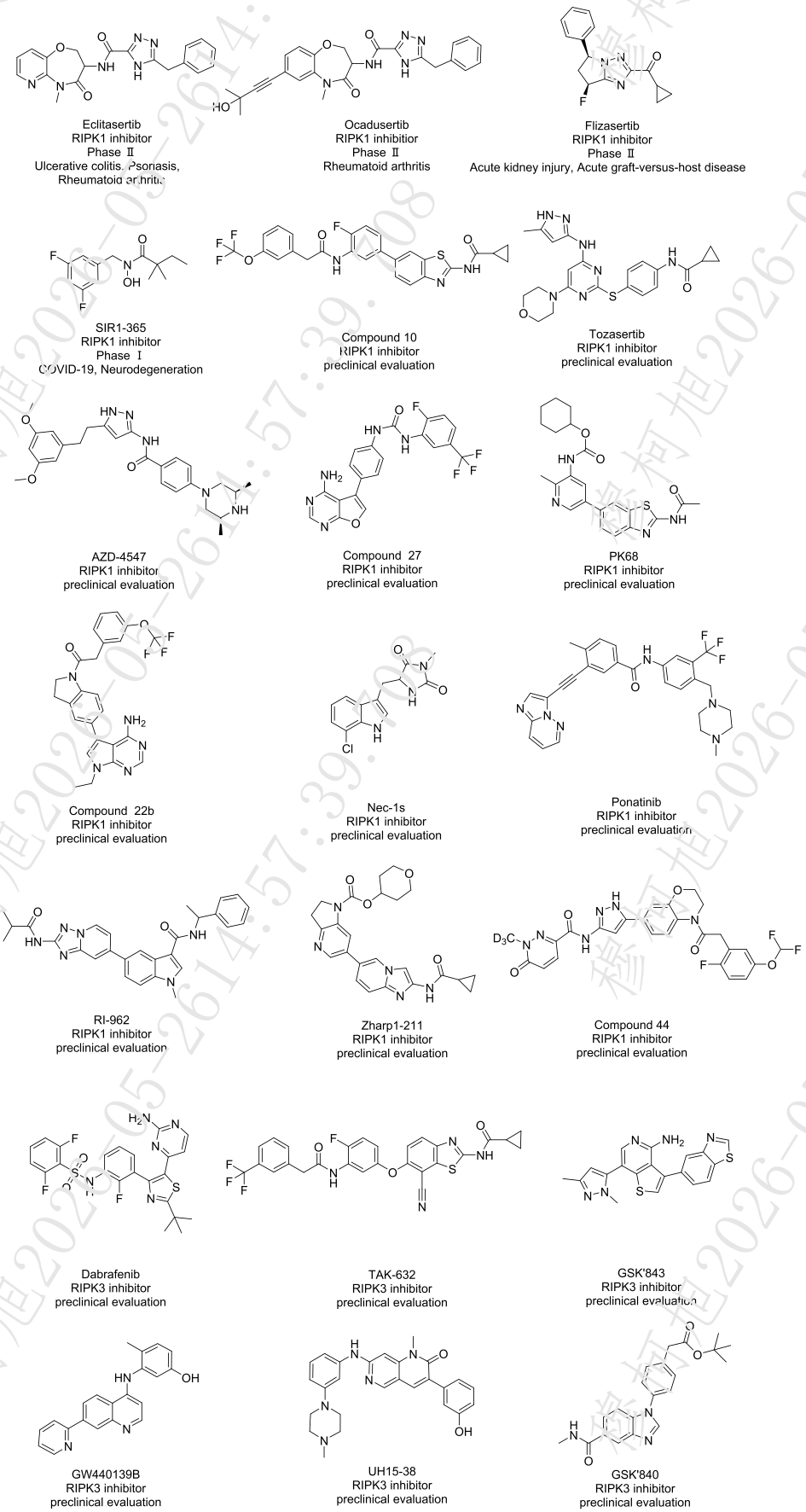


**Figure 1.** Chemical structures of representative RIPK1 and RIPK3 inhibitors.[17−28]



https://doi.org/10.1021/acs.jmedchem.5c03775
J. Med. Chem. XXXX, XXX, XXX−XXX

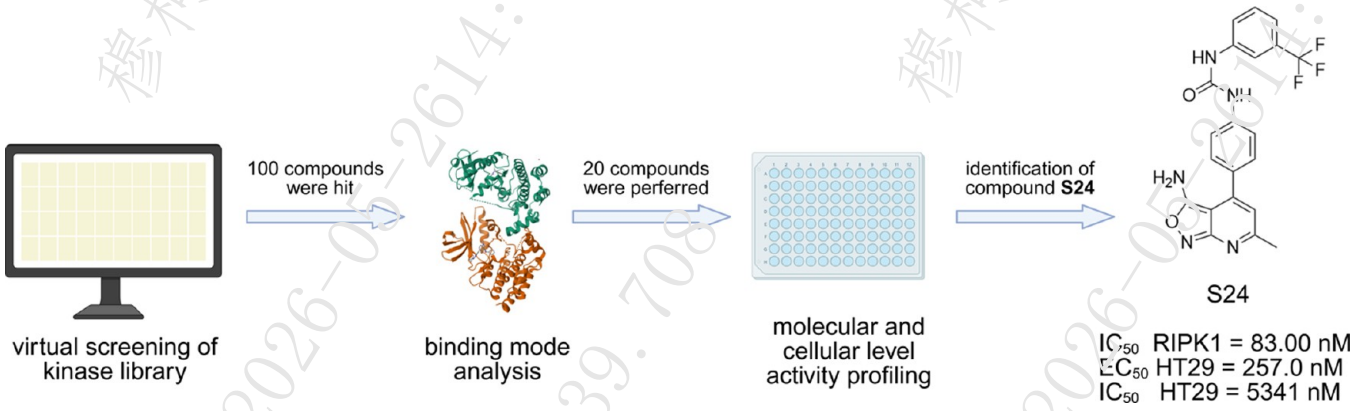


**Figure 2.** Identification of compound **S24**.

therapeutic targets for a range of human autoimmune and inflammatory diseases, and a variety of RIPK1 and RIPK3 inhibitors are advanced into clinical trials or under preclinical evaluation[15,16] (Figure 1).

In experimental models of schistosomiasis, infection induces a pronounced necroptotic response in the liver, which is characterized by the activation of inflammation and necroptosis pathway.[29,30] The parasitic pathogen Schistosoma illustrates this mechanism: after infecting a host, the worms mature and reside in the mesenteric veins, where their eggs are deposited in the liver. This deposition elicits a robust immune response, recruiting macrophages, T cells, and eosinophils to encapsulate the eggs and form hepatic inflammatory granulomas. Subsequent tissue repair processes drive the development of hepatic fibrosis.[31] As a chronic, naturally infectious pathogenic process, schistosome-induced hepatic fibrosis represents a highly relevant and valuable model for studying fibrotic liver disease.[32] Moreover, our previous work has directly implicated RIPK3-mediated necroptosis in the pathogenesis of this condition, where genetic ablation of RIPK3 was shown to significantly ameliorate hepatic granulomatous inflammation and collagen deposition in infected mice, thereby validating the necroptosis pathway as a promising therapeutic target for antifibrotic therapy.[29] However, RIPK1 serves as the pivotal upstream master regulator of this cascade, integrating multiple death signals and acting as the primary initiator of necroptosis. Strategies directly inhibiting the downstream kinase RIPK3, while effective in some contexts, face potential safety challenges, such as the unintended induction of caspase-8-dependent apoptosis.[33] Targeting RIPK1 offers a more strategic approach to intercept the necroptotic cascade at its origin, potentially achieving broad efficacy with a reduced risk of off-target effects. Furthermore, RIPK1 is a key mediator of both apoptosis and inflammatory signaling, making it an attractive target with broad therapeutic implications.[34] We herein present our efforts to explore this upstream, targeted RIPK1 strategy for treating schistosomiasis-induced hepatic fibrosis.

In pursuit of novel RIPK1 inhibitors, we performed virtual screening of an internal kinase-focused compound library. The top 100 candidates were selected based on docking scores, and their binding modes were systematically analyzed in comparison to known RIPK1 inhibitors. Compounds exhibiting both structural novelty and interaction patterns consistent with effective inhibition were prioritized. From this set, 20 compounds with favorable profiles were advanced to kinase activity assays. These efforts led to the identification of compound **S24** (Figure 2), which demonstrated an $IC_{50}$ of 83 nM against RIPK1. In a TNF$\alpha$/Smac-mimetic/z-VAD-FMK (TSZ)-induced necroptosis model in HT29 cells, **S24** exhibited potent protective effects against necroptosis ($EC_{50}$ = 257 nM) and minimal cytotoxicity (proliferation inhibition $IC_{50}$ = 5341 nM). Owing to this promising activity and safety profile, **S24** was selected as a lead compound for further optimization. Guided by detailed binding mode analysis, we designed a series of benzo[*d*]isoxazol-3-amine derivatives with high RIPK1 inhibitory activity. Among these, compound **39** (**LT-1339−553**) showed particularly potent antinecroptotic effects in the TSZ-induced HT29 cell model. Furthermore, *in vivo* administration of **30** to schistosome-infected mice via both intraperitoneal injection and oral gavage, significantly reduced hepatic inflammation levels and effectively attenuated the degree of hepatic fibrosis, through modulations of RIPK1 related necroptosis and the following AKT/PI3K/NF-$\kappa$B and IL-17 signaling pathways. These findings lay a solid scientific foundation for expanding the application of RIPK1 inhibitors into the treatment of liver fibrosis.

## 2. CHEMISTRY

Synthesis of compound **S24** followed previously reported procedures.[35] The synthetic routes for compounds **1**−**10** are outlined in Scheme 1. Suzuki coupling of the corresponding aryl bromides with 4-(4,4,5,5-tetramethyl-1,3,2-dioxaborolan-2-yl)-aniline afforded key intermediates **B-1a**−**B-3a**. Subsequent urea formation between intermediates **B-1a**−**B-3a** and the corresponding primary amines or isocyanates yielded target compounds **1**−**7**, **9**, and **10**. For the synthesis of compound **8**, intermediate **B-1** was first reacted with *tert*-butyl 4-aminopiperidine-1-carboxylate to form the urea intermediate **B-8b**, which was then treated with trifluoroacetic acid to remove the *Boc* protecting group, affording the compound **8**.

Synthetic routes for target compounds **11**, **12**, **14**, **17**, **18**, and **21**−**38** are presented in Scheme 2. Key intermediates **B-11a**, **B-12a**, **B-14a**, **B-17a**, **B-18a**, and **B-21a**−**B-38a** were synthesized via Miyaura borylation of the corresponding aryl bromides with bis(pinacolato)diboron. These boronic ester intermediates underwent Suzuki coupling with 4-bromobenzo[*d*]isoxazol-3-amine to afford intermediates **B-11b**, **B-12b**, **B-14b**, **B-17b**, **B-18b**, and **B-21b**−**B-38b**. Finally, reaction of these intermediates with 3-(trifluoromethyl)aniline yielded the corresponding ureas, providing target compounds **11**, **12**, **14**, **17**, **18**, and **21**−**38**.

Synthetic routes for target compounds **13** and **15** are depicted in Scheme 3. Nucleophilic substitution of *Boc*-protected *para*-


https://doi.org/10.1021/acs.jmedchem.5c03775
J. Med. Chem. XXXX, XXX, XXX−XXX

**Scheme 1. Synthetic Route of Compounds 1−10**[a]

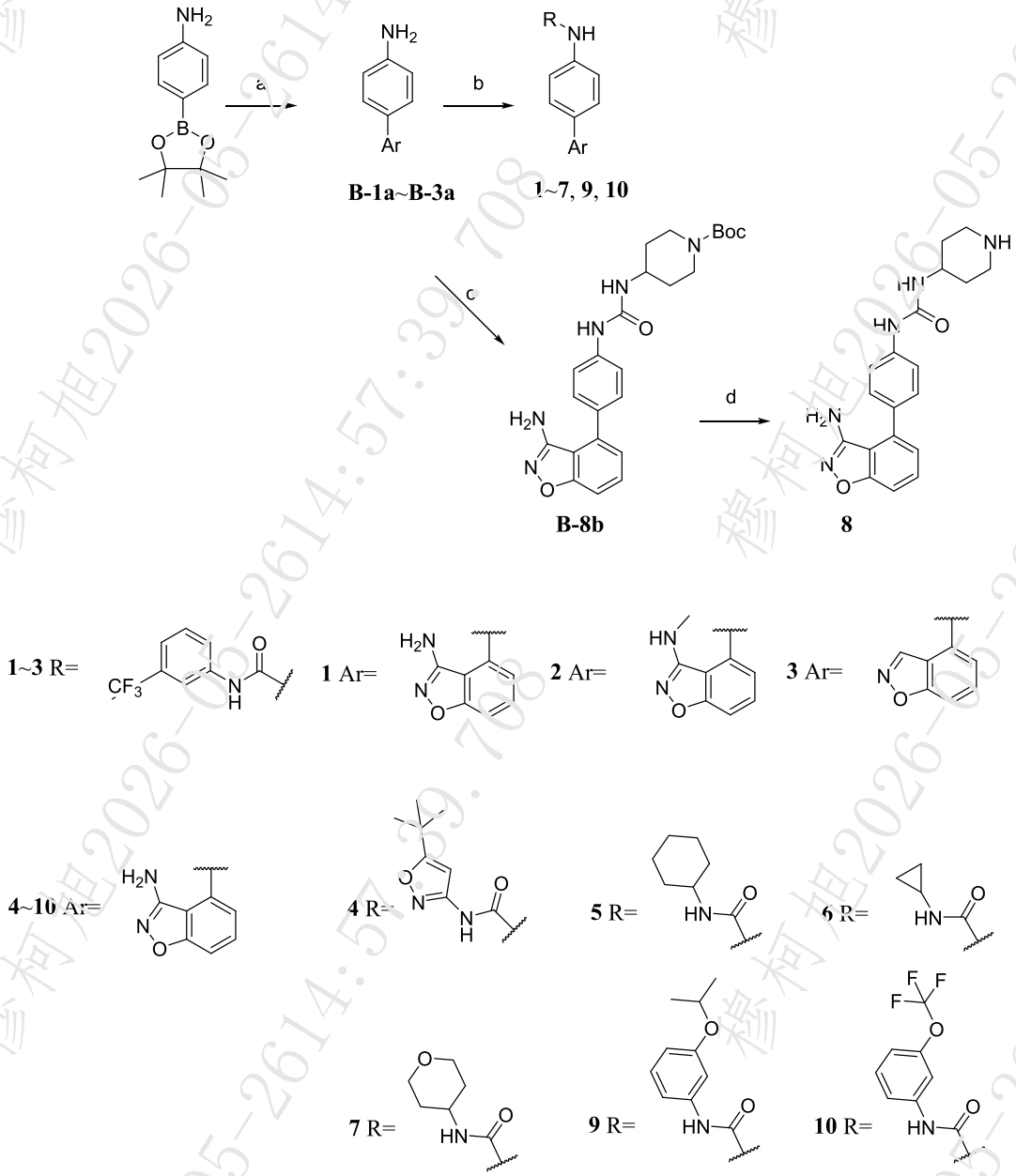


[a]Reagents and conditions: (a) corresponding aryl bromide, $Pd(dppf)Cl_2$, $Na_2CO_3$, 1,4-dioxane/$H_2O$ (5/1), reflux; (b) 1-isocyanato-3-(trifluoromethyl)benzene, DCM, $Et_3N$, rt (for 1−3); corresponding primary amine, triphosgene, DCM, $Et_3N$, rt (for 4−7, 9, 10); (c) 3-(trifluoromethyl)phenyl isocyanate, DCM, $Et_3N$, rt; (d) TFA, DCM, rt.

aminophenol or *meta*-aminophenol with 2,6-difluorobenzonitrile afforded intermediates **B-13a** and **B-15a**, respectively. Reaction with acetonenadione yielded intermediates **B-13b** and **B-15b**, which underwent *Boc* deprotection with trifluoroacetic acid to provide **B-13c** and **B-15c**. Urea formation with 3-(trifluoromethoxy)aniline furnished compounds **13** and **15.**

Synthesis of compound **16** (Scheme 4) commenced with Suzuki coupling between 2-(4-(4,4,5,5-tetramethyl-1,3,2-dioxaborolan-2-yl)phenyl)acetic acid and 4-bromobenzo[*d*]isoxazol-3-amine, generating intermediate **B-16a**. Amide coupling of **B-16a** with 3-(trifluoromethoxy)aniline afforded **16.**

Synthetic routes for compounds **19** and **20** are depicted in Scheme 5. Bromination of 2,3-dihydro-1*H*-inden-4-amine with *N*-bromosuccinimide gave **B-19a**. Miyaura borylation of **B-19a** yielded boronic ester **B-19b**, which underwent Suzuki coupling with 4-bromobenzo[*d*]isoxazol-3-amine to afford **B-19c**. Urea formation of **B-19c** with 3-(trifluoromethoxy)aniline yielded **19**. Compound **20** was synthesized analogously from 7-amino-2,3-dihydro-1*H*-inden-1-one.

## 3. RESULT

### 3.1. Design Rationale

Molecular docking analysis based on the reported RIPK1 crystal structure (PDB code: 4NEU) revealed that the 6-methylisoxazolo[3,4-*b*]pyridin-3-amine fragment of lead compound **S24** occupies the hinge region (Figure 3A). The nitrogen of isoxazole ring acts as a hydrogen bond acceptor from the backbone NH of Met95, while the amino group serves as a


https://doi.org/10.1021/acs.jmedchem.5c03775
J. Med. Chem. XXXX, XXX, XXX−XXX

**Scheme 2. Synthetic Route of Compounds 11, 12, 14, 17, 18, and 21−38**[a]

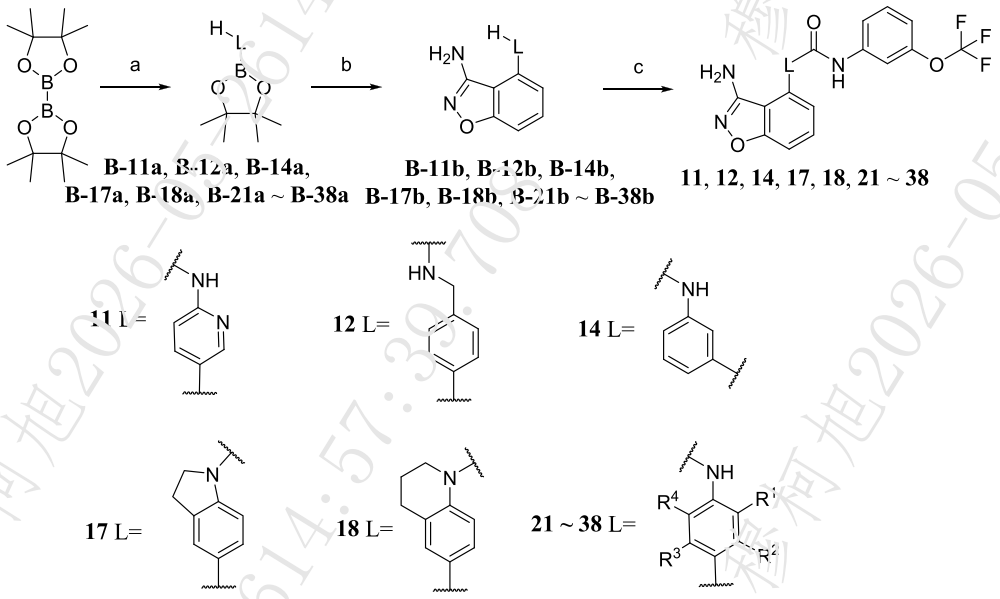


**21** $R^1$=$CH_3$ $R^2$=H $R^3$=H $R^4$=H **22** $R^1$=H $R^2$=$CH_3$ $R^3$=H $R^4$=H **23** $R^1$=F $R^2$=H $R^3$=H $R^4$=H
**24** $R^1$=Cl $R^2$=H $R^3$=H $R^4$=H **25** $R^1$=H $R^2$=Cl $R^3$=H $R^4$=H **26** $R^1$=$OCH_3$ $R^2$=H $R^3$=H $R^4$=H
**27** $R^1$=H $R^2$=CN $R^3$=H $R^4$=F **28** $R^1$=H $R^2$=F $R^3$=F $R^4$=H **29** $R^1$=$CH_3$ $R^2$=$CH_3$ $R^3$=H $R^4$=H
**30** $R^1$=F $R^2$=F $R^3$=H $R^4$=H **31** $R^1$=F $R^2$=H $R^3$=H $R^4$=F **32** $R^1$=H $R^2$=F $R^3$=F $R^4$=H
**33** $R^1$=H $R^2$=F $R^3$=H $R^4$=F **34** $R^1$=F $R^2$=Cl $R^3$=H $R^4$=H **35** $R^1$=Cl $R^2$=Cl $R^3$=H $R^4$=H
**36** $R^1$=$CH_3$ $R^2$=F $R^3$=H $R^4$=H **37** $R^1$=H $R^2$=F $R^3$=H $R^4$=$CH_3$ **38** $R^1$=H $R^2$=$CH_3$ $R^3$=H $R^4$=F

[a]Reagents and conditions: (a) corresponding aryl bromide, $Pd(dppf)Cl_2$, AcOK, dry 1,4-dioxane, reflux; (b) 4-bromobenzo[d]isoxazol-3-amine, $Pd(dppf)Cl_2$, $Na_2CO_3$, 1,4-dioxane/$H_2O$ (5/1), reflux; (c) 3-(trifluoromethoxy)aniline, triphosgene, DCM, $Et_3N$, rt.

**Scheme 3. Synthetic Route of Compounds 13 and 15**[a]

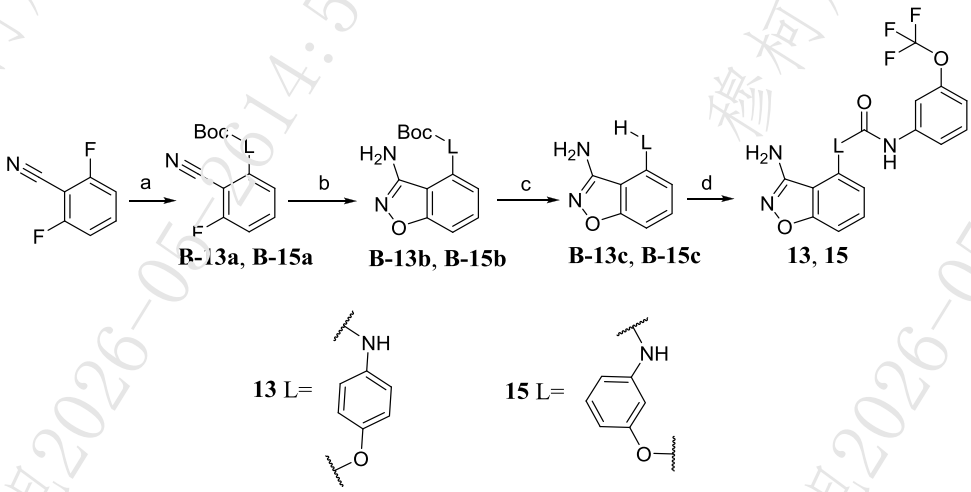


[a]Reagents and conditions: (a) corresponding phenol derivative, dry DMF, KOH, rt; (b) acetomenadione, *t*-BuOK, DMF, rt; (c) TFA, DCM, rt; (d) 3-(trifluoromethoxy)aniline, triphosgene, TEA, DCM, rt.

donor to the carbonyl oxygen of Glu93. The urea moiety extends into the channel region, forming three hydrogen bonds with the backbone NH of Asp156 and the carboxylate side chain of Glu63, respectively. The trifluoromethylphenyl group occupies the hydrophobic back pocket (Figure 3B). Hence, **S24** may adopt a Type II kinase-inhibitor binding mode. Guided by this binding pose, we structurally modified **S24** to develop novel chemotypes through stepwise investigating alternative moieties that can interact with the hinge, channel region and hydrophobic pocket of RIPK1. *In vitro* RIPK1 inhibition (ADP-Glo assay), antinecroptotic activity (TSZ-induced HT29 model) and cytotoxicity (HT29 proliferation) of the target compounds were evaluated for the collective consideration.

Initially, we replaced the isoxazolo[3,4-*b*]pyridine moiety of **S24** with its bioisosteres, yielding compounds **1**−**3**. As shown in Table 1, Compound **1** demonstrated the moderately increased


https://doi.org/10.1021/acs.jmedchem.5c03775
J. Med. Chem. XXXX, XXX, XXX−XXX

**Scheme 4. Synthetic Route of Compound 16**[a]

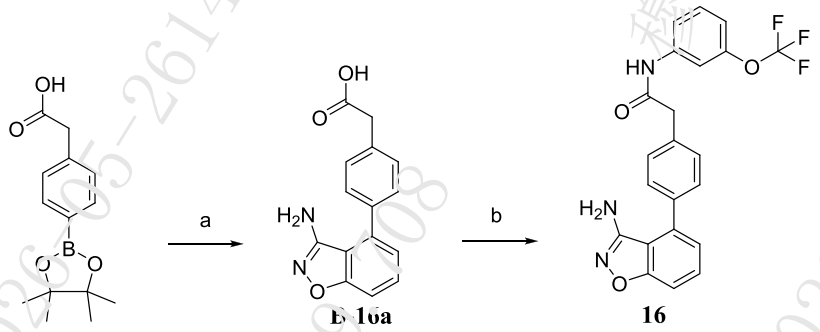


[a]Reagents and conditions: (a) 4-bromobenzo[d]isoxazol-3-amine, Pd(dppf)$Cl_2$, $Na_2CO_3$, 1,4-dioxane/$H_2O$ (5/1), reflux; (b) 3-(trifluoromethoxy)aniline, HATU, DIPEA, DMF, rt.

**Scheme 5. Synthetic Route of Compounds 19 and 20**[a]

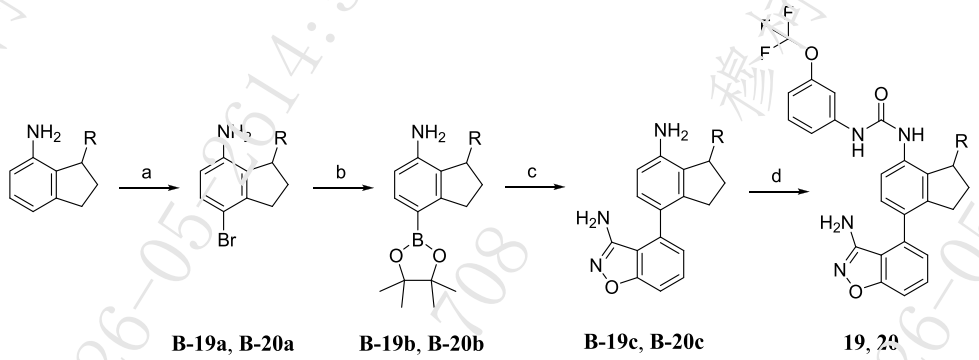


**19** R=H **20** R=carbonyl group

[a]Reagents and conditions: (a) NBS, DCM, rt; (b) $B_2pin_2$, Pd(dppf)$Cl_2$, AcOK, dry 1,4-dioxane, reflux, (c) bromobenzo[d]isoxazol-3-amine, Pd(dppf)$Cl_2$, $Na_2CO_3$, 1,4-dioxane/$H_2O$ (5/1), reflux; (d) 3-(trifluoromethoxy)aniline, triphosgene, DCM, $Et_3N$, rt.

RIPK1 inhibitory and comparable antinecroptotic potency (HT29 $EC_{50}$ = 256.6 nM) as **S24** did. Inversely, modifications that impaired either the hydrogen-bond donating (**2**) or accepting (**3**) potential of the original moiety significantly decreased both RIPK1 inhibition and antinecroptotic activity, underscoring the necessity of forming multiple hydrogen bonds with the hinge region. This comparable activity is structurally rationalized, as the binding modes of **S24** and **1** from molecular docking are nearly superimposed (Figure 3C), with both compounds forming analogous hydrogen-bonding interactions and occupying the hydrophobic pocket in a highly similar manner. Given the lower cytotoxicity and more feasible synthetic route of **1**, the benzo[*d*]isoxazol-3-amine moiety were selected for interacting hinge region of RIPK1.

Next, we investigated the substituents bound in the hydrophobic back pocket (Table 2). Compound **4** with a *tert*-butyl oxazole group exhibited potent RIPK1 kinase inhibition ($IC_{50}$ = 2.716 nM), but it had no cellular antinecroptotic activity. To probe this disconnect, we calculated its in silico ADME properties (Table S1). **4** displayed a high Membrane dG Insert value (18.51 kcal/mol) and a low predicted Caco-2 permeability (QPPCaco = 72.0 nm/s), which strongly supports the hypothesis that its lack of cellular activity stems from poor passive membrane diffusion due to its high hydrophobicity. Incorporation of a six-member alicyclic group (**5**) led to a sharp decrease in RIPK1 inhibition. Reducing the size of the aliphatic ring (**6**), or introducing a heteroatom (O for **7**, N for **8**) into the cyclohexyl group, also abolished kinase inhibition, suggesting a superiority of aromatic group in this back pocket. We then explored the effects of *m*-trifluoromethyl of **1**. Compound **9** with a *m*-isopropoxyl group showed moderate RIPK1 inhibition ($IC_{50}$ = 106.5 nM), but diminished cellular activity. In contrast, compound **10** (trifluoromethoxy) maintained comparable kinase-inhibition potency to **1** ($IC_{50}$ = 72 nM vs 66 nM) and robust cellular antinecroptotic activity ($EC_{50}$ = 380.4 nM vs 256.6 nM); while it exhibited lower cytotoxicity ($IC_{50}$ = 7178 nM vs 3963 nM) than **1**. Based on the balanced activity and cytotoxicity profile, **10** was selected for further optimization.

We then fixed core structure of compound **10** and systematically investigated the linker moiety bound to the channel region of RIPK1 (Table 3). Replacement of the phenyl ring with pyridine (**11**) afforded potent RIPK1 kinase inhibition ($IC_{50}$ = 8.971 nM) but significantly reduced cellular antinecroptotic activity ($EC_{50}$ = 988.7 nM vs 380.4 nM). In silico ADME predictions revealed that **11** exhibits lower passive permeability (QPPCaco = 141.1 nm/s) and a higher membrane insertion energy barrier (Membrane dG Insert = 18.81 kcal/mol) compared to the more permeable **10** (QPPCaco = 215.6 nm/s, Membrane dG Insert = 14.18 kcal/mol, Table S1). These data support the hypothesis that the introduction of a pyridine nitrogen increases molecular polarity, thereby compromising membrane permeability and cellular efficacy. Subsequent


https://doi.org/10.1021/acs.jmedchem.5c03775
J. Med. Chem. XXXX, XXX, XXX−XXX

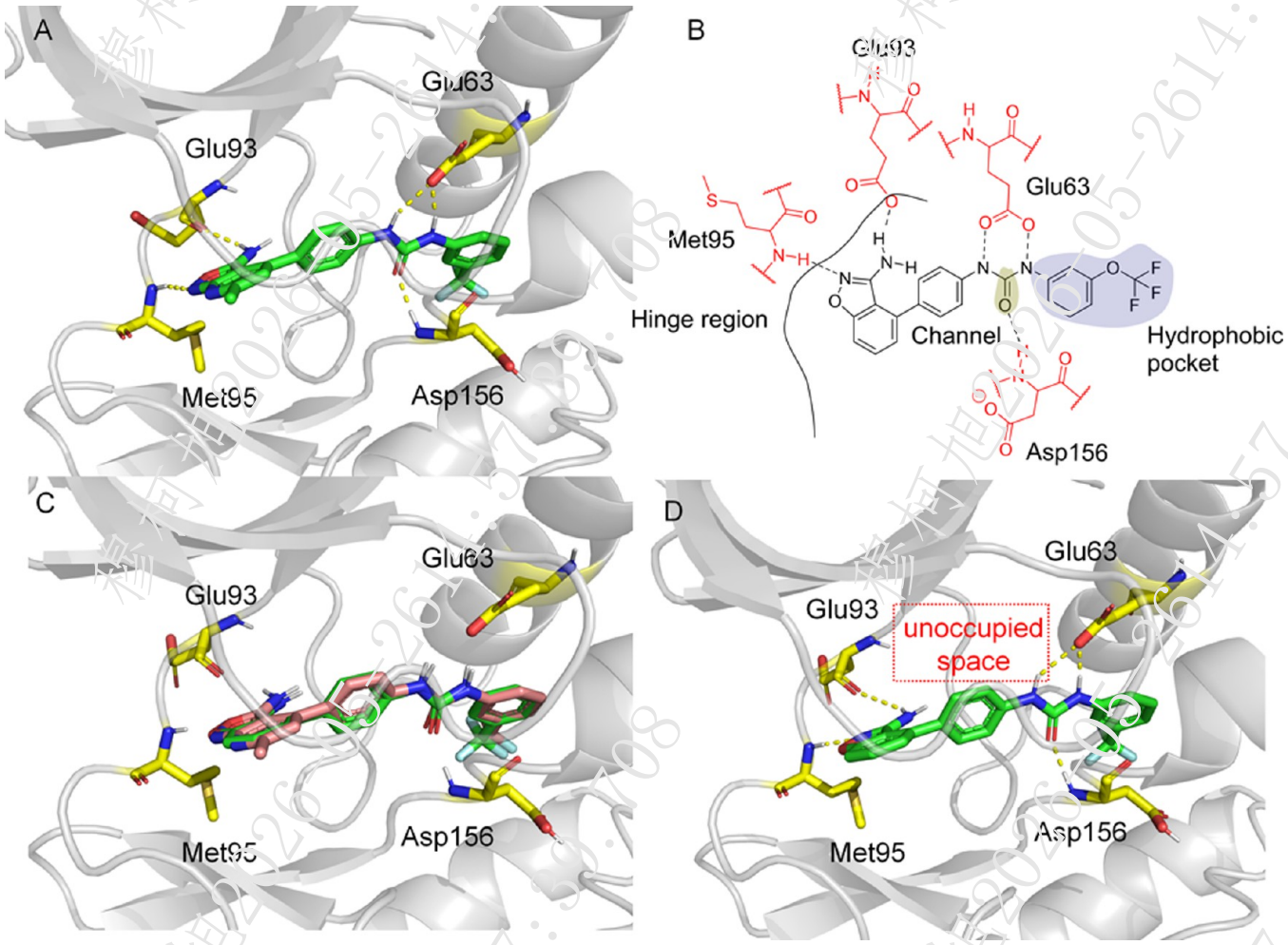


**Figure 3.** Molecular docking prediction of the binding mode of compound **S24** and **1** to RIPK1 (PDB: 4NEU). (A) Three-dimensional representation of the docking pose within the active site, where compound **S24** is depicted as a green thick solid line, key residues forming hydrogen bonds are shown in yellow thick solid lines, and hydrogen bonds are indicated by yellow dashed lines. (B) Two-dimensional schematic of the specific molecular interactions, showing key residues. (C) Structural alignment of the proposed binding modes for compound **S24** and compound **1** docked into RIPK1. In the overlay, compound **1** is shown as a pink thick solid line, and compound **S24** as a green thick solid line. (D) Molecular docking result of compound **1** reveals the presence of an unoccupied space adjacent to the linker moiety of the compound (all binding modes discussed hereafter are for complexes with RIPK1, unless explicitly indicated).

investigation into the linker length (**12** and **13**) revealed that both exhibited poor RIPK1 kinase inhibitory activity and a complete loss of cellular activity, indicating stringent requirements for the chain length of the linker moiety. We then continued our study on phenyl substitution patterns (**14** and **15**). The results showed that **14** exhibited a complete loss of RIPK1 inhibitory ability. In contrast, although **15** retained enzymatic potency comparable to **10**, its cellular inactivity aligned with inferior permeability metrics (QPPCaco = 164.7 nm/s; Membrane dG Insert = 14.56 kcal/mol, Table S1), further highlighting the necessity of balanced physicochemical properties for cellular efficacy. Changing the N1 of the urea to C (**16**), despite leading to an improvement in RIPK1 kinase inhibitory activity, resulted in a complete loss of cellular activity, possibly due to the elevated flexibility of the linker.

Enlightened by the insights from molecular docking, that an unoccupied space is close to the linker moiety (Figure 3D), we designed four fused-ring derivatives (**17**–**20**). Fusing $N^1$ with the adjacent phenyl ring leads to distinguishing effects on the biological activity. Compared to **10**, formation of five-membered ring (**17**) slightly enhanced cellular antinecroptotic activity ($EC_{50}$ = 282.2 nM vs 380.4 nM) but weakened kinase inhibition ($IC_{50}$ = 111 nM vs 72 nM). In the contrast, cyclization to six-membered ring (**18**) caused drastically reduced kinase inhibitory activity and a complete loss of antinecroptotic efficacy, suggesting that the larger ring made significant steric hindrance with the channel region of RIPK1. Direct fusing an extra five-membered ring to the phenyl ring (**19** and **20**) retained RIPK1-inhibition activity, but obviously impaired the cellular efficacy, likely due to the unfavorable contribution to membrane permeability. Collectively, these results underscore the critical sensitivity of the channel region to structural perturbations, and thus the original linker moiety remained unchanged.

Finally, we explored various substitution patterns on the central benzene ring. As summarized in the table, we first investigated the SAR of monosubstituted benzene rings with different functional groups, affording compounds **21**–**28** (Table 4). Biological data indicated that monomethyl substitution markedly improved RIPK1 kinase inhibitory activity but had only a modest effect on cellular antinecroptotic activity (**21** and **22**). Monofluoro substitution (**23** and **24**) demonstrated a


https://doi.org/10.1021/acs.jmedchem.5c03775
J. Med. Chem. XXXX, XXX, XXX−XXX

**Table 1. Structures of Compounds S24, 1−3, and Their Inhibitory Activities against RIPK1 Kinase, Antinecroptotic Effects, and Cytotoxicity**

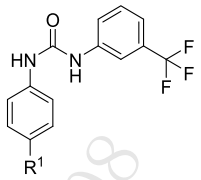

| Number | $R^1$ | RIPK1 $IC_{50}$ (nM) [a] | $EC_{50}^{HT29}$ (nM) [b] | $IC_{50}^{HT29}$ (nM) [a] |
|---|---|---|---|---|
| 1 |  | 66 ± 4.19 | 256.6 ± 21.23 | 3963 ± 565 |
| 2 |  | 568.9 ± 97.1 | > 10000 | 6940 ± 629 |
| 3 |  | > 10000 | > 10000 | > 10000 |
| S24 | 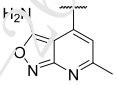 | 83.0 ± 5.17 | 257.0 ± 17.3 | 5341 ± 334 |
| GSK-2982772 | / | 16.3 ± 2.60 | 10.96 ± 4.15 | > 10000 |

[a]The $IC_{50}$ values are expressed as the mean ± SD from three independent experiments. [b]The $EC_{50}$ values are expressed as the mean ± SD from three independent experiments.

certain degree of enhancement in both RIPK1 kinase inhibition and antinecroptotic potency. Notably, **23** ($IC_{50}$ = 72 nM) possessed kinase inhibitory activity equivalent to that of **10**, while exhibiting an 8-fold improvement in antinecroptotic efficacy ($EC_{50}$ = 49 nM vs 380.4 nM, respectively), suggesting that the incorporation of a fluorine atom may exert a more positive effect on cellular activity. In contrast, although **24** displayed significant RIPK1 kinase inhibitory activity, its cellular activity was notably weak. Monochloro substitution also evidently exhibited RIPK1 inhibitory activity, along with a slight increase in antinecroptotic potency, but was generally accompanied by stronger cytotoxic effects (**25** and **26**). Similarly, the introduction of a methoxy group led to reduced RIPK1 kinase inhibitory activity and a complete loss of antinecroptotic efficacy (**27**). Considering its size and position, we postulate that it may sterically clash with residues in the channel region, preventing the urea moiety from adopting its optimal conformation; additionally, the increased polar surface area introduced by the methoxy group likely compromised membrane permeability, resulting in the complete loss of its cellular activity. Although the cyano group (**28**) maintained RIPK1 kinase inhibitory activity and enhanced antinecroptotic potency by 2-fold, it exhibited significant cytotoxicity.

Subsequently, we investigated combinations of methyl, fluorine, and chlorine atoms that are favorable for antinecroptotic activity, affording compounds **29**−**38**. Among them, the dimethyl-substituted analog (**29**) maintained kinase inhibitory activity but exhibited significantly reduced cellular activity ($EC_{50}$ = 2781 nM). Compared with **10**, the ipsilateral difluoro-substituted **30** showed a 26-fold increase in antinecroptotic potency ($EC_{50}$ = 14.43 nM vs 380.4 nM) and a 17-fold enhancement in kinase inhibition ($IC_{50}$ = 4.32 nM vs 72 nM), accompanied by a modest rise in cytotoxicity ($IC_{50}$ = 1760 nM vs 7178 nM). The marked improvement in cellular activity for **30** can be attributed, at least in part, to enhanced membrane permeability. In silico predictions indicate that the *ortho*-difluoro substitution improves key permeability metrics compared to the unsubstituted **10** (QPPCaco: 246.4 vs 215.6 nm/s; Membrane dG Insert: 13.47 vs 14.18 kcal/mol, Table S1). This comparison further underscores the importance of balancing target potency with favorable physicochemical properties for cellular activity. The beneficial "fluoro-effect" observed for **30** may result from the fluorine atoms lowering the $pK_a$ of adjacent basic groups and increasing the overall lipophilicity of the molecule, a conclusion supported by numerous reports.[36,37] In contrast, other difluoro-substituted combinations (**31**−**33**) retained RIPK1 kinase inhibitory activity but failed to significantly improve cellular activity. Replacing one fluorine atom in **30** with chlorine (**34**) resulted in similarly potent kinase inhibitory activity ($IC_{50}$ = 3.98 nM) but a substantial decrease in cellular potency ($EC_{50}$ = 151.8 nM), further underscoring the unique advantage conferred by the *ortho*-difluoro substitution. Furthermore, dichloro-substitution (**35**) failed to improve cellular activity and maintained unfavorable cytotoxicity compared with its monochloro analog **25**. **36**−**38** with different combinations of methyl/fluoro substitutions did not outperform **10** in terms of overall potency.

### 3.2. RIPK Selectivity Profiling

While effectively inhibiting necroptosis, some RIPK3 inhibitors concurrently induce RIPK3-mediated apoptosis, which signifi-


https://doi.org/10.1021/acs.jmedchem.5c03775
J. Med. Chem. XXXX, XXX, XXX−XXX

**Table 2. Structures of Compounds 4−10 and Their Inhibitory Activities against RIPK1 Kinase, Antinecroptotic Effects, and Cytotoxicity**

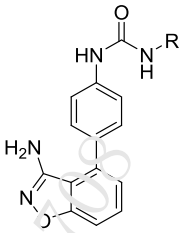

| Number | R | $IC_{50}$ RIPK1 (nM) [a] | $EC_{50}^{HT29}$ (nM) [c] | $IC_{50}^{HT29}$ (nM) [a] |
|---|---|---|---|---|
| **4** | 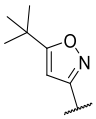 | 2.716 ± 1.13 | > 10000 | 3530 ± 224 |
| **5** |  | > 10000 | > 10000 | > 10000 |
| **6** |  | > 10000 | > 10000 | 118 ± 7.20 |
| **7** |  | > 10000 | > 10000 | > 10000 |
| **8** | 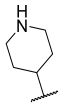 | > 10000 | > 10000 | > 10000 |
| **9** | 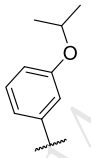 | 106.5 ± 27.3 | > 10000 | 3056 ± 179 |
| **10** | 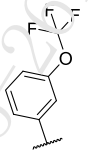 | 72 ± 6.02 | 380.4 ± 30.6 | 7178 ± 694 |
| **1** | 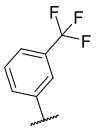 | 66 ± 4.19 | 256.6 ± 21.23 | 3963 ± 565 |
| **GSK-2982772** | / | 16.3 ± 2.60 | 10.96 ± 4.15 | > 10000 |

[a]The $IC_{50}$ values are expressed as the mean ± SD from three independent experiments. [b]The $EC_{50}$ values are expressed as the mean ± SD from three independent experiments.

cantly compromises their safety profile and clinical potential.[33] Since RIPK2 serves as a key molecule in antibacterial innate immunity, off-target RIPK2 inhibition would be detrimental to increase susceptibility to bacterial infections.[38] Given the high structural similarity within the kinase domains of the RIPK family, we specifically evaluated the selectivity of some compounds against RIPK members. As illustrated in Table 5, at a concentration of 500 nM, most tested compounds including **30** exhibited high RIPK1 selectivity over RIPK2 and RIPK3. Collectively, the SAR analysis establishes **30** as a standout


https://doi.org/10.1021/acs.jmedchem.5c03775
J. Med. Chem. XXXX, XXX, XXX−XXX

**Table 3. Structures of Compounds 10−20 and Their Inhibitory Activities against RIPK1 Kinase, Antinecroptotic Effects, and Cytotoxicity**

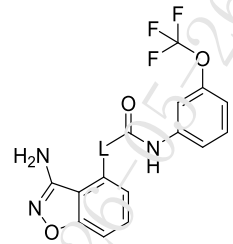

| Number | L | $IC_{50}$ RIPK1 (nM) [a] | $EC_{50}$ HT29 (nM) [b] | $IC_{50}$ HT29 (nM) [a] |
|---|---|---|---|---|
| 11 | 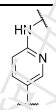 | 8.971 ± 2.68 | 988.7 ± 52.1 | 3651 ± 305 |
| 12 | 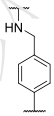 | 2477 ± 267 | > 10000 | > 10000 |
| 13 | 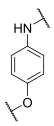 | 2321 ± 376 | > 10000 | 3930 ± 294 |
| 14 |  | > 10000 | > 10000 | > 10000 |
| 15 |  | 77.38 ± 15.3 | > 10000 | 5793 ± 556 |
| 16 | 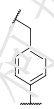 | 24.76 ± 5.13 | > 10000 | 9032 ± 1046 |
| 17 | 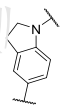 | 111 ± 10.2 | 282.2 ± 17.8 | 3380 ± 258 |
| 18 | 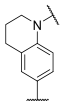 | 178 ± 12.6 | > 10000 | 3592 ± 324 |
| 19 | 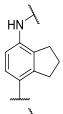 | 82 ± 10.9 | 832.1 ± 127 | 4517 ± 663 |
| 20 | 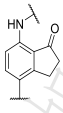 | 142 ± 23.0 | 1041 ± 182 | > 10000 |
| 10 | 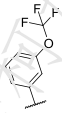 | 72 ± 6.02 | 380.4 ± 30.6 | 7178 ± 694 |
| GSK-2982772 | / | 16.3 ± 2.60 | 10.96 ± 4.15 | > 10000 |

[a]The $IC_{50}$ values are expressed as the mean ± SD from three independent experiments. [b]The $EC_{50}$ values are expressed as the mean ± SD from three independent experiments.

inhibitor, exhibiting superior RIPK1 kinase inhibitory activity ($IC_{50}$ = 4.32 nM), high selectivity over RIPK2 and RIPK3 (over 100-fold), and antinecroptotic efficacy ($EC_{50}$ = 14.43 nM), over 19-fold and 18-fold enhancements relative to lead compound **S24**, respectively, and thus positioning it as an optimal candidate for further evaluation.

### 3.3. Molecular Dynamics Simulations of Compound 30 Complexed with RIPK1 and RIPK3

Given the superior selectivity of compound **30** for RIPK1 over RIPK3, molecular docking and molecular dynamics (MD) simulations were performed to explore its differences in binding RIPK1 and RIPK3. (For detailed information regarding the system setup and MD simulation protocols, refer to the Experimental Section.)

After 500 ns NPT simulation, the backbone RMSD of RIPK1 plateaued around 3 Å, while that of **30** basically fluctuated within 1 Å (Figure 4A and Figure S1). In contrast, the RMSD values observed in the **30**-RIPK3 complex exhibited greater fluctuations (Figure 4B). When comparing the binding modes of **30** in RIPK1 or RIPK3 from molecular docking (Figure 4C,D) and molecular dynamics (Figure 4E,F), an obviously conformational inversion was observed for **30** in RIPK3 after MD, but not for **30** in RIPK1. These analyses suggested that **30** formed more stable interaction with RIPK1. Consistently, hydrogen-bond occupancy during the equilibrium state of MD indicated stronger hydrogen bonding interaction of **30** with RIPK1. As shown in Figure 4G,H, the benzo[*d*]isoxazol-3-amine moiety formed two hydrogen bonds with Met95 and Glu93 of the hinge region (occupancy: 87.48% and 80.34%), respectively; meanwhile, carbonyl group of the urea moiety acted as a hydrogen bond acceptor, interacting with Asp156 at an occupancy of 96.95%. Undoubtedly, such stable hydrogen bonding networks helped fix the trifluoromethoxybenzene group in the hydrophobic back pocket. However, key hydrogen bonding interaction with the hinge region was lacked for **30** complexed with RIPK3, and only labile hydrogen bonds were made with Met97 and Asp160. Further MM/GBSA (Molecular Mechanics/Generalized Born Surface Area) binding free energy analysis of the **30**-RIPK1 complex revealed strong binding affinity (ΔG −49.73 kcal/mol), omitting the entropy effect. Energy decomposition on per residue of RIPK1 identified that Met67 and Glu93 as the top-two contributions (Figure 4I). More precisely, Met67 mainly participated in van der Waals interactions, highlighting the importance of the middle benzene ring of **30**; while, Glu93 exerted primarily electrostatic interactions, confirming the necessary of hydrogen-bonding capacity of **30** with the hinge region (Figure 4J). These results are in accord with the RIPK1 selectivity of **30** over RIPK3 and provides useful insights into the binding mode of **30** bound to RIPK1.

### 3.4. Kinase Panel Selectivity of Compound 30

The kinase selectivity profile of compound **30** was evaluated against a panel of 80 kinases at a concentration of 100 nM (Figure 5 and Table S2). Using a threshold of <90% residual activity to define selectivity (corresponding to >25-fold selectivity over RIPK1), compound **30** exhibited excellent overall selectivity. It inhibited only 6 kinases by >90%: EPHB4,


https://doi.org/10.1021/acs.jmedchem.5c03775
J. Med. Chem. XXXX, XXX, XXX−XXX

Table 4. Structures of 21−38 and Their Inhibitory Activities against RIPK1 Kinase, Antinecroptotic Effects, and Cytotoxicity

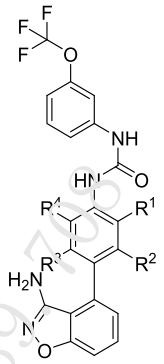

| number | $R^1$ | $R^2$ | $R^3$ | $R^4$ | $IC_{50}$RIPK1 (nM)[a] | $EC_{50}^{HT29}$(nM)[b] | $IC_{50}^{HT29}$(nM)[a] |
|---|---|---|---|---|---|---|---|
| **21** | $CH_3$ | H | H | H | 7.511 ± 2.51 | 426.9 ± 47.1 | 5408 ± 411 |
| **22** | H | $CH_3$ | H | H | 15.15 ± 2.47 | 295.0 ± 40.1 | 9653 ± 309 |
| **23** | F | H | H | H | 72 ± 12.17 | 49 ± 8.32 | 8124 ± 225 |
| **24** | H | F | H | H | 11.15 ± 1.02 | 262.6 ± 28.1 | 4002 ± 322 |
| **25** | Cl | H | H | H | 16.1 ± 2.97 | 323.9 ± 63.2 | 3771 ± 231 |
| **26** | H | Cl | H | H | 13.81 ± 3.02 | 160.6 ± 21.1 | 1908 ± 165 |
| **27** | $OCH_3$ | H | H | H | 145.3 ± 25.2 | >10000 | 4737 ± 237 |
| **28** | H | CN | H | H | 52.53 ± 17.4 | 153.0 ± 19.8 | 2049 ± 103 |
| **29** | $CH_3$ | $CH_3$ | H | H | 17.38 ± 2.95 | 2781 ± 123 | 7129 ± 352 |
| **30** | F | F | H | H | 4.32 ± 0.46 | 14.43 ± 1.69 | 1760 ± 97 |
| **31** | F | H | H | F | 12.43 ± 2.03 | 854.1 ± 101 | 9518 ± 122 |
| **32** | H | F | F | H | 15.3 ± 3.58 | 352.9 ± 74.2 | >10000 |
| **33** | F | H | F | H | 12.73 ± 1.64 | 731.1 ± 53.4 | 8463 ± 416 |
| **34** | F | Cl | H | H | 3.89 ± 0.40 | 151.8 ± 19.8 | 1824 ± 99.1 |
| **35** | Cl | Cl | H | H | 10.34 ± 2.62 | 393.2 ± 24.0 | 4075 ± 459 |
| **36** | $CH_3$ | F | H | H | 6.706 ± 1.98 | 300.4 ± 29.1 | 6932 ± 331 |
| **37** | H | F | H | $CH_3$ | 21.99 ± 5.26 | 1106 ± 95.2 | >10000 |
| **38** | H | $CH_3$ | H | F | 460.1 ± 64.2 | >10000 | 3812 ± 328 |
| **10** | H | H | H | H | 72 ± 6.02 | 380.4 ± 30.6 | 7178 ± 694 |
| **GSK-2982772** | | | | | 16.3 ± 2.60 | 10.96 ± 4.15 | >10000 |

[a]The $IC_{50}$ values are expressed as the mean ± SD from three independent experiments. [b]The $EC_{50}$ values are expressed as the mean ± SD from three independent experiments.

Table 5. RIPK1 Kinase Selectivity Profiling of Compounds 21, 22, 24−26, 28, 30, 32, and 35

| | | kinase activity % @ 0.5 μM[b] | |
|---|---|---|---|
| number | $IC_{50}$RIPK1 (nM)[a] | RIPK2 | RIPK3 |
| **21** | 7.511 ± 2.51 | 98.39 ± 12.7 | 108.40 ± 28.3 |
| **22** | 15.15 ± 2.47 | 103.98 ± 16.4 | 103.83 ± 4.81 |
| **24** | 11.15 ± 1.02 | 107.09 ± 12.9 | 99.45 ± 13.2 |
| **25** | 16.1 ± 2.97 | 101.71 ± 19.5 | 104.22 ± 18.4 |
| **26** | 13.81 ± 3.02 | 98.33 ± 7.90 | 102.68 ± 26.3 |
| **28** | 52.53 ± 17.4 | 105.72 ± 17.5 | 108.81 ± 25.1 |
| **30** | 4.32 ± 0.46 | 95.74 ± 11.3 | 84.33 ± 22.6 |
| **32** | 15.3 ± 3.58 | 105 ± 15.3 | 103.45 ± 14.4 |
| **35** | 10.34 ± 2.62 | 83.41 ± 8.55 | 55.69 ± 13.7 |

[a]The $IC_{50}$ values are expressed as the mean ± SD from three independent experiments. [b]The kinase activity % values are expressed as the mean ± SD from three independent experiments.

TRKB, p70S6K, MAP3K19, EPHA2 and FGFR1. A brief assessment of potential off-target toxicity associated with these kinases was conducted. Among them, MAP3K19 is a known driver of pulmonary fibrosis, and its inhibition may synergize with RIPK1 blockade to enhance antifibrotic efficacy.[39] Conversely, EPHB4, EPHA2 and FGFR1 are receptor tyrosine kinases involved in angiogenesis and tissue repair;[40,41] their partial inhibition at 100 nM is unlikely to cause significant toxicity. TRKB and p70S6K are implicated in cell survival and metabolism;[42,43] however, their transient inhibition at this low concentration is not expected to produce adverse systemic effects. For the vast majority of the kinase panel, inhibition remained below 50%, confirming minimal off-target activity and high specificity of **30** for RIPK1. Overall, the off-target profile of **30** at 100 nM suggests a low risk of kinase-mediated toxicity, supporting its suitability for *in vivo* evaluation.

### 3.5. Preliminary Pharmacokinetic Evaluation and Metabolic Stability of Compound 30

Subsequently, the *in vivo* pharmacokinetic properties of compound **30** were evaluated in Table 6 following intravenous injection (*i.v.*, 1 mg/kg) and oral administration via gavage (*p.o.*, 10 mg/kg; formulated as 2 mg/mL API in 5% DMSO, 5% Tween 80, and 90% saline). In the *i.v.* group, **30** exhibited rapid distribution and moderate clearance, as indicated by the following parameters: $T_{max}$ = 0.083 h, mean elimination half-life ($t_{1/2}$) = 3.06 h and clearance (CL) = 8.59 mL/min/kg. For oral administration (n = 5), **30** achieved an acceptable oral bioavailability ($F$ = 39.3%) and a similar metabolic stability ($t_{1/2}$ = 3.63 h). The favorable bioavailability combined with the moderate half-life supports sustained *in vivo* pharmacological evaluation. Additionally, the metabolic stability of **30** was


https://doi.org/10.1021/acs.jmedchem.5c03775
J. Med. Chem. XXXX, XXX, XXX−XXX

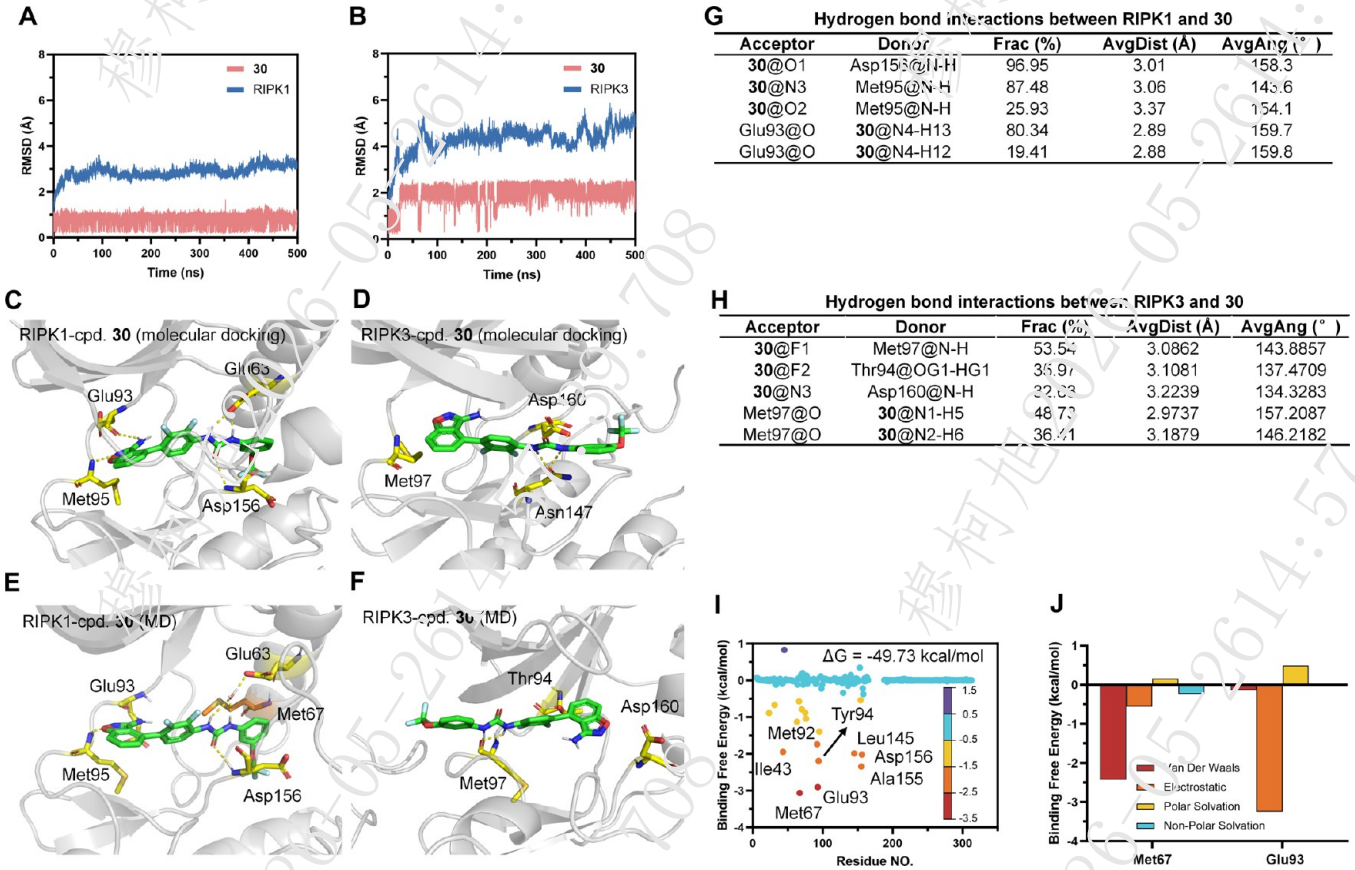


**Figure 4.** Results from molecular dynamics simulation. (A-B) RMSD of the backbone for RIPK1/3 (blue) and **30** listing to protein (red); (C, D) binding pose of **30** (green sticks) with RIPK1 (yellow sticks; PDB: 4NEU) and RIPK3 (yellow sticks; PDB: 7MX3) after molecular docking; (E, F) binding pose of **30** (green sticks) and RIPK1/3 (yellow sticks) at the end of MD simulation; (G, H) hydrogen bond interactions between **30** and RIPK1/3 (only occupancy over 10% were shown); (I) MM/GBSA binding free energy per residue for RIPK1 in complex with **30**; (J) energy contributions of key residues to the binding free energy.

assessed in human and rat hepatic microsomes. As shown in Table 7, **30** exhibited higher stability in rat microsomes ($t_{1/2}$ = 74.52 min) than in human microsomes ($t_{1/2}$ = 33.16 min). Subsequently, we further analyzed the metabolites of **30** in rats using the LC-MS/MS method. The results indicated that hydroxylation, oxidation, hydrolysis and glucuronidation were its primary metabolic pathways (Table S3 and Figure S2).

### 3.6. Safety Evaluation of Compound 30 *In Vivo*

We next assessed the acute toxicity of compound **30** in ICR mice (*p.o.*, single dose of 400 mg/kg). Survival, behavioral changes, and body weight of the rodents were monitored throughout the 14 days after dosing. Then, major organs (heart, liver, spleen, lungs and kidneys) were collected for histopathological examination via hematoxylin and eosin (H&E) staining. As a result, no mouse died or behaved abnormally, accompanied by unaffected body weight (Figure 6A,B). HE staining revealed no notable adverse effect on the normal cellular morphology of the organs examined. In conclusion, **30** exhibits a favorable safety profile under the tested conditions.

### 3.7. Intraperitoneal Injection of Compound 30 Reduces Hepatic Fibrosis of Mice Infected with *S. japonicum*

With the favorable safety profile of compound **30** established, we proceeded to evaluate its antifibrotic efficacy in a murine model of schistosomiasis-induced hepatic fibrosis. Prior to *in vivo* testing, we confirmed its activity against murine RIPK1 *in vitro*. In murine L929 cells stimulated with TSZ to induce necroptosis, compound **30** exhibited potent protective effects with an $EC_{50}$ of 5.33 nM (Figure 7A). Western blot analysis further demonstrated that compound **30** dose-dependently reduced p-RIPK1 (Figure 7B), confirming its effective targeting of murine RIPK1 and suppression of necroptotic signaling. These results provided a mechanistic basis for subsequent *in vivo* evaluation.

We then assessed the therapeutic effects of compound **30** in Schistosoma-infected mice. After 4 weeks of intraperitoneal administration (*i.p.*, qd), changes in body weight and liver pathology were assessed (Figure 7C). Healthy control mice exhibited a steady weight gain over time. In contrast, infected mice showed marked weight loss by week 5 postinfection, reaching a nadir at week 6, before partial recovery. Compared with the infected control, **30**-treated groups (I5:5 mg/kg; I10:10 mg/kg) showed significant weight recovery at weeks 8 and 9 postinfection ($P < 0.05$; Figure 7D). Mean egg burdens did not differ significantly among the infected control (55,203.79 ± 13,558.93), I5 (55,296.84 ± 15,919.02), and I10 (70,846.53 ± 23,117.90) groups ($P > 0.05$; Figure 7E). Organ indices were significantly elevated in infected mice. The liver and spleen indices were 4.13 ± 0.27% and 0.22 ± 0.04% in healthy controls, versus 8.67 ± 0.65% and 1.60 ± 0.36% in the infected control. Treatment with I10 significantly reduced both indices (liver: 6.14 ± 0.67%; spleen: 0.76 ± 0.21%; $P < 0.05$; Figure 7F,G). Hepatic enzyme levels (ALT and AST) were significantly elevated in infected controls (68.84 ± 7.82 U/L and 61.07 ± 8.62 U/L) compared to healthy mice (23.51 ± 8.18 U/L and


https://doi.org/10.1021/acs.jmedchem.5c03775
J. Med. Chem. XXXX, XXX, XXX−XXX

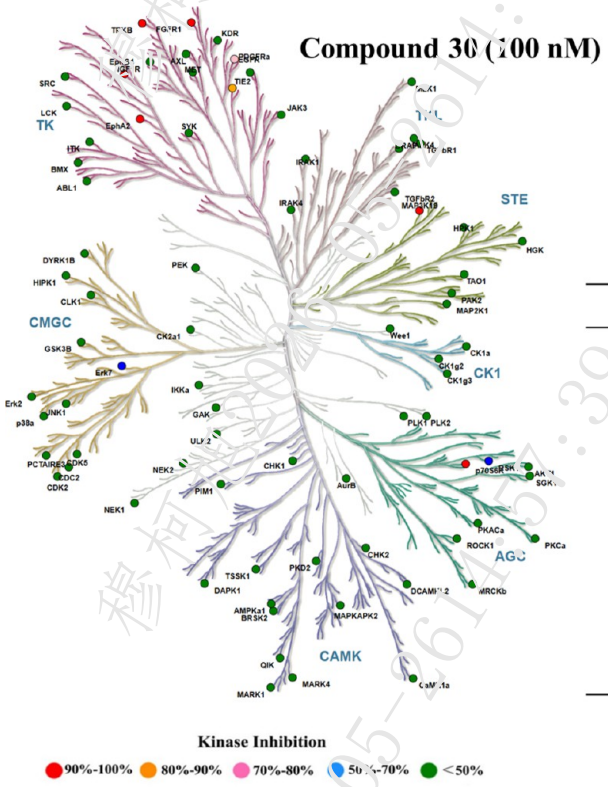


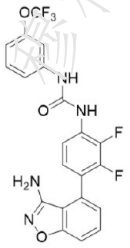

| Kinase | Kinase inhibition% @ 100 nM |
|---|---|
| EPHB4 | 103.13 |
| TRKB | 99.58 |
| p70S6K | 96.53 |
| MAP3K19 | 92.50 |
| EPHA2 | 91.89 |
| FGFR1 | 90.77 |
| TIE2 | 85.61 |
| PDGFRα | 76.27 |
| RSK1 | 60.24 |
| Erk7 | 58.51 |

**Figure 5.** Compound **30** underwent comprehensive wild-type kinase profiling to assess selectivity against a panel of 80 kinases.

**Table 6. Pharmacokinetic Parameters of Compound 30 in Rats**

| parameter | IV group (1 mg/kg) | PO group (10 mg/kg) |
|---|---|---|
| $C_{max}$(ng/mL) | 3237.5 ± 1232.7 | 1920.0 ± 584.6 |
| $T_{max}$ (h) | 0.083 ± 0.000 | 1.25 ± 0.34 |
| $AUC_{last}$(h·ng/mL) | 2070.5 ± 586.8 | 8128.4 ± 1341.7 |
| $t_{1/2}$ (h) | 3.06 ± 0.19 | 3.63 ± 0.79 |
| Vz (L/kg) | 2.25 ± 0.61 | 6.54 ± 1.50 |
| CL (mL/min/kg) | 8.59 ± 2.71 | 21.32 ± 5.03 |
| $MRT_{last}$ (h) | 1.80 ± 0.70 | 2.90 ± 0.39 |
| *F* (%) | | 39.3 |

**Table 7. Liver Microsomal Stability of Compound 30**

| parameter | human microsomes | rat microsomes |
|---|---|---|
| $t_{1/2}$ (min) | 33.16 | 74.52 |
| $CL_{int}$(mL/min/mg) | 0.0523 | 0.023 |

21.43 ± 5.30 U/L). Treatment of **30**, especially I10 group, restored these levels to near-normal values (ALT: 23.90 ± 9.00 U/L; AST: 23.68 ± 9.01 U/L; $P < 0.05$), indicating ameliorated liver injury (Figure 7H,I). Granuloma areas were significantly smaller in I5 (33,245.53 ± 21,752.78 $\mu m^2$) and I10 (18,983.35 ± 11,853.70 $\mu m^2$) groups compared to the infected control (51,121.68 ± 26,191.02 $\mu m^2$; $P < 0.05$; Figure 7J). Masson staining revealed a significant reduction in collagen deposition in treated groups (I5:17.33 ± 3.80%; I10:14.74 ± 4.36%) relative to the infected control (34.26 ± 4.10%; $P < 0.05$; Figure 7J). The upregulation of collagen I and α-SMA in infected livers was significantly suppressed by **30** ($P < 0.05$; Figure 7K). Hepatic hydroxyproline content, indicative of collagen accumulation, was markedly reduced in I5 (0.39 ± 0.08 mg/g) and I10 (0.25 ± 0.06 mg/g) groups versus the infected control (0.58 ± 0.15 mg/g; $P < 0.05$; Figure 7L). Liver ROS levels were also significantly lower in I5 (119,033.90 ± 31,601.15 RFU) and I10 (56,532.92 ± 20,493.61 RFU) groups compared to infected controls (282,942.30 ± 47,465.79 RFU; $P < 0.05$; Figure 7M). Together, these results indicate that intraperitoneal administration of **30** effectively alleviates egg-induced granulomatous inflammation and hepatic fibrosis in murine schistosomiasis.

### 3.8. Oral Administration of Compound 30 Alleviates Hepatic Fibrosis of Mice Infected with *S. japonicum*

To optimize the route of administration for clinical translation, we evaluated the efficacy of an orally administered compound **30** (*i.g.*, qd). First, schistosome-infected mice were treated with low doses of the compound at 10 (I10), 20 (I20), and 30 (I30) mg/kg, while PZQ 250 mg/kg was used as a positive control (Figure S3A). However, the results showed that under the same egg burden (Figure S3B), the low-dose compound did not exhibit significant protective effects against liver damage and fibrosis. Compared to the infected group, there were no statistical differences in liver index, spleen index, and serum ALT levels (Figure S3C–E). AST levels, egg granuloma, and fibrosis in the liver only decreased at 30 mg/kg, with statistically significant differences ($P < 0.05$, Figure S3F–H). The positive control PZQ demonstrated good antifibrotic effects, with a 15.98% decrease in the area of fibrosis in the liver compared to the control group (Figure S3H). Subsequently, we increased the oral administration dose to 50 mg/kg and 100 mg/kg (Figure 8A). Body weight increased progressively in healthy controls, whereas schistosome-infected mice exhibited a sharp decline, reaching the lowest point at week 6 before partial recovery. Notably, oral administration of **30** at 50 (I50) and 100 (I100) mg/kg significantly improved body weight recovery at weeks 8 and 9 postinfection compared to the infected control (Ctr) ($P < 0.05$; Figure 8B). Although egg burdens were numerically lower in the


https://doi.org/10.1021/acs.jmedchem.5c03775
J. Med. Chem. XXXX, XXX, XXX−XXX

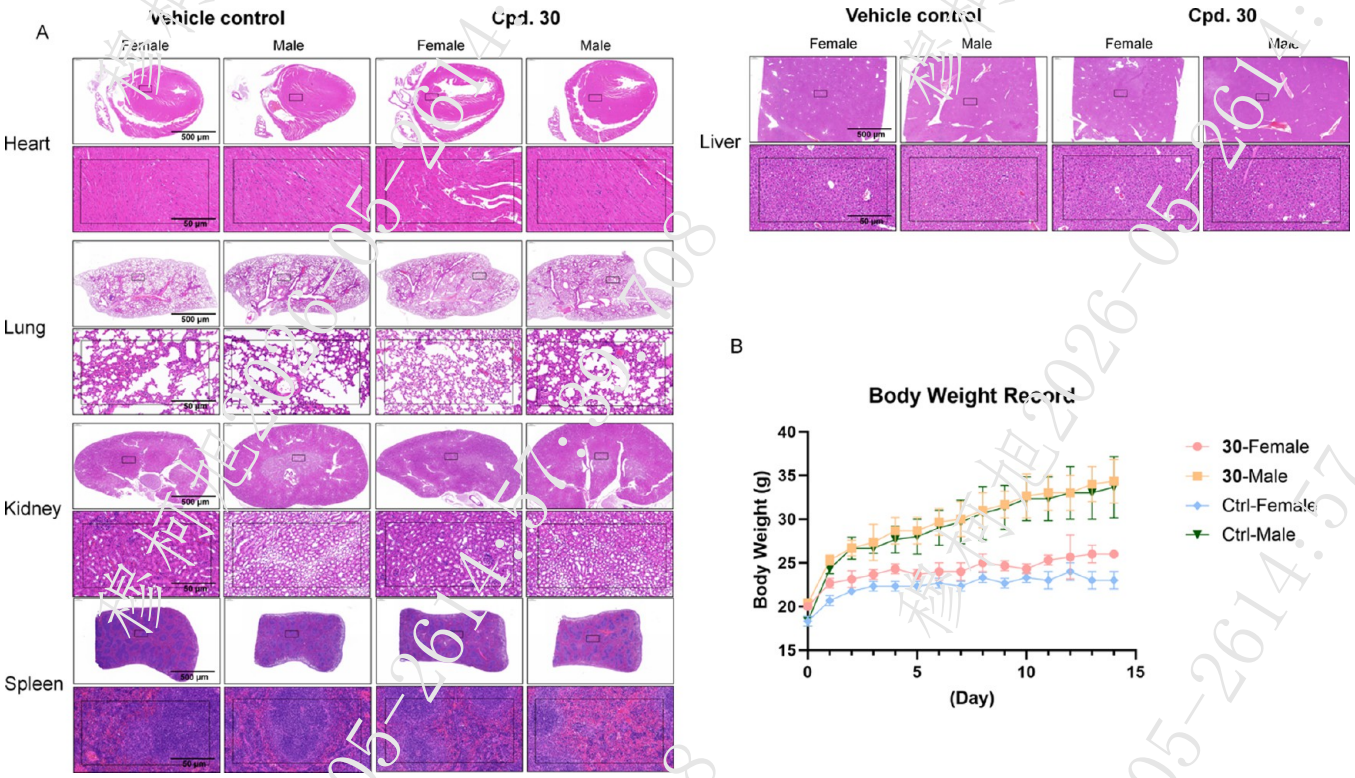


**Figure 6.** Safety evaluation of compound **30***in vivo* (single dose, *p.o.*, 400 mg/kg). (A) Histopathological analysis of vital organs following administered with **30**. Representative H&E-stained sections of heart, lung, kidney, spleen, and liner from mice treated with vehicle control or **30**. (B) Body weight over time in the same administration groups.

treated groups (I50:49,991.44 ± 11,327.66; I100:53,577.39 ± 15,723.35) than in the Ctr group (75,846.22 ± 25,873.59), the differences were not statistically significant ($P > 0.05$; Figure 8C). After sacrifice, liver and spleen indices were calculated. Oral treatment of **30** significantly ameliorated infection-induced hepatosplenomegaly compared to the infected control, with the I100 group showing a marked reduction in both liver and spleen indices (6.84 ± 0.44% and 0.94 ± 0.11%, respectively; $P < 0.05$; Figure 8D,E). Consistent with this improvement, serum ALT and AST levels, indicators of hepatic injury, were also significantly reduced in the treated groups ($P < 0.05$; Figure 8F,G). Oral treatment of **30** significantly attenuated schistosome-induced liver fibrosis, as demonstrated by histopathological and molecular markers. HE staining revealed that granuloma area was significantly reduced in the I50 (20,686.57 ± 11,117.23 $\mu m^2$) and I100 (15,408.16 ± 5,641.63 $\mu m^2$) groups compared to the infected control (38,473.51 ± 33,569.96 $\mu m^2$; $P < 0.05$). Correspondingly, Masson's trichrome staining showed a significant decrease in the collagen area ratio (Ctr: 36.54 ± 1.43%; I50:29.44 ± 1.46%; I100:24.82 ± 0.94%; $P < 0.05$; Figure 8H). Moreover, the infection-induced upregulation of key fibrotic markers, collagen I and $\alpha$-SMA, was significantly reversed by the treatment ($P < 0.05$; Figure 8I). Furthermore, oral **30** treatment significantly reduced hepatic hydroxyproline content, a key biochemical marker of fibrosis, and attenuated oxidative stress by lowering ROS levels in a dose-dependent manner ($P < 0.05$; Figure 8J,K). Specifically, hydroxyproline content and ROS levels in the I100 group were reduced to 0.27 ± 0.08 mg/g and 53,688.13 ± 21,309.58 RFU, respectively, approaching those of the healthy controls (0.16 ± 0.03 mg/g; 35,530.79 ± 7,861.90 RFU) and markedly lower than the infected control (0.43 ± 0.14 mg/g; 275,680.90 ± 83,405.07 RFU). Collectively, these data demonstrate that oral administration of **30** effectively alleviates egg granuloma inflammation and hepatic fibrosis in schistosomiasis.

### 3.9. Compound 30 Suppresses the AKT/PI3K/NF-κB and IL-17 Signaling Pathways in the Livers of Mice Infected with *S. japonicum*

To elucidate the signaling pathways by which compound **30** ameliorates hepatic fibrotic lesions, transcriptome sequencing was performed on liver tissues from mice orally administered **30** at 100 mg/kg. Compared with healthy mice, livers of schistosome-infected mice showed upregulated expression of inflammatory factors, including TNF-$\alpha$, IL-17, and IL-1b, and chemokines such as CXCL5/9/10/16 and CCL2/4/5/7/11/22 (Figure 9A). These increases were attenuated following treatment of **30**. KEGG enrichment analysis of differentially expressed genes revealed that infected mice exhibited significant enrichment in pathways related to cytokine−cytokine receptor interaction, NF-κB, IL-17, PI3K−AKT, and TNF signaling compared to healthy controls (Figure 9B). In **30**-treated mice, these pathways, particularly cytokine−cytokine receptor interaction, PI3K−AKT/NF-κB, and IL-17 signaling, were markedly downregulated relative to the infected group (Figure 9C). Transcriptome findings were validated using a PCR array to assess mRNA expression of inflammatory factors and chemokines. Oral treatment of **30** significantly reduced mRNA levels of CX3CL1, IL1r1, CCL19, IL1r2, and IL1b (Figure 10A,B). Subsequent KEGG analysis further confirmed enrichment in IL-17 signaling, cytokine−cytokine receptor interaction, and NF-κB signaling among the differentially expressed genes (Figure 10C). Western blot analysis was employed to assess the PI3K−AKT/NF-κB pathway. Schistosome infection elevated levels of necroptosis-related proteins (RIPK1, RIPK3, MLKL, and their


https://doi.org/10.1021/acs.jmedchem.5c03775
J. Med. Chem. XXXX, XXX, XXX−XXX

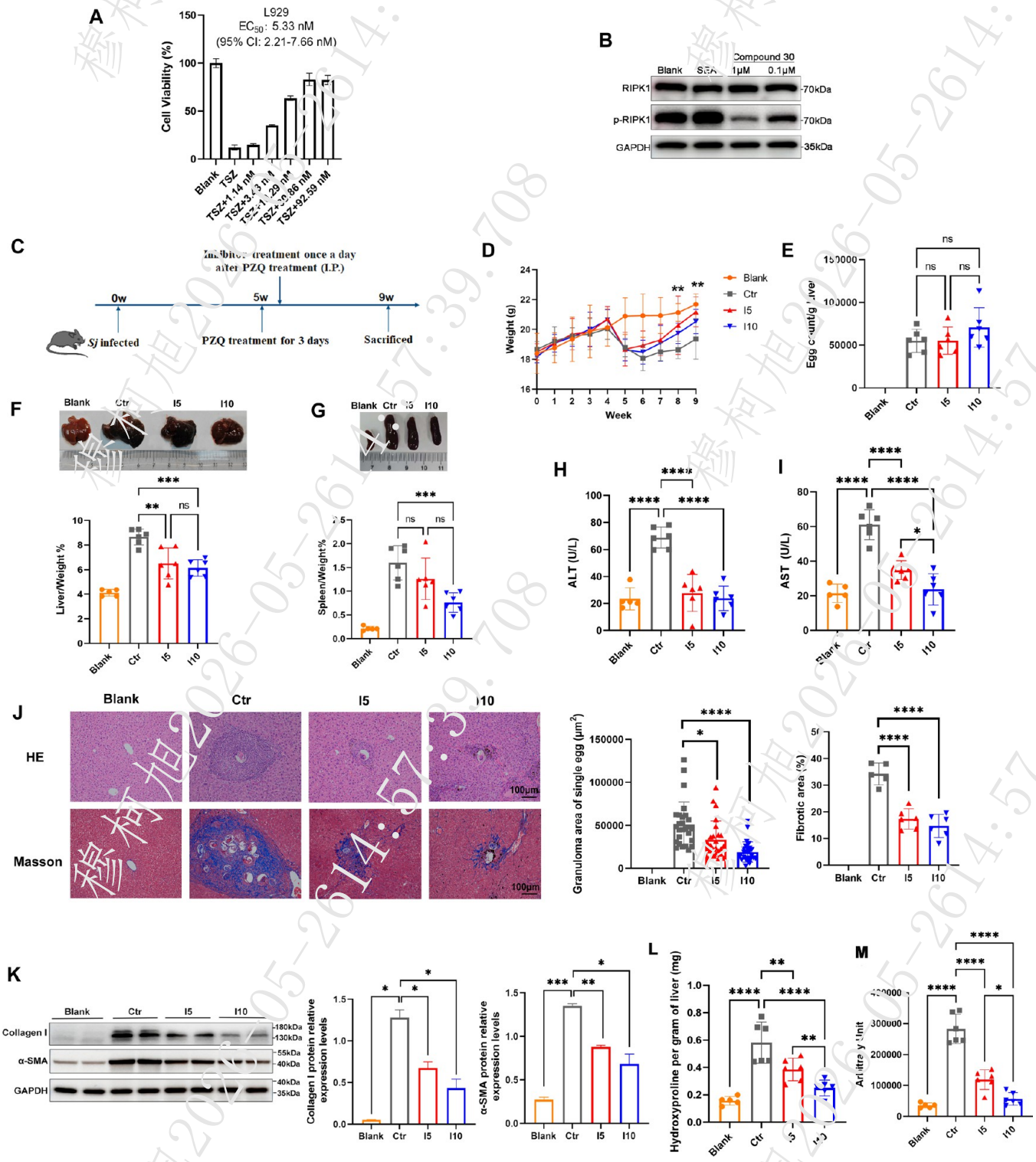


**Figure 7.** Intraperitoneal injection of compound **30** alleviates hepatic fibrosis of mice infected with *S. japonicum*. (A) $EC_{50}$ determination of **30** in L929 cells. (B) Effect of **30** on RIPK1 phosphorylation. Protein levels of total RIPK1 and p-RIPK1 in L929 cells treated with **30** were detected by Western Blot. GAPDH was used as a loading control. (C) Schematic of the experimental protocol for treating hepatic fibrosis in schistosome-infected mice via intraperitoneal injection of **30**. C57BL/6 mice were infected with *S. japonicum* cercariae. At 5 weeks postinfection, infected mice were treated with praziquantel (250 mg/kg) by oral gavage. Subsequently, the infected mice received continuous treatment with **30** at doses of I5 (5 mg/kg) and I10 (10 mg/kg) for 4 weeks before dissection. Schistosome-infected mice injected intraperitoneally with PBS (Ctr) and healthy mice (Blank) served as controls; (D) body weight changes in schistosome-infected mice treated intraperitoneally with **30**. Body weight was measured weekly; (E) egg burden in the livers of schistosome-infected mice treated intraperitoneally with **30**; (F) liver morphology and liver index (liver weight/body weight ratio) of schistosome-infected mice treated intraperitoneally with **30**; (G) spleen morphology and spleen index (spleen weight/body weight ratio) of schistosome-infected mice treated intraperitoneally with **30**; (H) serum alanine aminotransferase (ALT) levels in schistosome-infected mice treated intraperitoneally with **30**; (I) serum aspartate aminotransferase (AST) levels in schistosome-infected mice treated intraperitoneally with **30**; (J) hepatic egg granulomas and fibrotic lesions in schistosome-infected mice treated intraperitoneally with **30**. HE staining shows inflammatory responses


https://doi.org/10.1021/acs.jmedchem.5c03775
J. Med. Chem. XXXX, XXX, XXX−XXX

**Figure** 7. continued

around egg granulomas, with statistical analysis of the area of a single egg granuloma. Masson staining shows hepatic fibrotic lesions (blue staining), with statistical analysis of the collagen area percentage; (K) Western blot analysis and grayscale quantification of Collagen I and $\alpha$-SMA protein levels in the livers of schistosome-infected mice treated intraperitoneally with **30**; (L) hepatic hydroxyproline content in schistosome-infected mice treated intraperitoneally with **30**; (M) hepatic reactive oxygen species (ROS) levels in schistosome-infected mice treated intraperitoneally with the **30**.

phosphorylated forms) and the apoptosis-related protein cleaved-caspase 3. Treatment of **30** reduced these markers in a dose-dependent manner (Figure 10D). Similarly, signaling molecules (PI3K, AKT, P65, and their phosphorylated forms) and inflammatory markers (F4/80, TNF-$\alpha$) were also downregulated in a concentration-dependent fashion (Figure 10E). These results indicate that **30** curbs hepatic inflammation by suppressing necroptosis-related factors and subsequently inhibiting the PI3K−AKT/NF-$\kappa$B signaling pathway. In addition, analysis of splenocyte culture supernatants revealed that **30** treatment reduced levels of TNF-$\alpha$, IL-4, and IL-17 in mouse livers (Figure 10F), further corroborating the transcriptomic data and supporting the conclusion that **30** alleviates hepatic inflammation via downregulation of TNF-$\alpha$, IL-4, and IL-17.

## 4. DISCUSSION AND CONCLUSIONS

Guided by structure-based drug design strategy, we identified the compound **30** with potent RIPK1 kinase inhibitory activity ($IC_{50}$ = 4.32 nM) and cellular antinecroptotic efficacy ($EC_{50}$ = 14.43 nM), respectively, as well as RIPK1 selectivity over RIPK3 and other kinases. During the process of structural optimization, a leap of the cellular activity occurred when incorporating two fluorine atoms at the ortho positions of central benzene ring. This "difluoro" effect is likely mediated by the elevation in cell membrane penetration, as supported by our in silico ADME predictions which showed improved permeability metrics for **30** over its unsubstituted **10**. MD simulations corroborated that **30** adopts a stable, classic Type II kinase-inhibitor binding mode within RIPK1, and coincided with its selectivity. Compound **30** possessed good PK and safety profile in rodents, supporting further pharmacology studies.

*In vivo* experiments demonstrated that this RIPK1-targeting small molecule compound exerted potent antifibrotic effects in a dose-dependent manner. In a murine model of schistosome-induced hepatic fibrosis, administration of **30** via either intraperitoneal injection or oral gavage led to significant improvements across multiple therapeutic indices, including recovery of body weight, reduction in liver and spleen indices (indicative of improved health status), decreases in serum ALT and AST levels and single egg granuloma area (reflecting attenuated liver injury), and downregulation of hydroxyproline content, collagen area proportion, and expression of extracellular matrix proteins (Collagen I, $\alpha$-SMA) (demonstrating alleviation of hepatic fibrosis). Hepatic oxidative stress was also concurrently reduced. Mechanistic investigations via transcriptome sequencing and Western blot analysis revealed that **30** effectively suppresses RIPK1 and RIPK3, subsequently downregulating the phosphorylation levels of the PI3K-AKT and NF-$\kappa$B signaling pathways and reducing the expression of key inflammatory factors such as IL-17 and TNF-$\alpha$.The PI3K/AKT and NF-$\kappa$B pathways jointly play a crucial role in regulating cell survival, proliferation, inflammatory response, and immune response.[44] Literature reports indicate that RIPK1 can regulate the PI3K-AKT signaling pathway. The use of RIPK1 inhibitor Nec-1S can inhibit the phosphorylation level of pPI3K-pAKT, thereby suppressing the expression of inflammatory factors through Eukaryotic Initiation Factor 4E (eIF4E). Additionally, a decrease in pNF-$\kappa$B levels has been observed. The RIPK1 agonist (Citronellol) enhanced the expression of p-eIF4E and p-PI3K.[45] In Parkinson's disease (PD) mice, RIPK1-specific inhibitors Nec-1 and Nec-1s exerted anti-inflammatory effects by modulating the PI3K/Akt and NF-$\kappa$B signaling pathways.[46] Our research results are consistent with previous findings. Our study suggests that its antifibrotic action is likely mediated through the inhibition of necroptosis, apoptosis, and associated inflammatory signaling.

From a translational perspective, based on its pharmacokinetic profile, intraperitoneal injection achieved more pronounced histological improvements at lower administered doses compared to oral administration, which nonetheless conferred significant efficacy particularly at higher doses. From a drug development standpoint, the oral route offers greater convenience and clinical translatability. Moreover, RIPK1-mediated necroptosis and inflammation represent a common pathogenic axis in various chronic liver injuries. While our study focused on schistosomiasis-induced fibrosis—a model of inflammation-driven pathology—the central role of RIPK1 suggests that its inhibition holds promise for treating hepatic fibrosis across diverse etiologies, a premise that merits further investigation.

We also acknowledge certain limitations of the present work. The SAR could be explored more comprehensively. Direct *in vivo* evidence causally linking RIPK1 target engagement to antifibrotic efficacy, such as through detailed PK/PD studies, would further strengthen our conclusions. Additionally, a more extensive preclinical druggability profile is required for clinical translation. Accordingly, future studies to address these points and to further evaluate the therapeutic potential of **30** in other fibrotic contexts are warranted.

In conclusion, this study identifies a highly potent and selective RIPK1 inhibitor and provides compelling scientific evidence for its robust *in vivo* hepatic fibrosis treatment efficacy, enlightening the clinical advancement of RIPK1 inhibitors in combating organ fibrosis.

## EXPERIMENTAL SECTION

### General Procedures

Unless otherwise specified, all the chemical solvents and reagents were analytically pure, which were obtained from commercial suppliers and used without further purification. All reactions were monitored by TLC (Merck Kieselgel GF254), and spots were visualized with UV light or iodine. Melting points were tested by the X-4 digital display micromelting point apparatus (Beijing Tech Instrument Company, Ltd., Beijing, China). $^1$H and $^{13}$C NMR spectra were obtained on a Bruker AVANCE AV-400 spectrometer (400 MHz for $^1$H NMR and 100 MHz for $^{13}$C NMR), or a Bruker AVANCE AV-300 spectrometer (300 MHz for $^1$H NMR and 75 MHz for $^{13}$C NMR) or Bruker AVANCE AV-300 spectrometer (600 MHz for $^1$H NMR and 151 MHz for $^{13}$C NMR). Mass spectra were recorded on the Agilent 1100 LC-MSD mass spectrometer (Agilent, USA) or Q-Tof micro MS (micromass company). The purity of all biologically evaluated


https://doi.org/10.1021/acs.jmedchem.5c03775
J. Med. Chem. XXXX, XXX, XXX−XXX

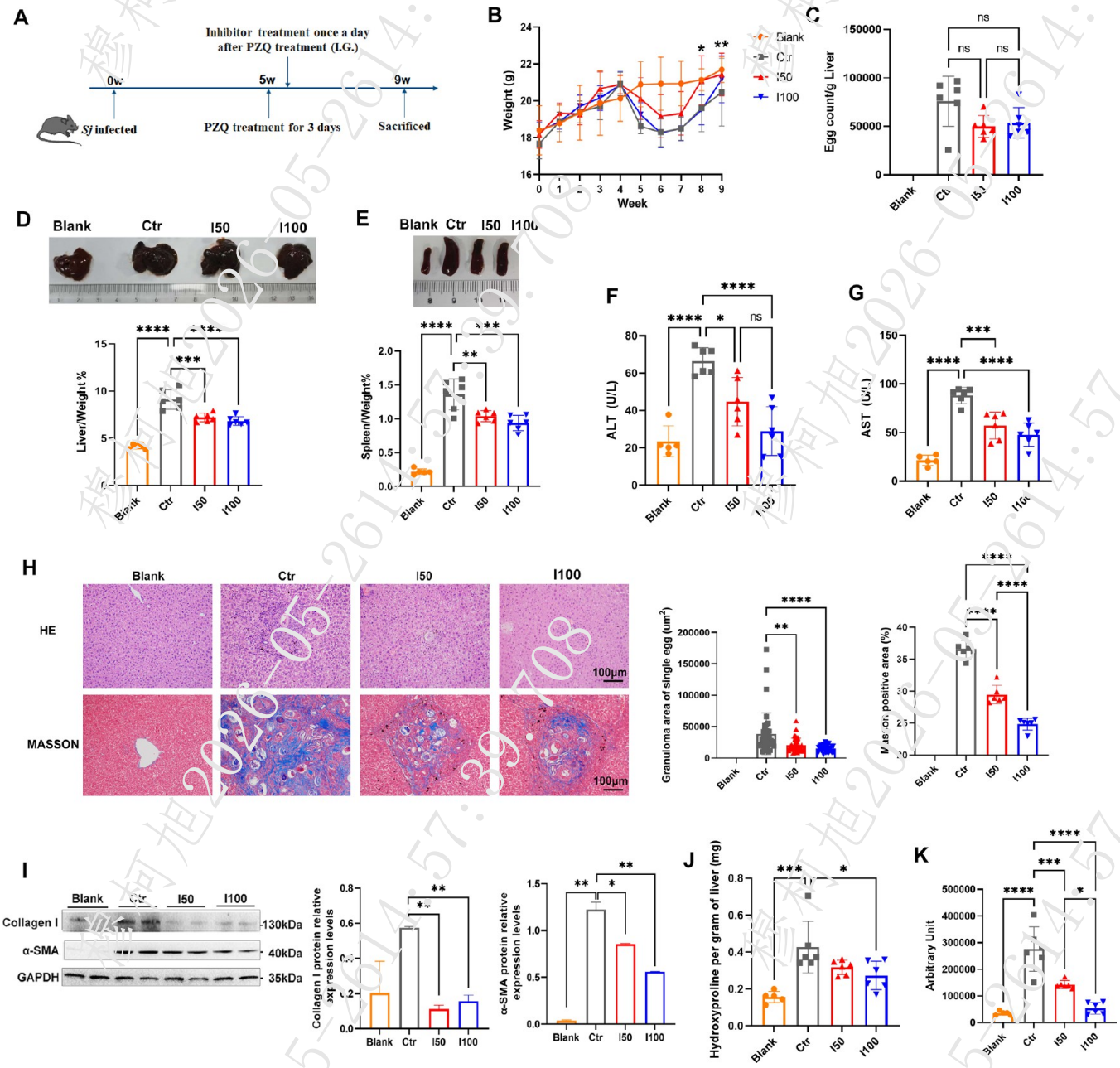


**Figure 8.** Oral administration of compound **30** alleviates hepatic fibrosis in mice infected with *S. japonicum*. (A) Schematic of the experimental protocol for treating hepatic fibrosis in schistosome-infected mice via oral gavage of **30**. C57BL/6 mice were infected with *S. japonicum* cercariae. At 5 weeks postinfection, infected mice were treated with praziquantel (250 mg/kg) by oral gavage. Subsequently, the infected mice received continuous treatment with **30** at doses of I50 (50 mg/kg) and I100 (100 mg/kg) for 4 weeks before dissection. Schistosome-infected mice injected intraperitoneally with PBS (Ctr) and healthy mice (Blank) served as controls. (B) Body weight changes in schistosome-infected mice treated orally with **30**. Body weight was measured weekly. (C) Egg burden in the livers of schistosome-infected mice treated orally with **30**. (D) Liver morphology and liver index (liver weight/body weight ratio) of schistosome-infected mice treated orally with **30**. (E) Spleen morphology and spleen index (spleen weight/body weight ratio) of schistosome-infected mice treated orally with **30**. (F) Serum alanine aminotransferase (ALT) levels in schistosome-infected mice treated orally with **30**. (G) Serum aspartate aminotransferase (AST) levels in schistosome-infected mice treated orally with **30**. (H) Hepatic egg granulomas and fibrotic lesions in schistosome-infected mice treated orally with **30**. (I) Western blot analysis and grayscale quantification of Collagen I and α-SMA protein levels in the livers of schistosome-infected mice treated orally with **30**. (J) Hepatic hydroxyproline contents in schistosome-infected mice treated orally with **30**. (K) Hepatic reactive oxygen species (ROS) levels in schistosome-infected mice treated orally with **30**.

compounds (≥95%) was determined by high-performance liquid chromatography (HPLC).

**4-(4-Aminophenyl)benzo[*d*]isoxazol-3-amine (B-1a).** A mixture of 4-(4,4,5,5-tetramethyl-1,3,2-dioxaborolan-2-yl)aniline (154 mg, 0.703 mmol), 4-bromobenzo[*d*]isoxazol-3-amine (100 mg, 0.469 mmol), and Pd(dppf)$Cl_2$ (68.6 mg, 0.0938 mmol) in 1,4-dioxane (10 mL) was charged with an aqueous solution of sodium carbonate (149 mg, 1.41 mmol in $H_2O$, 2 mL). The reaction mixture was degassed with $N_2$ and stirred at 110 °C for 5 h. After complete consumption of starting materials (monitored by TLC), the mixture was concentrated under reduced pressure. Purification by column chromatography on silica gel (eluent: petroleum ether/ethyl acetate, 1:1 v/v) afforded the product as


https://doi.org/10.1021/acs.jmedchem.5c03775
J. Med. Chem. XXXX, XXX, XXX−XXX

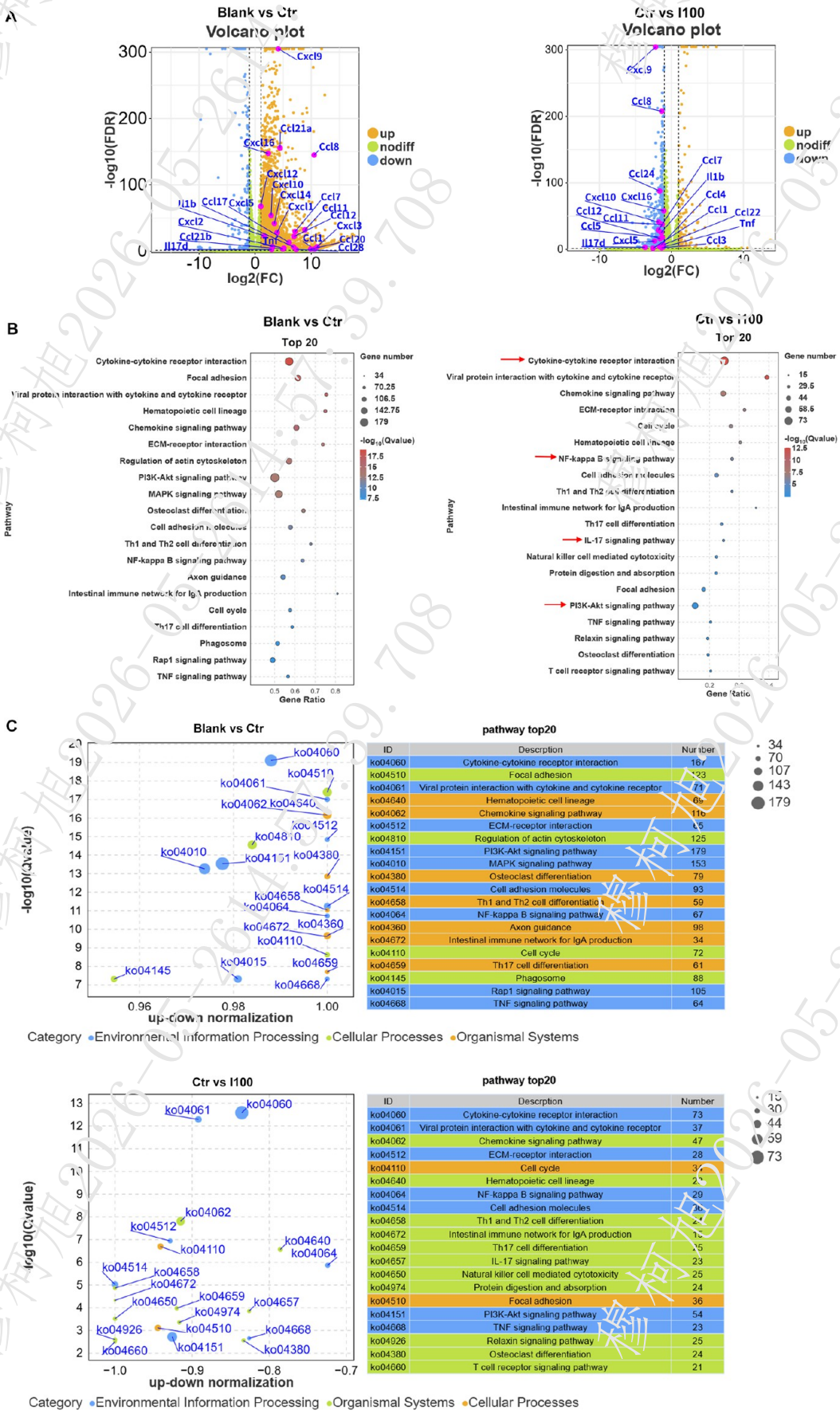


**Figure 9.** Transcriptome analysis and validation of livers from mice infected with *S. japonicum* treated orally with compound **30**. (A) Volcano plot of differentially expressed genes in the livers of schistosome-infected mice compared to healthy mice; Volcano plot of differentially expressed genes in the



https://doi.org/10.1021/acs.jmedchem.5c03775
J. Med. Chem. XXXX, XXX, XXX−XXX

**Figure** 9. continued

livers of schistosome-infected mice compared to those treated with **30** (I100) by oral gavage; (B) KEGG pathway analysis of differentially expressed genes in the livers of schistosome-infected mice compared to healthy mice; KEGG pathway analysis of differentially expressed genes in the livers of schistosome-infected mice compared to those treated with **30** (I100); (C) KEGG pathways upregulated and downregulated in the livers of schistosome-infected mice compared to healthy mice; KEGG pathways upregulated and downregulated in the livers of schistosome-infected mice compared to those treated with **30** (I100).

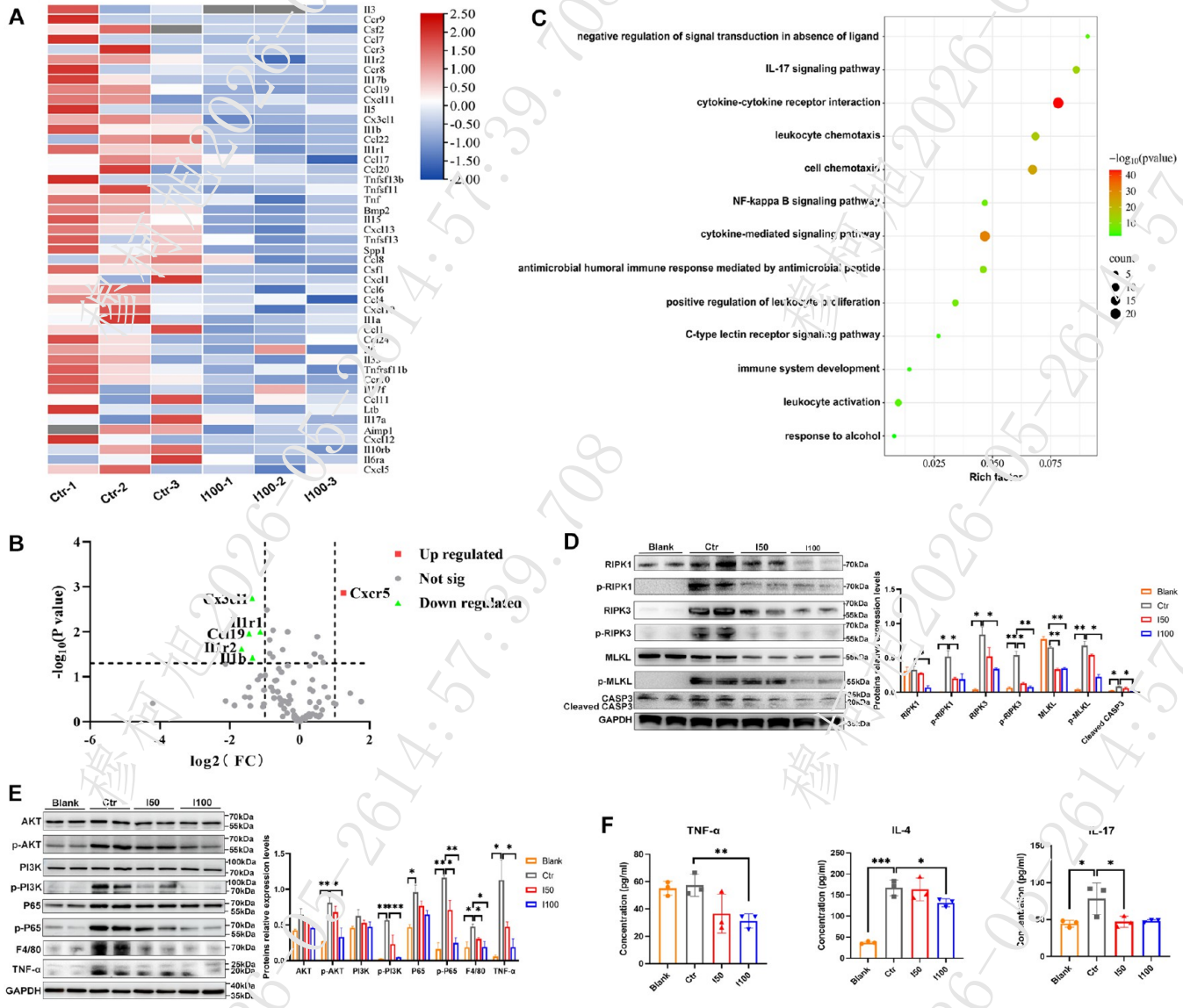


**Figure 10.** Effects of treatment **30** on inflammatory factors and signaling pathways in schistosome-infected mice. (A) Heatmap of mRNA levels of inflammatory factors and their receptors in the livers of schistosome-infected mice and those treated with **30** (I100), detected by PCR array; (B) volcano plot of differentially expressed inflammatory factors in the livers of schistosome-infected mice and those treated with **30** (I100), detected by PCR array; (C) KEGG pathway analysis of differentially expressed inflammatory factors in the livers of schistosome-infected mice and those treated with **30** (I100), detected by PCR array; (D) Western blot analysis and grayscale quantification of necroptosis and apoptosis-related protein expression in the livers of schistosome-infected mice treated with **30**; (E) Western blot analysis and grayscale quantification of AKT-PI3K/NF-κB signaling molecules and inflammatory factors F4/80 and TNF-α in the livers of schistosome-infected mice treated with **30**; (F) levels of TNF-α, IL-4, and IL-17 in the culture supernatant of splenic single cells from schistosome-infected mice treated with **30**.

a yellow solid (90.0 mg, 85.2%). mp: 101−104 °C. $^1$H NMR (300 MHz, DMSO-$d_6$) $\delta$ 7.53 (dd, $J$ = 8.4, 7.2 Hz, 1H), 7.39 (dd, $J$ = 8.4, 0.8 Hz, 1H), 7.22−7.12 (m, 2H), 7.05 (dd, $J$ = 7.3, 0.9 Hz, 1H), 6.78−6.66 (m, 2H), 5.41 (s, 2H), 5.23 (s, 2H). MS $m/z$ (ESI) $[M + H]^+$: 226.3.

**4-(4-Aminophenyl)-*N*-methylbenzo[*d*]isoxazol-3-amine (B-2a).** Following the synthetic protocol for intermediate **B-1a**, a reaction of 4-(4,4,5,5-tetramethyl-1,3,2-dioxaborolan-2-yl)aniline (565 mg, 2.58 mmol), 4-bromo-*N*-methylbenzo[*d*]isoxazol-3-amine (293 mg, 1.29 mmol), Pd(dppf)Cl$_2$ (189 mg, 0.258 mmol), and sodium carbonate (410 mg, 3.87 mmol) afforded the product as a brown solid (114 mg, 34.7%). mp: 73−76 °C. MS $m/z$ (ESI) $[M + H]^+$: 240.3.

**4-(4-Aminophenyl)-1*H*-indazol-3-amine (B-3a).** Following the synthetic protocol for intermediate **B-1a**, a reaction of 4-(4,4,5,5-tetramethyl-1,3,2-dioxaborolan-2-yl)aniline (310 mg, 1.41 mmol), 4-


https://doi.org/10.1021/acs.jmedchem.5c03775
J. Med. Chem. XXXX, XXX, XXX−XXX

bromo-1*H*-indazol-3-amine (200 mg, 0.940 mmol), $Pd(dppf)Cl_2$ (138 mg, 0.188 mmol), and sodium carbonate (299 mg, 2.82 mmol) afforded the product as a brown oil (100 mg, 47.4%). MS *m/z* (ESI) $[M + H]^+$: 225.3.

**1−1-(4-(3-Aminobenzo[*d*]isoxazol-4-yl)phenyl)-3-(3-(trifluoromethyl)phenyl)urea (1).** A solution of 2,6-difluorobenzonitrile (500 mg, 3.60 mmol) and *tert*-butyl (4-hydroxyphenyl)-carbamate (750 mg, 3.60 mmol) in anhydrous DMF (12 mL) was treated with potassium hydroxide (605 mg, 10.8 mmol). The mixture was stirred at 25 °C for 10 h. After reaction completion (TLC monitoring), the mixture was diluted with $H_2O$ (100 mL) and extracted with ethyl acetate (6 × 50 mL). The combined organic layers were washed with brine (2 × 50 mL), dried over anhydrous $Na_2SO_4$, and concentrated in vacuo. Purification by flash chromatography ($SiO_2$, petroleum ether/ethyl acetate 10:1 v/v) afforded the product as a white solid (520 mg, 44%). mp: 116−120 °C; HPLC analysis, retention time, 3.926 min; peak area, 95.73%. $^1H$ NMR (300 MHz, DMSO-$d_6$) $\delta$ 9.14 (s, 1H), 9.02 (s, 1H), 8.05 (s, 1H), 7.68−7.57 (m, 4H), 7.55−7.43 (m, 4H), 7.33 (d, $J$ = 7.6 Hz, 1H), 7.15 (d, $J$ = 7.1 Hz, 1H), 5.24 (s, 2H). $^{13}C$ NMR (75 MHz, DMSO-$d_6$) $\delta$ 163.27, 158.57, 152.96, 140.97, 140.11, 137.62, 131.17, 130.62, 130.41, 129.81, 123.91, 122.36, 120.54 (q, $^1J_{C-F}$ = 255.8 Hz), 119.01, 118.66, 114.67, 113.35, 108.83. HRMS-ESI *m/z* $[M + H]^+$ calcd for $C_{21}H_{15}F_3N_4O_2$: 413.1225, found: 413.1221.

**1−1-(4-(3-(Methylamino)benzo[*d*]isoxazol-4-yl)phenyl)-3-(3-(trifluoromethyl)phenyl)urea (2).** Following the synthetic protocol for compound **1**, a reaction of intermediate **B-2a** (114 mg, 0.477 mmol), 1-isocyanato-3-(trifluoromethyl)benzene (89.2 mg, 0.477 mmol), and triethylamine (145 mg, 1.43 mmol) afforded the product as a white solid (57 mg, 28.1%). mp: 112−114 °C; HPLC analysis, retention time, 4.325 min; peak area, 99.20%. $^1H$ NMR (300 MHz, DMSO-$d_6$) $\delta$ 9.16 (s, 1H), 9.05 (s, 1H), 8.06 (d, $J$ = 2.0 Hz, 1H), 7.65 (dd, $J$ = 9.0, 2.3 Hz, 2H), 7.62−7.52 (m, 3H), 7.49 (dd, $J$ = 8.4, 0.9 Hz, 1H), 7.46−7.41 (m, 2H), 7.34 (d, $J$ = 7.5 Hz, 1H), 7.13 (dd, $J$ = 7.2, 1.0 Hz, 1H), 4.69 (q, $J$ = 5.0 Hz, 1H), 2.78 (d, $J$ = 5.0 Hz, 3H). $^{13}C$ NMR (75 MHz, DMSO-$d_6$) $\delta$ 163.46, 159.61, 152.95, 140.99, 140.10, 137.47, 131.30, 130.49, 130.40, 129.82, 129.70, 124.03, 120.54 (q, $^1J_{C-F}$ = 255.8 Hz), 119.06, 114.65, 113.01, 108.73. HRMS-ESI *m/z* $[M + H]^+$ calcd for $C_{22}H_{18}F_3N_4O_2$: 427.1376, found: 427.1369.

**1-(4-(3-Amino-1*H*-indazol-4-yl)phenyl)-3-(3-(trifluoromethyl)phenyl)urea (3).** Following the synthetic protocol for compound **1**, a reaction of intermediate **B-3a** (100 mg, 0.446 mmol), 1-isocyanato-3-(trifluoromethyl)benzene (83.5 mg, 0.446 mmol), and triethylamine (135 mg, 1.34 mmol) afforded the product as a white solid (48 mg, 26.2%). mp: 218−220 °C; HPLC analysis, retention time, 5.802 min; peak area, 97.19%. $^1H$ NMR (300 MHz, DMSO-$d_6$) $\delta$ 10.07 (s, 1H), 9.17 (s, 1H), 9.06 (s, 1H), 8.29 (s, 1H), 8.06 (s, 1H), 7.73−7.53 (m, 5H), 7.47 (d, $J$ = 7.7 Hz, 2H), 7.34 (d, $J$ = 7.6 Hz, 1H), 7.17 (d, $J$ = 7.2 Hz, 1H), 5.22−4.96 (m, 2H). $^{13}C$ NMR (75 MHz, DMSO-$d_6$) $\delta$ 152.98, 151.31, 149.77, 140.97, 140.68, 140.08, 139.73, 136.80, 131.74, 130.41, 130.27, 129.93, 124.48, 124.12, 122.88, 122.37, 118.97, 116.54, 115.89, 114.68. HRMS-ESI *m/z* $[M-H]^-$ calcd for $C_{21}H_{17}F_3N_5O$: 410.1234, found: 410.1233.

**1-(4-(3-Aminobenzo[*d*]isoxazol-4-yl)phenyl)-3-(5-(*tert*-butyl)isoxazol-3-yl)urea (4).** A solution of 5-(*tert*-butyl)isoxazol-3-amine (312 mg, 2.22 mmol) in anhydrous $CH_2Cl_2$ (20 mL) was cooled to 0 °C under $N_2$. Triphosgene (660 mg, 2.22 mmol) was added, and the mixture was stirred for 10 min. Triethylamine (901 mg, 8.90 mmol) was added dropwise, and the reaction was warmed to 25 °C with stirring for 2 h. TLC analysis confirmed complete consumption of the amine and formation of the isocyanate intermediate. Intermediate **B-1a** (400 mg, 1.78 mmol) was then added, and stirring continued at 25 °C for 10 h. After TLC confirmation of isocyanate consumption, the mixture was concentrated in vacuo. Purification by column chromatography on silica gel (eluent: petroleum ether/ethyl acetate, 2:1 v/v) afforded the product as a white solid (20 mg, 3%). mp: 210−212 °C; HPLC analysis, retention time, 3.982 min; peak area, 99.44%. $^1H$ NMR (300 MHz, DMSO-$d_6$) $\delta$ 9.64 (s, 1H), 9.19−9.07 (m, 1H), 7.63 (d, $J$ = 8.4 Hz, 2H), 7.61−7.55 (m, 1H), 7.53−7.41 (m, 3H), 7.15 (d, $J$ = 7.1 Hz, 1H), 6.53 (s, 1H), 5.24 (s, 2H), 1.31 (s, 9H). $^{13}C$ NMR (75 MHz, DMSO-$d_6$) $\delta$ 180.71, 163.28, 158.81, 158.57, 151.83, 139.66, 137.53, 131.54, 130.61, 129.87, 123.92, 119.04, 113.36, 108.89, 92.95, 32.95, 28.81. HRMS-ESI *m/z* $[M + H]^+$ calcd for $C_{21}H_{21}N_5O_3$: 392.1723, found: 392.1726.

**1-(4-(3-Aminobenzo[d]isoxazol-4-yl)phenyl)-3-cyclohexylurea (5).** Following the synthetic protocol for compound **4**, a reaction of intermediate **B-1a** (400 mg, 1.78 mmol), cyclohexylamine (220 mg, 2.22 mmol), triphosgene (660 mg, 2.22 mmol), and triethylamine (901 mg, 8.90 mmol) afforded the product as a white solid (30 mg, 5.1%). mp: 218−220 °C; HPLC analysis, retention time, 3.737 min; peak area, 95.41%. $^1H$ NMR (300 MHz, DMSO-$d_6$) $\delta$ 8.53 (s, 1H), 7.64−7.51 (m, 3H), 7.47 (d, $J$ = 8.3 Hz, 1H), 7.37 (d, $J$ = 8.6 Hz, 2H), 7.12 (d, $J$ = 7.1 Hz, 1H), 6.18 (d, $J$ = 7.8 Hz, 1H), 5.23 (s, 2H), 3.49 (d, $J$ = 8.7 Hz, 1H), 1.90−1.76 (m, 2H), 1.73−1.63 (m, 2H), 1.60−1.50 (m, 1H), 1.35−1.15 (m, 5H). $^{13}C$ NMR (151 MHz, DMSO-$d_6$) $\delta$ 163.26, 158.55, 154.82, 141.36, 137.86, 130.56, 129.89, 129.54, 123.78, 118.01, 113.37, 108.62, 48.11, 33.40, 25.72, 24.80. HRMS-ESI *m/z* $[M + H]^+$ calcd for $C_{21}H_{21}N_5O_3$: 351.1816, found: 351.1813.

**1-(4-(3-Aminobenzo[*d*]isoxazol-4-yl)phenyl)-3-cyclopropylurea (6).** Following the synthetic protocol for compound **4**, a reaction of intermediate **B-1a** (400 mg, 1.78 mmol), cyclopropylamine (127 mg, 2.22 mmol), triphosgene (660 mg, 2.22 mmol), and triethylamine (901 mg, 8.90 mmol) afforded the product as a white solid (41 mg, 7.5%). HPLC analysis, retention time, 4.270 min; peak area, 98.64%. $^1H$ NMR (300 MHz, DMSO-$d_6$) $\delta$ 8.53 (s, 1H), 7.67−7.32 (m, 6H), 7.12 (d, $J$ = 7.2 Hz, 1H), 6.49 (s, 1H), 5.21 (s, 2H), 1.33−1.15 (m, 1H), 0.66 (d, $J$ = 6.8 Hz, 2H), 0.43 (s, 2H). $^{13}C$ NMR (101 MHz, DMSO-$d_6$) $\delta$ 163.23, 158.54, 156.49, 141.09, 137.80, 130.65, 130.13, 129.60, 123.85, 118.40, 113.30, 108.68, 22.88, 6.90. HRMS-ESI *m/z* $[M + H]^+$ calcd for $C_{21}H_{21}N_5O_3$: 309.1346, found: 309.1338.

**1-(4-(3-Aminobenzo[*d*]isoxazol-4-yl)phenyl)-3-(tetrahydro-2*H*-pyran-4-yl)urea (7).** Following the synthetic protocol for compound **4**, a reaction of intermediate **B-1a** (400 mg, 1.78 mmol), tetrahydro-2*H*-pyran-4-amine (225 mg, 2.22 mmol), triphosgene (660 mg, 2.22 mmol), and triethylamine (901 mg, 8.90 mmol) afforded the product as a white solid (33 mg, 5%). mp: 245−246 °C; HPLC analysis, retention time, 3.379 min; peak area, 97.02%. $^1H$ NMR (300 MHz, DMSO-$d_6$) $\delta$ 8.58 (s, 1H), 7.62−7.51 (m, 3H), 7.47 (d, $J$ = 8.3 Hz, 1H), 7.38 (d, $J$ = 8.2 Hz, 2H), 7.12 (d, $J$ = 7.1 Hz, 1H), 6.30 (d, $J$ = 7.6 Hz, 1H), 5.22 (s, 2H), 3.83 (m, 2H), 3.76−3.63 (m, 1H), 3.42 (d, $J$ = 11.0 Hz, 2H), 1.81 (d, $J$ = 13.0 Hz, 2H), 1.48−1.33 (m, 2H). $^{13}C$ NMR (75 MHz, DMSO-$d_6$) $\delta$ 163.23, 152.55, 154.84, 141.20, 137.82, 130.59, 129.99, 129.67, 123.81, 118.08, 113.33, 108.65, 66.31, 45.79, 33.59. HRMS-ESI *m/z* $[M + H]^+$ calcd for $C_{21}H_{15}F_3N_4O_3$: 353.1599, found: 353.1608

***tert*-Butyl 4-(3-(4-(3-Aminobenzo[*d*]isoxazol-4-yl)phenyl)-ureido)piperidine-1-carboxylate (B-8b).** Following the synthetic protocol for compound **4**, a reaction of intermediate **B-1a** (400 mg, 1.78 mmol), *tert*-butyl 4-aminopiperidine-1-carboxylate (445 mg, 2.22 mmol), triphosgene (660 mg, 2.22 mmol), and triethylamine (901 mg, 8.90 mmol) afforded the product as a yellow solid (120 mg, 15%). MS *m/z* (ESI) $[M + H]^+$: 409.2.

**1-(4-(3-Aminobenzo[*d*]isoxazol-4-yl)phenyl)-3-(piperidin-4-yl)urea (8).** A solution of intermediate **B-8b** (120 mg, 0.266 mmol) in dichloromethane (5 mL) was treated with trifluoroacetic acid (1 mL). The reaction mixture was stirred at 25 °C for 1 h. After complete deprotection (confirmed by TLC), the solution was concentrated under reduced pressure. The residue was diluted with $H_2O$ (20 mL), adjusted to pH 8 with saturated $NaHCO_3$(aq), and extracted with ethyl acetate (5 × 20 mL). The combined organic layers were washed with brine (2 × 20 mL), dried over anhydrous $Na_2SO_4$, and concentrated in vacuo to afford the product as a white solid (30 mg, 32%). mp: 204−206 °C; HPLC analysis, retention time, 3.625 min; peak area, 98.76%. $^1H$ NMR (300 MHz, DMSO-$d_6$) $\delta$ 8.91 (s, 1H), 7.55 (d, $J$ = 7.9 Hz, 3H), 7.46 (d, $J$ = 8.2 Hz, 1H), 7.37 (d, $J$ = 8.1 Hz, 2H), 7.11 (d, $J$ = 7.2 Hz, 1H), 6.74 (s, 1H), 5.21 (s, 2H), 3.70 (s, 1H), 3.15 (d, $J$ = 13.1 Hz, 2H), 2.85 (t, $J$ = 11.1 Hz, 2H), 1.99 (s, 1H), 1.91 (d, $J$ = 13.4 Hz, 2H), 1.49 (d, $J$ = 10.7 Hz, 2H). $^{13}C$ NMR (151 MHz, DMSO-$d_6$) $\delta$ 163.25, 158.55, 155.04, 141.31, 137.86, 130.58, 129.95, 129.65, 123.81, 118.00, 113.37, 108.64, 44.83, 43.02, 30.36. HRMS-ESI *m/z* $[M + H]^+$ calcd for $C_{21}H_{21}N_5O_3$: 352.1773, found: 352.1777.


https://doi.org/10.1021/acs.jmedchem.5c03775
J. Med. Chem. XXXX, XXX, XXX−XXX

**1-(4-(3-Aminobenzo[*d*]isoxazol-4-yl)phenyl)-3-(3-isopropoxyphenyl)urea (9).** Following the synthetic protocol for compound **4**, a reaction of intermediate **B-1a** (400 mg, 1.78 mmol), 3-isopropoxyaniline (336 mg, 2.22 mmol), triphosgene (660 mg, 2.22 mmol), and triethylamine (901 mg, 8.90 mmol) afforded the product as a white solid (69 mg, 9.5%). HPLC analysis, retention time, 4.083 min; peak area, 96.64%. $^1$H NMR (300 MHz, DMSO-$d_6$) $\delta$ 8.89 (s, 1H), 8.74 (s, 1H), 7.67−7.56 (m, 3H), 7.52−7.40 (m, 3H), 7.20 (t, $J$ = 2.4 Hz, 1H), 7.18−7.12 (m, 2H), 6.95−6.88 (m, 1H), 6.60−6.48 (m, 1H), 5.23 (s, 2H), 4.56 (p, $J$ = 6.0 Hz, 1H), 1.28 (s, 3H), 1.27 (s, 3H). $^{13}$C NMR (101 MHz, DMSO-$d_6$) $\delta$ 163.28, 158.57, 158.36, 152.93, 141.31, 140.44, 137.70, 130.83, 130.62, 130.04, 129.79, 123.89, 118.73, 113.37, 110.87, 109.57, 108.78, 106.17, 69.53, 22.34. HRMS-ESI $m/z$ [M + H]$^+$ calcd for $C_{21}H_{21}N_3O_3$: 403.1765, found: 403.1769.

**1-(4-(3-Aminobenzo[*d*]isoxazol-4-yl)phenyl)-3-(3-(trifluoromethoxy)phenyl)urea (10).** Following the synthetic protocol for compound **4**, a reaction of intermediate **B-1a** (180 mg, 0.799 mmol), 3-(trifluoromethoxy)aniline (170 mg, 0.956 mmol), triphosgene (284 mg, 0.956 mmol), and triethylamine (387 mg, 3.82 mmol) afforded the product as a white solid (125 mg, 36.6%). mp: 200−202 °C; HPLC analysis, retention time, 4.066 min; peak area, 97.43%. $^1$H NMR (300 MHz, DMSO-$d_6$) $\delta$ 9.11 (s, 1H), 9.01 (s, 1H), 7.74 (s, 1H), 7.68−7.57 (m, 3H), 7.53−7.41 (m, 4H), 7.37−7.31 (m, 1H), 7.16 (dd, $J$ = 7.2, 0.9 Hz, 1H), 7.02−6.94 (m, 1H), 5.25 (s, 2H). $^{13}$C NMR (75 MHz, DMSO-$d_6$) $\delta$ 163.27, 158.56, 152.85, 149.22, 149.20, 149.18, 141.89, 140.10, 137.62, 131.16, 130.86, 130.59, 129.79, 123.89, 120.58 (q, $^1J_{C-F}$ = 190.5 Hz), 118.98, 117.33, 114.23, 113.36, 110.71, 108.81. HRMS-ESI $m/z$ [M + H]$^+$ calcd for $C_{21}H_{15}F_3N_4O_3$: 429.1175, found: 429.1178.

**5-(4,4,5,5-Tetramethyl-1,3,2-dioxaborolan-2-yl)pyridin-2-amine (B-11a).** A mixture of 2-amino-5-bromopyridine (500 mg, 2.89 mmol), bis(pinacolato)diboron (984 mg, 3.76 mmol), Pd(dppf)Cl$_2$ (212 mg, 0.289 mmol), and potassium acetate (567 mg, 5.78 mmol) in anhydrous 1,4-dioxane (15 mL) was degassed with $N_2$ and stirred at 110 °C for 5 h. After complete consumption of the starting material (TLC monitoring), the reaction mixture was concentrated under reduced pressure. Purification by column chromatography on silica gel (eluent: petroleum ether/ethyl acetate, 10:1 v/v) afforded the product as a yellow solid (501 mg, 79%). mp: 131−135 °C. MS $m/z$ (ESI) [M + H]$^+$: 221.2.

**4-(6-Aminopyridin-3-yl)benzo[*d*]isoxazol-3-amine (B-11b).** Following the synthetic protocol for intermediate **B-1a**, a reaction of intermediate **B-11a** (501 mg, 2.27 mmol), 4-bromobenzo[*d*]isoxazol-3-amine (400 mg, 1.76 mmol), Pd(dppf)Cl$_2$ (258 mg, 0.352 mmol), and sodium carbonate (561 mg, 5.29 mmol) afforded the product as a yellow solid (203 mg, 51%). $^1$H NMR (300 MHz, DMSO-$d_6$) $\delta$ 8.05 (m, 1H), 7.56−7.50 (m, 2H), 7.44 (m, 1H), 7.09 (dd, $J$ = 7.2, 0.9 Hz, 1H), 6.57 (m, 1H), 6.26 (s, 2H), 5.29 (s, 2H). MS $m/z$ (ESI) [M + H]$^+$: 227.3.

**1-(5-(3-Aminobenzo[*d*]isoxazol-4-yl)pyridin-2-yl)-3-(3-(trifluoromethoxy)phenyl)urea (11).** Following the synthetic protocol for compound **4**, a reaction of 3-(trifluoromethoxy)aniline (196 mg, 1.10 mmol), triphosgene (328 mg, 1.10 mmol), triethylamine (448 mg, 4.42 mmol), and intermediate **B-11b** (200 mg, 0.884 mmol) afforded the product as a white solid (44 mg, 13%). mp 190−192 °C; HPLC analysis, retention time, 4.281 min; peak area, 97.55%. $^1$H NMR (300 MHz, DMSO-$d_6$) $\delta$ 10.78 (s, 1H), 9.74 (s, 1H), 8.46 (s, 1H), 7.94 (d, $J$ = 8.6 Hz, 1H), 7.82 (s, 1H), 7.70−7.62 (m, 2H), 7.56 (d, $J$ = 7.7 Hz, 1H), 7.48−7.42 (m, 2H), 7.24−7.19 (m, 1H), 7.06−7.00 (m, 1H), 5.41 (s, 2H). $^{13}$C NMR (75 MHz, DMSO-$d_6$) $\delta$ 163.47, 158.82, 152.78, 152.57, 149.22, 147.05, 141.23, 139.52, 134.19, 131.01, 130.70, 127.27, 124.31, 120.58 (q, $^1J_{C-F}$ = 254.2 Hz), 118.88, 117.92, 114.92, 113.67, 112.10, 111.34, 109.46. HRMS-ESI $m/z$ [M + H]$^+$ calcd for $C_{20}H_{14}F_3N_5O_3$: 430.1127, found: 430.1129.

**(4-(4,4,5,5-Tetramethyl-1,3,2-dioxaborolan-2-yl)phenyl)-methanamine (B-12a).** Following the synthetic protocol for intermediate **B-11a**, a reaction of 4-bromobenzylamine (500 mg, 2.69 mmol), bis(pinacolato)diboron (889 mg, 3.50 mmol), Pd(dppf)Cl$_2$ (197 mg, 0.269 mmol), and potassium acetate (528 mg, 5.38 mmol) afforded the product as a yellow solid (500 mg, 78%). MS $m/z$ (FSI) [M + H]$^+$: 234.2.

**4-(4-(Aminomethyl)phenyl)benzo[*d*]isoxazol-3-amine (B-12b).** Following the synthetic protocol for intermediate **B-1a**, a reaction of intermediate **B-12a** (500 mg, 2.09 mmol), 4-bromobenzo-[*d*]isoxazol-3-amine (432 mg, 1.90 mmol), Pd(dppf)Cl$_2$ (139 mg, 0.190 mmol), and sodium carbonate (604 mg, 5.70 mmol) afforded the product as a yellow solid (300 mg, 66%). MS $m/z$ (ESI) [M + H]$^+$: 240.3.

**1-(4-(3-Aminobenzo[*d*]isoxazol-4-yl)benzyl)-3-(3-(trifluoromethoxy)phenyl)urea (12).** Following the synthetic protocol for compound **4**, a reaction of 3-(trifluoromethoxy)aniline (139 mg, 0.780 mmol), intermediate **B-12b** (150 mg, 0.630 mmol), triphosgene (231 mg, 0.780 mmol), and triethylamine (316 mg, 3.12 mmol) afforded the product as a white solid (30 mg, 11%). mp 100−102 °C; HPLC analysis, retention time, 3.809 min; peak area, 97.06%. $^1$H NMR (300 MHz, DMSO-$d_6$) $\delta$ 9.01 (s, 1H), 7.70 (s, 1H), 7.61 (m, 1H), 7.54 (s, 1H), 7.49 (d, $J$ = 1.3 Hz, 4H), 7.35 (t, $J$ = 8.1 Hz, 1H), 7.30−7.22 (m, 1H), 7.15 (d, $J$ = 7.0 Hz, 1H), 6.87 (m, 2H), 5.19 (s, 2H), 4.41 (d, $J$ = 5.9 Hz, 2H). $^{13}$C NMR (151 MHz, DMSO-$d_6$) $\delta$ 163.23, 158.48, 155.55, 149.23, 142.76, 140.95, 137.60, 136.06, 130.68, 130.64, 129.25, 127.99, 124.00, 120.59 (q, $^1J_{C-F}$ = 256.7 Hz), 116.75, 113.39, 110.16, 109.15, 42.95, 40.56. HRMS-ESI $m/z$ [M + H]$^+$ calcd for $C_{20}H_{14}F_3N_5O_3$: 443.1331, found: 443.1314.

**3-(4,4,5,5-Tetramethyl-1,3,2-dioxaborolan-2-yl)aniline (B-14a).** Following the synthetic protocol for intermediate **B-11a**, a reaction of 3-bromoaniline (500 mg, 2.91 mmol), bis(pinacolato)-diboron (960 mg, 3.78 mmol), Pd(dppf)Cl$_2$ (213 mg, 0.291 mmol), and potassium acetate (571 mg, 5.82 mmol) afforded the product as a yellow oil (500 mg, 78%).MS $m/z$ (ESI) [M + H]$^+$: 220.3.

**4-(3-Aminophenyl)benzo[*d*]isoxazol-3-amine (B-14b).** Following the synthetic protocol for intermediate **B-1a**, a reaction of intermediate **B-14a** (500 mg, 2.28 mmol), 4-bromobenzo[*d*]isoxazol-3-amine (400 mg, 1.76 mmol), Pd(dppf)Cl$_2$ (129 mg, 0.176 mmol), and sodium carbonate (560 mg, 5.28 mmol) afforded the product as a yellow solid (300 mg, 76%). mp 142−148 °C. $^1$H NMR (300 MHz, DMSO-$d_6$) $\delta$ 7.57 (m, 1H), 7.51−7.43 (m, 1H), 7.18 (t, $J$ = 7.7 Hz, 1H), 7.11 (d, $J$ = 7.0 Hz, 1H), 6.73−6.62 (m, 2H), 6.61−6.52 (m, 1H), 5.45−5.33 (m, 2H), 5.30 (s, 2H). MS $m/z$ (ESI) [M + H]$^+$: 226.3

**1-(3-(3-Aminobenzo[*d*]isoxazol-4-yl)phenyl)-3-(3-(trifluoromethoxy)phenyl)urea (14).** Following the synthetic protocol for compound **4**, a reaction of 3-(trifluoromethoxy)aniline (295 mg, 1.66 mmol), intermediate **B-14b** (300 mg, 1.33 mmol), triphosgene (493 mg, 1.66 mmol), and triethylamine (672 mg, 6.64 mmol) afforded the product as a white solid (40 mg, 12%). mp 210−212 °C; HPLC analysis, retention time, 4.029 min; peak area, 98.14%. $^1$H NMR (300 MHz, DMSO-$d_6$) $\delta$ 9.12 (s, 1H), 9.01 (s, 1H), 7.76−7.44 (m, 6H), 7.37 (d, $J$ = 21.6 Hz, 1H), 7.31 (s, 1H), 7.17 (m, 2H), 6.96 (d, $J$ = 8.1 Hz, 1H), 5.36 (s, 2H). HRMS-ESI $m/z$ [M + H]$^+$ calcd for $C_{20}H_{14}F_3N_5O_3$: 429.1166, found: 429.1166.

**5-(4,4,5,5-Tetramethyl-1,3,2-dioxaborolan-2-yl)indoline (B-17a).** Following the synthetic protocol for intermediate **B-11a**, a reaction of 5-bromoindoline (1.0 g, 5.04 mmol), bis(pinacolato)-diboron (1.02 g, 4.32 mmol), Pd(dppf)Cl$_2$ (274 mg, 0.336 mmol), and potassium acetate (658 mg, 6.72 mmol) afforded the product as a yellow solid (764 mg, 58.9%). mp 82−87 °C. $^1$H NMR (300 MHz, Chloroform-$d$) $\delta$ 7.83 (dt, $J$ = 6.7, 1.5 Hz, 1H), 7.70−7.59 (m, 2H), 3.99 (t, $J$ = 8.7 Hz, 2H), 3.09 (ddd, $J$ = 9.5, 8.1, 1.1 Hz, 2H), 1.36 (d, $J$ = 4.4 Hz, 9H), 1.28 (s, 12H). MS $m/z$ (ESI) [M + H]$^+$: 246.3.

**4-(Indolin-5-yl)benzo[*d*]isoxazol-3-amine (B-17b).** Following the synthetic protocol for intermediate **B-1a**, a reaction of intermediate **B-17a** (764 mg, 2.97 mmol), 4-bromobenzo[*d*]isoxazol-3-amine (421 mg, 1.98 mmol), Pd(dppf)Cl$_2$ (289 mg, 0.396 mmol), and sodium carbonate (629 mg, 5.94 mmol) afforded the product as a yellow oil (358 mg, 72%). MS $m/z$ (ESI) [M + H]$^+$: 252.3.

**5-(3-Aminobenzo[*d*]isoxazol-4-yl)-*N*-(3-(trifluoromethoxy)-phenyl)indoline-1-carboxamide (17).** Following the synthetic protocol for compound **4**, a reaction of intermediate **B-17b** (40.0 mg, 0.159 mmol), 3-(trifluoromethoxy)aniline (33.8 mg, 0.191 mmol), triphosgene (56.7 mg, 0.191 mmol), and triethylamine (77.3 mg, 0.764


https://doi.org/10.1021/acs.jmedchem.5c03775
J. Med. Chem. XXXX, XXX, XXX−XXX

mmol) afforded the product as a white solid (32 mg, 44.0%). mp 89−92 °C; HPLC analysis, retention time, 4.383 min; peak area, 97.71%. $^1$H NMR (300 MHz, Chloroform-*d*) $\delta$ 8.38 (d, $J$ = 8.8 Hz, 1H), 7.53 (dd, $J$ = 8.5, 7.2 Hz, 1H), 7.45−7.39 (m, 2H), 7.37−7.28 (m, 4H), 7.24−7.17 (m, 2H), 7.12 (dd, $J$ = 7.2, 0.9 Hz, 1H), 4.21 (t, $J$ = 8.5 Hz, 2H), 3.89 (s, 2H), 3.32 (t, $J$ = 8.4 Hz, 2H). HRMS-ESI $m/z$ [M + H]$^+$ calcd for $C_{23}H_{17}F_3N_4O_3$: 455.1331, found: 455.1331.

**6-(4,4,5,5-Tetramethyl-1,3,2-dioxaborolan-2-yl)-1,2,3,4-tetrahydroquinoline (B-18a).** Following the synthetic protocol for intermediate **B-11a**, a reaction of 6-bromo-1,2,3,4-tetrahydroquinoline (1.0 g, 4.71 mmol), bis(pinacolato)diboron (1.43 g, 5.65 mmol), Pd(dppf)$Cl_2$ (345 mg, 0.471 mmol), and potassium acetate (924 mg, 9.42 mmol) afforded the product as a yellow solid (0.25 g, 20%). mp 75−78 °C. MS $m/z$ (ESI) [M + H]$^+$: 260.3.

**4-(1,2,3,4-Tetrahydroquinolin-6-yl)benzo[*d*]isoxazol-3-amine (B-18b).** Following the synthetic protocol for intermediate **B-1a**, a reaction of intermediate **B-18a** (250 mg, 0.965 mmol), 4-bromobenzo[*d*]isoxazol-3-amine (137 mg, 0.643 mmol), Pd(dppf)$Cl_2$ (73.2 mg, 0.0643 mmol), and sodium carbonate (204 mg, 1.929 mmol) afforded the product as a yellow oil (90 mg, 53%). MS $m/z$ (ESI) [M + H]$^+$: 266.3.

**6-(3-Aminobenzo[*d*]isoxazol-4-yl)-*N*-(3-(trifluoromethoxy)-phenyl)-3,4-dihydroquinoline-1(2*H*)-carboxamide (18).** Following the synthetic protocol for compound **4**, a reaction of intermediate **B-22b** (90.0 mg, 0.340 mmol), 3-(trifluoromethoxy)aniline (72.3 mg, 0.408 mmol), triphosgene (121 mg, 0.408 mmol), and triethylamine (165 mg, 1.63 mmol) afforded the product as a white solid (49 mg, 31%). mp 96−100 °C. $^1$H NMR (300 MHz, DMSO-$d_6$) $\delta$ 9.28 (s, 1H), 7.69 (m, 1H), 7.59 (dd, $J$ = 8.4, 7.1 Hz, 1H), 7.52−7.45 (m, 3H), 7.39 (t, $J$ = 8.1 Hz, 1H), 7.34 (d, $J$ = 2.1 Hz, 1H), 7.25 (dd, $J$ = 8.4, 2.2 Hz, 1H), 7.16 (dd, $J$ = 7.2, 0.9 Hz, 1H), 6.96 (ddt, $J$ = 8.0, 2.4, 1.2 Hz, 1H), 5.40 (s, 2H), 3.78 (dd, $J$ = 6.8, 5.4 Hz, 2H), 2.85 (t, $J$ = 6.5 Hz, 2H), 1.99−1.92 (m, 2H). $^{13}$C NMR (75 MHz, DMSO-$d_6$) $\delta$ 163.24, 158.51, 154.64, 148.99, 148.96, 142.34, 139.37, 137.57, 132.08, 131.19, 130.55, 130.52, 129.47, 127.09, 123.81, 123.71, 120.58 (q, $^1J_{C-F}$ = 254.2 Hz), 118.34, 114.48, 113.33, 111.77, 108.89, 44.85, 27.08, 23.79. HRMS-ESI $m/z$ [M + H]$^+$ calcd for $C_{24}H_{20}F_3N_4O_3$: 469.1482, found: 469.1492.

**2-Methyl-4-(4,4,5,5-tetramethyl-1,3,2-dioxaborolan-2-yl)-aniline (B-21a).** Following the synthetic protocol for intermediate **B-11a**, a reaction of 4-bromo-2-methylaniline (500 mg, 2.69 mmol) and bis(pinacolato)diboron (887 mg, 3.49 mmol) afforded the product as a yellow solid (510 mg, 82%). MS $m/z$ (ESI) [M + H]$^+$: 234.1.

**4-(4-Amino-3-methylphenyl)benzo[*d*]isoxazol-3-amine (B-21b).** Following the synthetic protocol for intermediate **B-1a**, a reaction of intermediate **B-21a** (500 mg, 2.15 mmol), 4-bromobenzo-[*d*]isoxazol-3-amine (374 mg, 1.65 mmol), Pd(dppf)$Cl_2$ (121 mg, 0.165 mmol), and sodium carbonate (524 mg, 4.95 mmol) afforded the product as a yellow solid (265 mg, 67%). MS $m/z$ (ESI) [M + H]$^+$: 240.1.

**1-(4-(3-Aminobenzo[*d*]isoxazol-4-yl)-2-methylphenyl)-3-(3-(trifluoromethoxy)phenyl)urea (21).** Following the synthetic protocol for compound **4**, a reaction of **B-21b** (200 mg, 0.880 mmol) and 3-(trifluoromethoxy)aniline (196 mg, 1.10 mmol) yielded the product as a white solid (48.0 mg, 10%). mp: 180−182 °C; HPLC analysis, retention time, 4.151 min; peak area, 95.87%. $^1$H NMR (300 MHz, DMSO-$d_6$) $\delta$ 9.46 (s, 1H), 8.19 (s, 1H), 8.05 (d, $J$ = 8.3 Hz, 1H), 7.76 (s, 1H), 7.59 (m, 1H), 7.52−7.41 (m, 2H), 7.38−7.27 (m, 3H), 7.15 (m, 1H), 6.97 (m, 1H), 5.25 (s, 2H), 2.35 (s, 3H). HRMS-ESI $m/z$ [M + H]$^+$ calcd for $C_{24}H_{20}F_3N_4O_3$: 443.1331, found: 443.1320

**3-Methyl-4-(4,4,5,5-tetramethyl-1,3,2-dioxaborolan-2-yl)-aniline (B-22a).** Following the synthetic protocol for intermediate **B-11a**, a reaction of 4-bromo-3-methylaniline (500 mg, 2.69 mmol) and bis(pinacolato)diboron (830 mg, 3.49 mmol) afforded the product as a yellow solid (520 mg, 83%). MS $m/z$ (ESI) [M + H]$^+$: 213.4.

**4-(4-Amino-2-methylphenyl)benzo[*d*]isoxazol-3-amine (B-22b).** Following the synthetic protocol for intermediate **B-1a**, a reaction of **B-22a** (500 mg, 2.15 mmol) and 4-bromobenzo[*d*]isoxazol-3-amine (418 mg, 1.65 mmol) afforded the product as a yellow solid (254 mg, 65%). MS $m/z$ (ESI) [M + H]$^+$: 234.1.

**1-(4-(3-Aminobenzo[*d*]isoxazol-4-yl)-3-methylphenyl)-3-(3-(trifluoromethoxy)phenyl)urea (22).** Following the synthetic protocol for compound **4**, a reaction of 3-(trifluoromethoxy)aniline (235 mg, 1.33 mmol) and intermediate **B-22b** (254 mg, 1.06 mmol) afforded the product as a white solid (50 mg, 11%). mp: 100−102 °C; HPLC analysis, retention time, 6.513 min; peak area, 98.81%. $^1$H NMR (300 MHz, DMSO-$d_6$) $\delta$ 9.15 (d, $J$ = 2.8 Hz, 1H), 8.97 (d, $J$ = 2.8 Hz, 1H), 7.76 (s, 1H), 7.60 (m, 1H), 7.51 (m, 2H), 7.42 (m, 2H), 7.32 (d, $J$ = 8.3 Hz, 1H), 7.19 (m, 1H), 7.05 (m, 1H), 6.97 (d, $J$ = 8.0 Hz, 1H), 4.97 (s, 2H), 2.07 (d, $J$ = 2.9 Hz, 3H). $^{13}$C NMR (151 MHz, DMSO-$d_6$) $\delta$ 162.65, 158.58, 152.89, 149.24, 141.94, 140.11, 136.67, 136.62, 130.85, 130.58, 130.47, 130.23, 120.60 (q, $^1J_{C-F}$ = 256.7 Hz), 120.24, 117.32, 116.42, 114.59, 114.20, 110.71, 108.98, 20.32. HRMS-ESI $m/z$ [M + H]$^+$ calcd for $C_{22}H_{17}F_3N_4O_3$: 443.1331, found: 443.1334.

**2-Fluoro-4-(4,4,5,5-tetramethyl-1,3,2-dioxaborolan-2-yl)-aniline (B-23a).** Following the synthetic protocol for intermediate **B-11a**, a reaction of 4-bromo-2-fluoroaniline (500 mg, 2.63 mmol) and bis(pinacolato)diboron (1002 mg, 3.95 mmol) afforded the product as a yellow solid (334.0 mg, 84%). MS $m/z$ (ESI) [M + H]$^+$: 213.4.

**4-(4-Amino-3-fluorophenyl)benzo[*d*]isoxazol-3-amine (B-23b).** Following the synthetic protocol for intermediate **B-1a**, a reaction of **B-23a** (334 mg, 1.41 mmol) and 4-bromobenzo[*d*]isoxazol-3-amine (200 mg, 0.939 mmol) afforded the product as a yellow oil (55 mg, 24%). MS $m/z$ (ESI) [M + H]$^+$: 243.3.

**1-(4-(3-Aminobenzo[*d*]isoxazol-4-yl)-2-fluorophenyl)-3-(3-(trifluoromethoxy)phenyl)urea (23).** Following the synthetic protocol for compound **4**, a reaction of intermediate **B-23b** (55.0 mg, 0.227 mmol) and 3-(trifluoromethoxy)aniline (48.0 mg, 0.272 mmol) afforded the product as a white solid (30 mg, 27%). mp: 198−200 °C; HPLC analysis, retention time, 4.260 min; peak area, 97.01%. $^1$H NMR (300 MHz, DMSO-$d_6$) $\delta$ 9.48 (s, 1H), 8.82 (d, $J$ = 2.7 Hz, 1H), 8.33 (t, $J$ = 8.5 Hz, 1H), 7.77−7.75 (m, 1H), 7.61 (dd, $J$ = 8.5, 7.1 Hz, 1H), 7.53 (dd, $J$ = 8.5, 1.0 Hz, 1H), 7.47−7.41 (m, 2H), 7.33 (dd, $J$ = 8.1, 1.9 Hz, 2H), 7.19 (dd, $J$ = 7.1, 1.0 Hz, 1H), 7.02−6.98 (m, 1H), 5.34 (s, 2H). $^{13}$C NMR (151 MHz, DMSO-$d_6$) $\delta$ 163.37, 158.56, 152.52 (d, $^1J_{C-F}$ = 241.6 Hz), 152.25, 149.29, 141.73, 141.61, 136.37, 131.94 (d, $^3J_{C-F}$ = 7.4 Hz), 130.96, 130.81, 130.54, 127.39 (d, $^2J_{C-F}$ = 10.4 Hz), 125.58 (d, $^3J_{C-F}$ = 3.0 Hz), 124.08, 120.98, 120.60 (q, $^1J_{C-F}$ = 255.2 Hz), 117.49, 117.22, 116.05 (d, $^2J_{C-F}$ = 21.1 Hz), 114.45, 114.37, 113.38, 110.91, 110.61, 109.25. HRMS-ESI $m/z$ [M + H]$^+$ calcd for $C_{21}H_{14}F_4N_4O_3$: 447.1080, found: 447.1076

**3-Fluoro-4-(4,4,5,5-tetramethyl-1,3,2-dioxaborolan-2-yl)-aniline (B-24a).** Following the synthetic protocol for intermediate **B-11a**, a reaction of 4-bromo-3-fluoroaniline (500 mg, 2.63 mmol) and bis(pinacolato)diboron (869 mg, 3.42 mmol) afforded the product as a yellow solid (504 mg, 81%). MS $m/z$ (ESI) [M + H]$^+$: 237.9.

**4-(4-Amino-2-fluorophenyl)benzo[*d*]isoxazol-3-amine (B-24b).** Following the synthetic protocol for intermediate **B-1a**, a reaction of **B-24a** (500 mg, 2.11 mmol) and 4-bromobenzo[*d*]isoxazol-3-amine (435 mg, 1.92 mmol) afforded the product as a yellow solid (300 mg, 65%). MS $m/z$ (ESI) [M + H]$^+$: 244.1.

**1-(4-(3-Aminobenzo[*d*]isoxazol-4-yl)-3-fluorophenyl)-3-(3-(trifluoromethoxy)phenyl)urea (24).** Following the synthetic protocol for compound **4**, a reaction of 3-(trifluoromethoxy)aniline (273 mg, 1.54 mmol) and intermediate **B-24b** (300 mg, 1.23 mmol) afforded the product as a white solid (70 mg, 13%). mp: 196−198 °C; HPLC analysis, retention time, 3.986 min; peak area, 98.89%. $^1$H NMR (300 MHz, DMSO-$d_6$) $\delta$ 9.22 (s, 1H), 9.20 (s, 1H), 7.72 (s, 1H), 7.69−7.63 (m, 1H), 7.62−7.56 (m, 1H), 7.54 (m, 1H), 7.49−7.35 (m, 3H), 7.31 (m, 1H), 7.16 (d, $J$ = 7.0 Hz, 1H), 6.99 (m, 1H), 5.20 (s, 2H).$^{13C}$ NMR (75 MHz, DMSO-$d_6$) $\delta$ 163.00, 159.38 (d, $^1J_{C-F}$ = 241.5 Hz), 157.77, 152.76, 149.19, 142.12 (d, $^2J_{C-F}$ = 11.25 Hz), 141.67, 132.04 (d, $^1J_{C-F}$ = 3.75 Hz), 130.92, 130.67, 130.45, 124.87, 120.58 (q, $^1J_{C-F}$ = 254.25 Hz), 117.97, 117.75, 117.50, 114.71 (d, $^1J_{C-F}$ = 3.00 Hz), 114.58, 114.49, 110.88, 109.61, 106.13, 105.77. HRMS-ESI $m/z$ [M + H]$^+$ calcd for $C_{21}H_{14}F_4N_4O_3$: 447.1080, found: 447.1071.

**2-Chloro-4-(4,4,5,5-tetramethyl-1,3,2-dioxaborolan-2-yl)-aniline (B-25a).** Following the synthetic protocol for intermediate **B-11a**, a reaction of 4-bromo-2-chloroaniline (500 mg, 2.43 mmol) and bis(pinacolato)diboron (801 mg, 3.16 mmol) afforded the product as a yellow solid (470 mg, 76%). MS $m/z$ (ESI) [M + H]$^+$: 254.4.


https://doi.org/10.1021/acs.jmedchem.5c03775
J. Med. Chem. XXXX, XXX, XXX−XXX

**4-(4-Amino-3-chlorophenyl)benzo[*d*]isoxazol-3-amine (B-25b).** Following the synthetic protocol for intermediate **B-1a**, a reaction of **B-25a** (470 mg, 1.86 mmol) and 4-bromobenzo[*d*]isoxazol-3-amine (324 mg, 1.43 mmol) afforded the product as a yellow solid (290 mg, 78%). MS *m/z* (ESI) $[M + H]^+$: 260.2.

**1-(4-(3-Aminobenzo[*d*]isoxazol-4-yl)-2-chlorophenyl)-3-(3-(trifluoromethoxy)phenyl)urea (25).** Following the synthetic protocol for compound **4**, a reaction of 3-(trifluoromethoxy)aniline (248 mg, 1.40 mmol) and intermediate **B-25b** (290 mg, 1.12 mmol) afforded the product as a white solid (65 mg, 13%). mp: 190−192 °C; HPLC analysis, retention time, 4.658 min; peak area, 95.13%. $^1$H NMR (300 MHz, DMSO-$d_6$) $\delta$ 9.90 (s, 1H), 8.61 (s, 1H), 8.33 (d, $J$ = 8.6 Hz, 1H), 7.76 (s, 1H), 7.68−7.39 (m, 5H), 7.31 (m, 1H), 7.19 (m, 1H), 7.05−6.95 (m, 1H), 5.34 (s, 2H). HRMS-ESI *m/z* $[M + H]^+$ calcd for $C_{21}H_{14}ClF_3N_4O_3$: 463.0785, found: 463.0784.

**3-Chloro-4-(4,4,5,5-tetramethyl-1,3,2-dioxaborolan-2-yl)-aniline (B-26a).** Following the synthetic protocol for intermediate **B-11a**, a reaction of 4-bromo-3-chloroaniline (500 mg, 2.43 mmol) and bis(pinacolato)diboron (801 mg, 3.16 mmol) afforded the product as a yellow solid (470 mg, 76%). MS *m/z* (ESI) $[M + H]^+$: 254.2.

**4-(4-Amino-2-chlorophenyl)benzo[*d*]isoxazol-3-amine (B-26b).** Following the synthetic protocol for intermediate **B-1a**, a reaction of **B-26a** (470 mg, 1.86 mmol) and 4-bromobenzo[*d*]isoxazol-3-amine (324 mg, 1.43 mmol) afforded the product as a yellow solid (295 mg, 80%). $^1$H NMR (300 MHz, DMSO-$d_6$) $\delta$ 7.62−7.42 (m, 2H), 7.05 (m, 2H), 6.77 (d, $J$ = 2.0 Hz, 1H), 6.64 (d, $J$ = 8.3 Hz, 1H), 5.70 (s, 2H), 5.01 (s, 2H). MS *m/z* (ESI) $[M + H]^+$: 260.1.

**1-(4-(3-Aminobenzo[*d*]isoxazol-4-yl)-3-chlorophenyl)-3-(3-(trifluoromethoxy)phenyl)urea (26).** Following the synthetic protocol for compound **4**, a reaction of 3-(trifluoromethoxy)aniline (252 mg, 1.42 mmol) and intermediate **B-26b** (295 mg, 1.14 mmol) afforded the product as a white solid (69 mg, 13%). mp: 115−117 °C; HPLC analysis, retention time, 4.170 min; peak area, 97.18%. $^1$H NMR (400 MHz, DMSO-$d_6$) $\delta$ 9.23 (s, 1H), 9.21 (s, 1H), 7.90 (d, $J$ = 2.1 Hz, 1H), 7.72 (s, 1H), 7.61 (m, 1H), 7.54 (d, $J$ = 8.4 Hz, 1H), 7.42−7.45 (m, 1H), 7.42 (d, $J$ = 8.1 Hz, 1H), 7.36 (m, 2H), 7.10 (d, $J$ = 7.1 Hz, 1H), 7.01−6.96 (m, 1H), 5.04 (s, 2H). HRMS-ESI *m/z* $[M + H]^+$ calcd for $C_{21}H_{14}ClF_3N_4O_3$: 463.0785, found: 463.0789.

**2-Methoxy-4-(4,4,5,5-tetramethyl-1,3,2-dioxaborolan-2-yl)-aniline (B-27a).** Following the synthetic protocol for intermediate **B-11a**, a reaction of 2-methoxy-4-bromoaniline (500 mg, 2.48 mmol) and bis(pinacolato)diboron (817 mg, 3.22 mmol) afforded the product as a yellow solid (509 mg, 82%). MS *m/z* (ESI) $[M + H]^+$: 250.2.

**4-(4-Amino-3-methoxyphenyl)benzo[*d*]isoxazol-3-amine (B-27b).** Following the synthetic protocol for intermediate **B-1a**, a reaction of **B-27a** (509 mg, 2.04 mmol) and 4-bromobenzo[*d*]isoxazol-3-amine (357 mg, 1.57 mmol) afforded the product as a yellow solid (350 mg, 87%). MS *m/z* (ESI) $[M + H]^+$: 256.2.

**1-(4-(3-Aminobenzo[*d*]isoxazol-4-yl)-2-methoxyphenyl)-3-(3-(trifluoromethoxy)phenyl)urea (27).** Following the synthetic protocol for compound **4**, a reaction of 3-(trifluoromethoxy)aniline (304 mg, 1.72 mmol) and intermediate **B-27b** (350 mg, 1.37 mmol) afforded the product as a white solid (60 mg, 10%). mp: 185−187 °C; HPLC analysis, retention time, 3.880 min; peak area, 98.41%. $^1$H NMR (300 MHz, DMSO-$d_6$) $\delta$ 9.74 (s, 1H), 8.48 (s, 1H), 8.31 (d, $J$ = 8.4 Hz, 1H), 7.76 (s, 1H), 7.60 (t, $J$ = 7.8 Hz, 1H), 7.50 (d, $J$ = 8.3 Hz, 1H), 7.43 (t, $J$ = 8.2 Hz, 1H), 7.31−7.25 (m, 1H), 7.24−7.17 (m, 2H), 7.08 (m, 1H), 6.97 (d, $J$ = 8.3 Hz, 1H), 5.32 (s, 2H), 3.97 (s, 3H). HRMS-ESI *m/z* $[M + H]^+$ calcd for $C_{22}H_{18}F_3N_4O_4$: 459.1280, found: 459.1276.

**5-Amino-2-(4,4,5,5-tetramethyl-1,3,2-dioxaborolan-2-yl)-benzonitrile (B-28a).** Following the synthetic protocol for intermediate **B-11a**, a reaction of 5-amino-2-bromobenzonitrile (500 mg, 2.55 mmol) and bis(pinacolato)diboron (842 mg, 3.31 mmol) afforded the product as a yellow solid (469 mg, 75%). MS *m/z* (ESI) $[M + H]^+$: 245.2.

**5-Amino-2-(3-aminobenzo[*d*]isoxazol-4-yl)benzonitrile (B-28b).** Following the synthetic protocol for intermediate **B-1a**, a reaction of **B-28a** (469 mg, 1.92 mmol) and 4-bromobenzo[*d*]isoxazol-3-amine (336 mg, 1.48 mmol) afforded the product as a yellow solid (260 mg, 70%). $^1$H NMR (400 MHz, DMSO-$d_6$) $\delta$ 7.60 (t, $J$ = 7.8 Hz, 1H), 7.53 (d, $J$ = 8.4 Hz, 1H), 7.24 (d, $J$ = 8.4 Hz, 1H), 7.14 (d, $J$ = 7.0 Hz, 1H), 7.03 (d, $J$ = 2.3 Hz, 1H), 6.95 (m, 1H), 5.88 (s, 2H), 5.12 (s, 2H). MS *m/z* (ESI) $[M + H]^+$: 251.2.

**1-(4-(3-Aminobenzo[*d*]isoxazol-4-yl)-3-cyanophenyl)-3-(3-(trifluoromethoxy)phenyl)urea (28).** Following the synthetic protocol for compound **4**, a reaction of 3-(trifluoromethoxy)aniline (232 mg, 1.30 mmol) and intermediate **B-28b** (260 mg, 1.04 mmol) afforded the product as a white solid (65 mg, 14%). mp: 214−216 °C; HPLC analysis, retention time, 3.591 min; peak area, 98.95%. $^1$H NMR (400 MHz, DMSO-$d_6$) $\delta$ 9.29 (s, 1H), 9.27 (s, 1H), 8.14 (d, $J$ = 2.3 Hz, 1H), 7.80 (m, 1H), 7.72 (s, 1H), 7.68−7.59 (m, 2H), 7.54 (d, $J$ = 8.5 Hz, 1H), 7.44 (t, $J$ = 8.1 Hz, 1H), 7.36 (d, $J$ = 8.7 Hz, 1H), 7.23 (d, $J$ = 6.9 Hz, 1H), 7.00 (d, $J$ = 8.7 Hz, 1H), 5.22 (s, 2H). $^{13}$C NMR (151 MHz, DMSO-$d_6$) $\delta$ 163.07, 158.58, 152.83, 149.21, 141.57, 140.65, 133.76, 133.43, 131.79, 130.93, 130.50, 124.77, 123.11, 122.45, 120.59 (q, $^1J_{C-F}$ = 256.7 Hz), 118.33, 117.64, 114.62, 114.31, 112.55, 111.02, 110.34. HRMS-ESI *m/z* $[M + H]^+$ calcd for $C_{22}H_{14}F_3N_5O_3$: 454.1127, found: 454.1122.

**2,3-Dimethyl-4-(4,4,5,5-tetramethyl-1,3,2-dioxaborolan-2-yl)aniline (B-29a).** Following the synthetic protocol for intermediate **B-11a**, a reaction of 4-bromo-2,3-dimethylaniline (500 mg, 2.51 mmol) and bis(pinacolato)diboron (830 mg, 3.27 mmol) afforded the product as a yellow solid (513 mg, 83%). MS *m/z* (ESI) $[M + H]^+$: 248.2.

**4-(4-Amino-2,3-dimethylphenyl)benzo[*d*]isoxazol-3-amine (B-29b).** Following the synthetic protocol for intermediate **B-1a**, a reaction of **B-29a** (500 mg, 2.02 mmol) and 4-bromobenzo[*d*]isoxazol-3-amine (418 mg, 1.84 mmol) afforded the product as a yellow solid (300 mg, 64%). MS *m/z* (ESI) $[M + H]^+$: 254.1.

**1-(4-(3-Aminobenzo[*d*]isoxazol-4-yl)-2,3-dimethylphenyl)-3-(3-(trifluoromethoxy)phenyl)urea (29).** Following the synthetic protocol for compound **4**, a reaction of 3-(trifluoromethoxy)aniline (232 mg, 1.31 mmol) and intermediate **B-29b** (265 mg, 1.05 mmol) afforded the product as a white solid (43 mg, 9%). mp: 170−172 °C; HPLC analysis, retention time, 4.098 min; peak area, 97.66%. $^1$H NMR (400 MHz, DMSO-$d_6$) $\delta$ 9.44 (s, 1H), 8.27 (s, 1H), 7.75 (s, 1H), 7.71 (d, $J$ = 8.3 Hz, 1H), 7.60 (m, 1H), 7.51 (d, $J$ = 8.4 Hz, 1H), 7.42 (t, $J$ = 8.2 Hz, 1H), 7.35−7.27 (m, 1H), 7.07 (d, $J$ = 8.3 Hz, 1H), 7.02 (d, $J$ = 7.1 Hz, 1H), 6.99−6.93 (m, 1H), 4.93 (s, 2H), 2.25 (s, 3H), 2.02 (s, 3H). $^{13}$C NMR (151 MHz, DMSO-$d_6$) $\delta$ 162.56, 158.59, 153.34, 149.26, 142.28, 137.55, 135.18, 132.21, 130.87, 130.59, 128.96, 127.08, 123.96, 120.56, 117.05, 114.66, 113.96, 110.42, 108.92, 17.79, 14.78. HRMS-ESI *m/z* $[M + H]^+$ calcd for $C_{23}H_{19}F_3N_4O_3$: 457.1488, found: 457.1488.

**2,3-Difluoro-4-(4,4,5,5-tetramethyl-1,3,2-dioxaborolan-2-yl)aniline (B-30a).** Following the synthetic protocol for intermediate **B-11a**, a reaction of 4-bromo-2,3-difluoroaniline (500 mg, 2.42 mmol) and bis(pinacolato)diboron (797 mg, 3.140 mmol) afforded the product as a yellow solid (490 mg, 79%). mp 102−106 °C. $^1$H NMR (300 MHz, DMSO-$d_6$) $\delta$ 7.08 (m, 1H), 6.60−6.50 (m, 1H), 5.96 (s, 2H), 1.26 (s, 12H). MS *m/z* (ESI) $[M + H]^+$: 256.1.

**4-(4-Amino-2,3-difluorophenyl)benzo[*d*]isoxazol-3-amine (B-30b).** Following the synthetic protocol for intermediate **B-1a**, a reaction of **B-30a** (490 mg, 1.92 mmol) and 4-bromobenzo[*d*]isoxazol-3-amine (397 mg, 1.75 mmol) afforded the product as a yellow solid (313 mg, 68%). $^1$H NMR (300 MHz, DMSO-$d_6$) $\delta$ 7.60−7.48 (m, 2H), 7.12 (m, 1H), 6.92 (m, 1H), 6.68 (m, 1H), 5.79 (s, 2H), 5.24 (s, 2H). MS *m/z* (ESI) $[M + H]^+$: 262.1.

**1-(4-(3-Aminobenzo[*d*]isoxazol-4-yl)-2,3-difluorophenyl)-3-(3-(trifluoromethoxy)phenyl)urea (30).** Following the synthetic protocol for compound **4**, a reaction of 3-(trifluoromethoxy)aniline (263 mg, 1.48 mmol) and intermediate **B-30b** (310 mg, 1.19 mmol) afforded the product as a white solid (47 mg, 9%). mp: 227−229 °C; HPLC analysis, retention time, 4.253 min; peak area, 98.79%. $^1$H NMR (300 MHz, DMSO-$d_6$) $\delta$ 9.47 (s, 1H), 8.99 (s, 1H), 8.10 (t, $J$ = 7.8 Hz, 1H), 7.75 (s, 1H), 7.65−7.55 (m, 2H), 7.45 (t, $J$ = 8.2 Hz, 1H), 7.35−7.28 (m, 1H), 7.21 (m, 2H), 7.01 (d, $J$ = 8.4 Hz, 1H), 5.35 (s, 2H). $^{13}$C NMR (75 MHz, DMSO-$d_6$) $\delta$ 163.09, 158.67, 152.35, 149.25 (d, $^3J_{C-F}$ = 2.25 Hz), 141.41, 131.05, 130.84, 130.46, 129.96 (dd, $^2J_{C-F}$ = 8.25 Hz, $^3J_{C-F}$ = 2.25 Hz), 129.44 (d, $^3J_{C-F}$ = 2.25 Hz), 126.14, 125.00, 120.58 (q, $^1J_{C-F}$ = 254,25 Hz), 119.44 (d, $^2J_{C-F}$ = 12.75 Hz), 117.33, 115.67 (d, $^3J_{C-F}$ = 2.25 Hz), 114.68, 114.58, 110.68, 110.08. HRMS-


https://doi.org/10.1021/acs.jmedchem.5c03775
J. Med. Chem. XXXX, XXX, XXX−XXX

ESI $m/z$ $[M + H]^+$ calcd for $C_{21}H_{13}F_5N_4O_3$: 465.0986, found: 465.0994.

**2,6-Difluoro-4-(4,4,5,5-tetramethyl-1,3,2-dioxaborolan-2-yl)aniline (B-31a).** Following the synthetic protocol for intermediate **B-11a**, a reaction of 4-bromo-2,6-difluoroaniline (500 mg, 2.42 mmol) and bis(pinacolato)diboron (797 mg, 3.14 mmol) afforded the product as a yellow solid (497 mg, 81%). mp 63−65 °C. $^1$H NMR (300 MHz, DMSO-$d_6$) $\delta$ 7.06 (m, 2H), 5.71 (s, 2H), 1.26 (s, 12H). MS $m/z$ (ESI) $[M + H]^+$: 256.3.

**4-(4-Amino-3,5-difluorophenyl)benzo[*d*]isoxazol-3-amine (B-31b).** Following the synthetic protocol for intermediate **B-1a**, a reaction of **B-31a** (497 mg, 1.95 mmol) and 4-bromobenzo[*d*]isoxazol-3-amine (340 mg, 1.50 mmol) afforded the product as a yellow solid (311 mg, 79%). MS $m/z$ (ESI) $[M + H]^+$: 262.2.

**1-(4-(3-Aminobenzo[*d*]isoxazol-4-yl)-2,6-difluorophenyl)-3-(3-(trifluoromethoxy)phenyl)urea (31).** Following the synthetic protocol for compound **4**, a reaction of 3-(trifluoromethoxy)aniline (263 mg, 1.48 mmol) and intermediate **B-31b** (311 mg, 1.19 mmol) afforded the product as a white solid (46 mg, 8%). mp: 196 -198 °C; HPLC analysis, retention time, 3.745 min; peak area, 98.56%. $^1$H NMR (300 MHz, DMSO-$d_6$) $\delta$ 9.31 (s, 1H), 8.43 (s, 1H) 7.72−7.57 (m, 3H), 7.45−7.32 (m, 4H), 7.24 (m, 1H), 6.97 (d, $J$ = 7.7 Hz, 1H), 5.43 (s, 2H). $^{13}$C NMR (151 MHz, DMSO-$d_6$) $\delta$ 163.39, 158.50, 157.98 (dd, $^1J_{C-F}$ = 249.15 Hz, $^3J_{C-F}$ = 6.04 Hz), 152.85, 149.21, 141.89, 136.43 (t, $^2J_{C-F}$ = 9.7 Hz), 135.22, 130.74 (d, $^2J_{C-F}$ = 37.75 Hz), 124.27, 120.58 (q, $^1J_{C-F}$ = 255.19 Hz), 117.33, 115.42 (t, $^2J_{C-F}$ = 16.61 Hz), 114.38, 113.37, 113.06 (dd, $^2J_{C-F}$ = 21.14 Hz, $^3J_{C-F}$ = 4.53 Hz), 110.72, 110.02. HRMS-ESI $m/z$ $[M + H]^+$ calcd for $C_{21}H_{13}F_5N_4O_3$: 465.0986, found: 465.0986.

**3,5-Difluoro-4-(4,4,5,5-tetramethyl-1,3,2-dioxaborolan-2-yl)aniline (B-32a).** Following the synthetic protocol for intermediate **B-11a**, a reaction of 4-bromo-3,5-difluoroaniline (500 mg, 2.42 mmol) and bis(pinacolato)diboron (797 mg, 3.14 mmol) afforded the product as a yellow solid (501 mg, 81%). MS $m/z$ (ESI) $[M + H]^+$: 256.1.

**4-(4-Amino-2,6-difluorophenyl)benzo[*d*]isoxazol-3-amine (B-32b).** Following the synthetic protocol for intermediate **B-1a**, a reaction of **B-32a** (501 mg, 1.96 mmol) and 4-bromobenzo[*d*]isoxazol-3-amine (340 mg, 1.51 mmol) afforded the product as a yellow solid (211 mg, 54%). $^1$H NMR (300 MHz, DMSO-$d_6$) $\delta$ 7.60−7.42 (m, 2H), 7.12−7.02 (m, 2H), 6.57−6.42 (m, 2H), 5.74 (s, 2H), 5.15 (s, 2H). MS $m/z$ (ESI) $[M + H]^+$: 262.2.

**1-(4-(3-Aminobenzo[*d*]isoxazol-4-yl)-3,5-difluorophenyl)-3-(3-(trifluoromethoxy)phenyl)urea (32).** Following the synthetic protocol for compound **4**, a reaction of 3-(trifluoromethoxy)aniline (179 mg, 1.01 mmol) and intermediate **B-32b** (211 mg, 0.808 mmol) afforded the product as a white solid (50 mg, 13%). mp: 98−100 °C. $^1$H NMR (300 MHz, DMSO-$d_6$) $\delta$ 9.39 (s, 1H), 9.32 (s, 1H), 7.70 (s, 1H), 7.67−7.62 (m, 1H), 7.61−7.59 (m, 1H), 7.45 (d, $J$ = 8.1 Hz, 1H), 7.41 (s, 1H), 7.40 (s, 1H), 7.37 (d, $J$ = 2.3 Hz, 1H), 7.18 (m, 1H), 7.03−6.97 (m, 1H), 5.30 (s, 2H). HRMS-ESI $m/z$ $[M + H]^+$ calcd for $C_{21}H_{13}F_5N_4O_3$: 465.0986, found: 465.0986.

**2,5-Difluoro-4-(4,4,5,5-tetramethyl-1,3,2-dioxaborolan-2-yl)aniline (B-33a).** Following the synthetic protocol for intermediate **B-11a**, a reaction of 4-bromo-2,5-difluoroaniline (500 mg, 2.42 mmol) and bis(pinacolato)diboron (797 mg, 3.14 mmol) afforded the product as a yellow solid (521 mg, 84%). MS $m/z$ (ESI) $[M + H]^+$: 234.3.

**4-(4-Amino-2,5-difluorophenyl)benzo[*d*]isoxazol-3-amine (B-33b).** Following the synthetic protocol for intermediate **B-1a**, a reaction of **B-33a** (521 mg, 2.04 mmol) and 4-bromobenzo[*d*]isoxazol-3-amine (357 mg, 1.57 mmol) afforded the product as a yellow solid (304 mg, 74%). $^1$H NMR (300 MHz, DMSO-$d_6$) $\delta$ 7.63−7.42 (m, 2H), 7.14−7.06 (m, 2H), 6.67 (m, 1H), 5.76 (s, 2H), 5.24 (s, 2H). MS $m/z$ (ESI) $[M + H]^+$: 262.4.

**1-(4-(3-Aminobenzo[*d*]isoxazol-4-yl)-2,5-difluorophenyl)-3-(3-(trifluoromethoxy)phenyl)urea (33).** Following the synthetic protocol for compound **4**, a reaction of 3-(trifluoromethoxy)aniline (258 mg, 1.46 mmol) and intermediate **B-33b** (304 mg, 1.16 mmol) afforded the product as a white solid (53 mg, 10%). mp: 198−200 °C; HPLC analysis, retention time, 4.121 min; peak area, 97.20%. $^1$H NMR (300 MHz, DMSO-$d_6$) $\delta$ 9.52 (s, 1H), 9.01 (s, 1H), 8.19 (m, 1H), 7.74 (s, 1H), 7.64−7.54 (m, 2H), 7.49−7.39 (m, 2H), 7.33−7.28 (m, 1H), 7.18 (d, $J$ = 6.8 Hz, 1H), 7.02 (d, $J$ = 8.2 Hz, 1H), 5.34 (s, 2H). $^{13}$C NMR (75 MHz, DMSO-$d_6$) $\delta$ 163.04, 158.69, 155.20 (d, $^1J_{C-F}$ = 177.75 Hz), 152.32, 149.25, 148.14 (d, $^1J_{C-F}$ = 178.5 Hz), 141.26, 131.05, 130.38, 129.57, 129.39 (t, $^3J_{C-F}$ = 9.0 Hz), 124.96, 120.57 (q, $^1J_{C-F}$ = 190.5 Hz), 117.56 (dd, $^2J_{C-F}$ = 17.25 Hz, $^3J_{C-F}$ = 3.0 Hz), 117.36, 114.76, 114.61, 110.72, 109.97, 107.47 (dd, $^2J_{C-F}$ = 22.5 Hz, $^3J_{C-F}$ = 2.5 Hz). HRMS-ESI $m/z$ $[M + H]^+$ calcd for $C_{21}H_{13}F_5N_4O_3$: 465.0986, found: 465.0989.

**3-Chloro-2-fluoro-4-(4,4,5,5-tetramethyl-1,3,2-dioxaborolan-2-yl)aniline (B-34a).** Following the synthetic protocol for intermediate **B-11a**, a reaction of 4-bromo-3-chloro-2-fluoroaniline (500 mg, 2.23 mmol) and bis(pinacolato)diboron (737 mg, 2.90 mmol) afforded the product as a yellow solid (534 mg, 87%). mp 76−80 °C. $^1$H NMR (300 MHz, DMSO-$d_6$) $\delta$ 7.20 (d, $J$ = 8.2 Hz, 1H), 6.59 (d, $J$ = 10.7 Hz, 1H), 5.90 (s, 2H), 1.26 (s, 12H). MS $m/z$ (ESI) $[M + H]^+$: 272.2.

**4-(4-Amino-2-chloro-3-fluorophenyl)benzo[*d*]isoxazol-3-amine (B-34b).** Following the synthetic protocol for intermediate **B-1a**, a reaction of **B-34a** (524 mg, 1.93 mmol) and 4-bromobenzo[*d*]-isoxazol-3-amine (399 mg, 1.76 mmol) afforded the product as a yellow solid (300 mg, 62%). $^1$H NMR (300 MHz, DMSO-$d_6$) $\delta$ 7.69−7.47 (m, 3H), 7.06 (m, 1H), 6.96 (m, 1H), 6.83 (t, $J$ = 8.5 Hz, 1H), 5.74 (s, 2H), 5.08 (s, 2H). MS $m/z$ (ESI) $[M + H]^+$: 277.4.

**1-(4-(3-Aminobenzo[*d*]isoxazol-4-yl)-3-chloro-2-fluorophenyl)-3-(3-(trifluoromethoxy)phenyl)urea (34).** Following the synthetic protocol for compound **4**, a reaction of 3-(trifluoromethoxy)-aniline (240 mg, 1.35 mmol) and intermediate **B-34b** (300 mg, 1.08 mmol) afforded the product as a white solid (56 mg, 11%). mp: 129−130 °C. $^1$H NMR (300 MHz, DMSO-$d_6$) $\delta$ 9.54 (s, 1H), 8.98 (d, $J$ = 2.7 Hz, 1H), 8.35−8.22 (m, 1H), 7.77 (m, 1H), 7.67−7.56 (m, 2H), 7.46 (t, $J$ = 8.2 Hz, 1H), 7.34−7.24 (m, 2H), 7.13 (m, 1H), 7.07−6.98 (m, 1H), 5.24 (s, 2H). HRMS-ESI $m/z$ $[M + H]^+$ calcd for $C_{21}H_{13}ClF_4N_4O_3$: 481.0691, found: 481.0686.

**2,3-Dichloro-4-(4,4,5,5-tetramethyl-1,3,2-dioxaborolan-2-yl)aniline (B-35a).** Following the synthetic protocol for intermediate **B-11a**, a reaction of 4-bromo-2,3-dichloroaniline (500 mg, 2.09 mmol) and bis(pinacolato)diboron (691 mg, 2.72 mmol) afforded the product as a yellow solid (495 mg, 83%). MS $m/z$ (ESI) $[M + H]^+$: 288.2.

**4-(4-Amino-2,3-dichlorophenyl)benzo[*d*]isoxazol-3-amine (B-35b).** Following the synthetic protocol for intermediate **B-1a**, a reaction of **B-35a** (495 mg, 1.72 mmol) and 4-bromobenzo[*d*]isoxazol-3-amine (301 mg, 1.33 mmol) afforded the product as a yellow solid (305 mg, 78%). $^1$H NMR (300 MHz, DMSO-$d_6$) $\delta$ 7.63−7.46 (m, 2H), 7.15−7.02 (m, 2H), 6.87 (d, $J$ = 8.4 Hz, 1H), 5.96 (s, 2H), 5.05 (s, 2H). MS $m/z$ (ESI) $[M + H]^+$: 293.4.

**1-(4-(3-Aminobenzo[*d*]isoxazol-4-yl)-2,3-dichlorophenyl)-3-(3-(trifluoromethoxy)phenyl)urea (35).** Following the synthetic protocol for compound **4**, a reaction of 3-(trifluoromethoxy)aniline (263 mg, 1.28 mmol) and intermediate **B-35b** (301 mg, 1.03 mmol) afforded the product as a white solid (60 mg, 12%). mp: 110−112 °C; HPLC analysis, retention time, 4.745 min; peak area, 96.06%. $^1$H NMR (300 MHz, DMSO-$d_6$) $\delta$ 11.28 (s, 1H), 10.03 (s, 1H), 9.65 (d, $J$ = 8.6 Hz, 1H), 9.09 (s, 1H), 9.00−8.94 (m, 1H), 8.91 (d, $J$ = 8.2 Hz, 1H), 8.80 (t, $J$ = 8.1 Hz, 1H), 8.74 (d, $J$ = 8.7 Hz, 1H), 8.67 (d, $J$ = 8.4 Hz, 1H), 8.46 (d, $J$ = 6.8 Hz, 1H), 8.35 (d, $J$ = 8.2 Hz, 1H), 6.50 (s, 2H). HRMS-ESI $m/z$ $[M + H]^+$ calcd for $C_{21}H_{13}Cl_2F_3N_4O_3$: 497.0395, found: 497.0399.

**3-Fluoro-2-methyl-4-(4,4,5,5-tetramethyl-1,3,2-dioxaborolan-2-yl)aniline (B-36a).** Following the synthetic protocol for intermediate **B-11a**, a reaction of 4-bromo-3-fluoro-2-methylaniline (500 mg, 2.45 mmol) and bis(pinacolato)diboron (809 mg, 3.19 mmol) afforded the product as a yellow solid (500 mg, 81%). MS $m/z$ (ESI) $[M + H]^+$: 252.3.

**4-(4-Amino-2-fluoro-3-methylphenyl)benzo[*d*]isoxazol-3-amine (B-36b).** Following the synthetic protocol for intermediate **B-1b**, a reaction of **B-36a** (500 mg, 1.99 mmol) and 4-bromobenzo[*d*]-isoxazol-3-amine (348 mg, 1.53 mmol) afforded the product as a yellow solid (269 mg, 68%). MS $m/z$ (ESI) $[M + H]^+$: 257.1.

**1-(4-(3-Aminobenzo[*d*]isoxazol-4-yl)-3-fluoro-2-methylphenyl)-3-(3-(trifluoromethoxy)phenyl)urea (36).** Following the synthetic protocol for compound **4**, a reaction of 3-(trifluoromethoxy)-


https://doi.org/10.1021/acs.jmedchem.5c03775
J. Med. Chem. XXXX, XXX, XXX−XXX

aniline (232 mg, 1.31 mmol) and intermediate **B-36b** (269 mg, 1.05 mmol) afforded the product as a white solid (69 mg, 14%). mp: 185−187 °C. $^1$H NMR (300 MHz, DMSO-$d_6$) $\delta$ 9.59 (d, $J$ = 2.0 Hz, 1H), 8.42 (s, 1H), 7.90 (d, $J$ = 8.2 Hz, 1H), 7.75 (s, 1H), 7.68−7.53 (m, 2H), 7.49−7.40 (m, 1H), 7.28 (m, 2H), 7.16 (d, $J$ = 6.9 Hz, 1H), 6.98 (d, $J$ = 8.0 Hz, 1H), 5.17 (s, 2H), 2.25 (s, 3H). $^{13}$C NMR (75 MHz, DMSO-$d_6$) $\delta$ 162.95, 158.63, 157.48 (d, $^1J_{C-F}$ = 237.0 Hz), 152.83, 149.25, 141.81, 139.83 (d, $^3J_{C-F}$ = 6.0 Hz), 131.06, 130.98, 130.42, 128.54 (d, $^3J_{C-F}$ = 6.0 Hz), 124.79, 120.59 (q, $^1J_{C-F}$ = 253.5 Hz), 118.80 (d, $^2J_{C-F}$ = 17.25 Hz), 117.22, 117.08 (d, $^3J_{C-F}$ = 3.75 Hz), 115.88 (d, $^2J_{C-F}$ = 18.75 Hz), 114.55, 114.37, 110.61, 109.59. HRMS-ESI $m/z$ [M + H]$^+$ calcd for $C_{22}H_{16}F_4N_4O_3$: 461.1237, found: 461.1226.

**5-Fluoro-2-methyl-4-(4,4,5,5-tetramethyl-1,3,2-dioxaborolan-2-yl)aniline (B-37a).** Following the synthetic protocol for intermediate **B-11a**, a reaction of 4-bromo-2-fluoro-5-methylaniline (500 mg, 2.45 mmol) and bis(pinacolato)diboron (809 mg, 3.19 mmol) afforded the product as a yellow solid (504 mg, 82%). MS $m/z$ (ESI) [M + H]$^+$: 252.2

**4-(4-Amino-2-fluoro-5-methylphenyl)benzo[*d*]isoxazol-3-amine (B-37b).** Following the synthetic protocol for intermediate **B-1a**, a reaction of **B-37a** (504 mg, 2.00 mmol) and 4-bromobenzo[*d*]-isoxazol-3-amine (348 mg, 1.54 mmol) afforded the product as a yellow solid (283 mg, 72%). MS $m/z$ (ESI) [M + H]$^+$: 257.1.

**1-(4-(3-Aminobenzo[*d*]isoxazol-4-yl)-5-fluoro-2-methylphenyl)-3-(3-(trifluoromethoxy)phenyl)urea (37).** Following the synthetic protocol for compound **4**, a reaction of 3-(trifluoromethoxy)-aniline (241 mg, 1.36 mmol) and intermediate **B-37b** (283 mg, 1.09 mmol) afforded the product as a white solid (30 mg, 6%). mp: 155−157 °C; HPLC analysis, retention time, 7.862 min; peak area, 99.33%. $^1$H NMR (300 MHz, DMSO-$d_6$) $\delta$ 9.41 (s, 1H), 8.68 (s, 1H), 8.11 (d, $J$ = 8.2 Hz, 1H), 7.70 (s, 1H), 7.53 (d, $J$ = 7.7 Hz, 1H), 7.47 (s, 1H), 7.36 (d, $J$ = 8.2 Hz, 1H), 7.25−7.09 (m, 2H), 7.04−6.87 (m, 2H), 4.98 (s, 2H), 1.97 (s, 3H). $^{13}$C NMR (75 MHz, DMSO-$d_6$) $\delta$ 162.95, 157.52 (d, $^1J_{C-F}$ = 238.5 Hz), 158.66, 152.72, 149.26 (d, $^3J_{C-F}$ = 2.25 Hz), 141.65, 139.54 (d, $^2J_{C-F}$ = 11.25 Hz), 132.76 (d, $^3J_{C-F}$ = 3.75 Hz), 131.03, 130.73, 130.44, 124.80, 123.09 (d, $^3J_{C-F}$ = 3.75 Hz), 120.59 (q, $^1J_{C-F}$ = 255.0 Hz), 117.92 (d, $^2J_{C-F}$ = 15.75 Hz), 117.26, 114.56, 114.50, 110.66, 109.59, 107.41, 107.04. HRMS-ESI $m/z$ [M + H]$^+$ calcd for $C_{22}H_{16}F_4N_4O_3$: 461.1237, found: 461.1223.

**2-Fluoro-5-methyl-4-(4,4,5,5-tetramethyl-1,3,2-dioxaborolan-2-yl)aniline (B-38a).** Following the synthetic protocol for intermediate **B-11a**, a reaction of 2-methyl-4-bromo-5-fluoroaniline (500 mg, 2.45 mmol) and bis(pinacolato)diboron (809 mg, 3.19 mmol) afforded the product as a yellow solid (501 mg, 81%). MS $m/z$ (ESI) [M + H]$^+$: 252.2.

**4-(4-Amino-5-fluoro-2-methylphenyl)benzo[*d*]isoxazol-3-amine (B-38b).** Following the synthetic protocol for intermediate **B-1a**, a reaction of **B-38a** (501 mg, 2.00 mmol) and 4-bromobenzo[*d*]-isoxazol-3-amine (348 mg, 1.54 mmol) afforded the product as a yellow solid (280 mg, 71%). MS $m/z$ (ESI) [M + H]$^+$: 257.1.

**1-(4-(3-Aminobenzo[*d*]isoxazol-4-yl)-2-fluoro-5-methylphenyl)-3-(3-(trifluoromethoxy)phenyl)urea (38).** Following the synthetic protocol for compound **4**, a reaction of 3-(trifluoromethoxy)-aniline (241 mg, 1.36 mmol) and intermediate **B-38b** (280 mg, 1.09 mmol) afforded the product as a white solid (40 mg, 8%). mp: 107−109 °C; HPLC analysis, retention time, 3.888 min; peak area, 99.51%. $^1$H NMR (300 MHz, DMSO-$d_6$) $\delta$ 9.56 (s, 1H), 8.28 (s, 1H), 8.05 (d, $J$ = 12.8 Hz, 1H), 7.75 (m, 1H), 7.65−7.51 (m, 2H), 7.45 (t, $J$ = 8.2 Hz, 1H), 7.34−7.27 (m, 2H), 7.15 (m, 1H), 7.00 (m, 1H), 5.19 (s, 2H), 2.30 (s, 3H). HRMS-ESI $m/z$ [M + H]$^+$ calcd for $C_{22}H_{16}F_4N_4O_3$: 461.1231, found: 461.1227.

***tert*-Butyl (4-(2-cyano-3-fluorophenoxy)phenyl)carbamate (B-13a).** A solution of 2,6-difluorobenzonitrile (500 mg, 3.60 mmol) and *tert*-butyl (4-hydroxyphenyl)carbamate (750 mg, 3.60 mmol) in anhydrous DMF (12 mL) was treated with potassium hydroxide (605 mg, 10.8 mmol). The reaction mixture was stirred at 25 °C for 10 h. Upon completion, the mixture was diluted with $H_2O$ (100 mL) and extracted with ethyl acetate (6 × 50 mL). The combined organic layers were washed with brine (2 × 50 mL), dried over anhydrous $Na_2SO_4$, and concentrated *in vacuo*. Purification by column chromatography on silica gel (eluent: petroleum ether/ethyl acetate, 10:1 v/v) afforded the product as a white solid (520 mg, 44%). mp: 116−120 °C. $^1$H NMR (300 MHz, chloroform-$d$) $\delta$ 7.49−7.36 (m, 3H), 7.12−7.04 (m, 2H), 6.87 (m, 1H), 6.57 (m, 2H), 1.55 (s, 9H). MS $m/z$ (ESI) [M + H]$^+$: 329.2.

***tert*-Butyl (4-((3-aminobenzo[*d*]isoxazol-4-yl)oxy)phenyl)-carbamate (B-13b).** A solution of acetomenadione (228 mg, 1.32 mmol) in anhydrous DMF (20 mL) was treated with potassium *tert*-butoxide (371 mg, 3.31 mmol). After stirring at 25 °C for 1 h, intermediate **B-13a** (500 mg, 1.52 mmol) was added. The reaction mixture was stirred for an additional 12 h at 25 °C. Upon completion (TLC monitoring), the mixture was diluted with $H_2O$ (50 mL) and extracted with ethyl acetate (5 × 50 mL). The combined organic layers were washed with brine (2 × 50 mL), dried over anhydrous $Na_2SO_4$, and concentrated in vacuo. Purification by column chromatography on silica gel (eluent: petroleum ether/ethyl acetate, 20:1 v/v) afforded the product as a white oil (300 mg, 58%). $^1$H NMR (400 MHz, DMSO-$d_6$) $\delta$ 9.45 (s, 1H), 7.54 (d, $J$ = 8.8 Hz, 2H), 7.37 (t, $J$ = 8.2 Hz, 1H), 7.19−7.12 (m, 2H), 7.09 (d, $J$ = 8.6 Hz, 1H), 6.31 (d, $J$ = 7.9 Hz, 1H), 6.04 (s, 2H), 1.49 (s, 9H). MS $m/z$ (ESI) [M + H]$^+$: 342.2.

**4-(4-Aminophenoxy)benzo[*d*]isoxazol-3-amine (B-13c).** A solution of intermediate **B-13b** (300 mg, 0.880 mmol) in dichloromethane (10 mL) was treated with trifluoroacetic acid (2 mL). The reaction mixture was stirred at 25 °C for 1 h. After complete deprotection (confirmed by TLC), the solution was concentrated under reduced pressure. The residue was diluted with $H_2O$ (20 mL), adjusted to pH 8 with saturated $NaHCO_3$(aq), and extracted with ethyl acetate (5 × 20 mL). The combined organic layers were washed with brine (2 × 20 mL), dried over anhydrous $Na_2SO_4$, and concentrated in vacuo to afford the product as a white solid (200 mg, 94%). mp: 82−85 °C. 1H NMR (300 MHz, DMSO-d6) $\delta$: 7.33 (t, J = 8.2 Hz, 1H), 7.02 (d, J = 8.1 Hz, 1H), 6.90 (d, J = 8.6 Hz, 2H), 6.63 (d, J = 8.7 Hz, 2H), 6.25 (d, J = 7.9 Hz, 1H), 6.00 (s, 2H), 5.10 (s, 2H). MS $m/z$ (ESI) [M + H]+: 242.1.

**1-(4-((3-Aminobenzo[*d*]isoxazol-4-yl)oxy)phenyl)-3-(3-(trifluoromethoxy)phenyl)urea (13).** Following the synthetic protocol for compound **4**, a reaction of intermediate **B-13c** (200 mg, 0.830 mmol) and 3-(trifluoromethoxy)aniline (176 mg, 0.996 mmol) afforded the product as a white solid (50 mg, 14%). mp: 193−195 °C; HPLC analysis, retention time, 10.391 min; peak area, 97.47%. $^1$H NMR (300 MHz, DMSO-$d_6$) $\delta$ 9.05 (s, 1H), 8.90 (s, 1H), 7.72 (s, 1H), 7.60−7.53 (m, 2H), 7.44−7.29 (m, 3H), 7.22−7.16 (m, 2H), 7.11 (d, $J$ = 8.3 Hz, 1H), 6.99−6.93 (m, 1H), 6.35 (d, $J$ = 8.0 Hz, 1H), 6.08 (s, 2H). $^{13}$C NMR (151 MHz, DMSO-$d_6$) $\delta$ 164.64, 158.17, 154.12, 152.96, 149.56, 149.23, 141.99, 136.96, 132.03, 130.86, 121.64, 120.56, 117.32, 114.15, 110.68, 107.54, 107.28, 103.97. HRMS-ESI $m/z$ [M + H]$^+$ calcd for $C_{22}H_{16}F_4N_4O_3$: 467.0938, found: 467.0933.

***tert*-Butyl (3-(2-cyano-3-fluorophenoxy)phenyl)carbamate (B-15a).** Following the synthetic protocol for intermediate **B-13a**, a reaction of 2,6-difluorobenzonitrile (500 mg, 3.60 mmol) and *tert*-butyl (4-hydroxyphenyl)carbamate (750 mg, 3.60 mmol) afforded the product as a white solid (502 mg, 43%). MS $m/z$ (ESI) [M + H]$^+$: 329.2.

***tert*-Butyl (3-((3-aminobenzo[*d*]isoxazol-4-yl)oxy)phenyl)-carbamate (B-15b).** Following the synthetic protocol for intermediate **B-13b**, the reaction of intermediate **B-15a** (500 mg, 1.52 mmol) afforded the product as a white oil (304 mg, 59%). MS $m/z$ (ESI) [M + H]$^+$: 342.2.

**4-(3-Aminophenoxy)benzo[*d*]isoxazol-3-amine (B-15c).** Following the synthetic protocol for target intermediate **B-13c**, the reaction of intermediate **B-13b** (300 mg, 0.880 mmol) afforded the product as a yellow solid (202 mg, 95%). $^1$H NMR (300 MHz, chloroform-$d$) $\delta$: 7.31 (t, $J$ = 8.0 Hz, 1H), 7.17 (t, $J$ = 7.7 Hz, 1H), 7.06 (d, $J$ = 8.1 Hz, 1H), 6.64−6.33 (m, 4H), 4.73 (s, 2H), 3.80 (s, 2H). MS $m/z$ (ESI) [M + H]$^+$: 242.1.

**1-(3-((3-Aminobenzo[*d*]isoxazol-4-yl)oxy)phenyl)-3-(3-(trifluoromethoxy)phenyl)urea (15).** Following the synthetic protocol for compound **4**, a reaction of intermediate **B-15c** (200 mg, 0.830 mmol) and 3-(trifluoromethoxy)aniline (176 mg, 0.996 mmol) afforded the product as a white solid (54 mg, 15%). mp: 218−220 °C;


https://doi.org/10.1021/acs.jmedchem.5c03775
J. Med. Chem. XXXX, XXX, XXX−XXX

HPLC analysis, retention time, 3.873 min; peak area, 99.44%. $^1$H NMR (400 MHz, DMSO-$d_6$) $\delta$ 9.03 (s, 1H), 8.97 (s, 1H), 7.66 (m, 1H), 7.47−7.36 (m, 4H), 7.27 (m, 2H), 7.16 (d, $J$ = 8.3 Hz, 1H), 6.95 (m, 1H), 6.84 (m, 1H), 6.48 (d, $J$ = 7.9 Hz, 1H), 6.04 (s, 2H). $^{13}$C NMR (75 MHz, DMSO-$d_6$) $\delta$ 164.62, 158.09, 155.65, 153.13, 152.75, 149.15, 141.75, 141.60, 132.05, 130.83, 130.72, 120.54 (q, $^1J_{C-F}$ = 254.25 Hz), 117.39, 115.17, 114.31, 114.17, 110.77, 110.46, 108.34, 107.93, 104.46. HRMS-ESI $m/z$ [M + H]$^+$ calcd for $C_{22}H_{15}F_4N_4O_3$: 467.0938, found: 467.0934.

**2-(4-(3-Aminobenzo[*d*]isoxazol-4-yl)phenyl)acetic acid (B-16a).** Following the synthetic protocol for intermediate **B-1a**, a reaction of 2-[4-(4,4,5,5-tetramethyl-1,3,2-dioxaborolan-2-yl)phenyl]-acetic acid (500 mg, 1.52 mmol) and 4-bromobenzo[*d*]isoxazol-3-amine (324 mg, 1.52 mmol) afforded the product as a yellow solid (394 mg, 87%). mp: 225−229 °C. $^1$H NMR (300 MHz, DMSO-$d_6$) $\delta$ 13.34 (s, 1H), 8.40−8.28 (m, 2H), 7.91−7.80 (m, 4H), 7.46 (m, 1H), 5.51 (s, 2H). MS $m/z$ (ESI) [M + H]$^+$: 255.1.

**2-(4-(3-Aminobenzo[*d*]isoxazol-4-yl)phenyl)-N-(3-(trifluoromethoxy)phenyl)acetamide (16).** A solution of intermediate **B-16a** (112 mg, 0.416 mmol), 2-(7-Azabenzotriazol-1-yl)-N,N,N′,N′-tetramethyluronium hexafluorophosphate (174 mg, 0.458 mmol), and *N*,*N*-diisopropylethylamine (162 mg, 1.25 mmol) in anhydrous DMF (5 mL) was stirred at 25 °C for 10 min. 3-(Trifluoromethoxy)aniline (73.7 mg, 0.416 mmol) was added, and stirring continued for 12 h at 25 °C. After complete consumption of starting material (TLC monitoring), the mixture was diluted with $H_2O$ (30 mL) and extracted with ethyl acetate (3 × 10 mL). The combined organic layers were washed with brine (2 × 10 mL), dried over anhydrous $Na_2SO_4$, and concentrated in vacuo. Purification by column chromatography on silica gel (eluent: petroleum ether/ethyl acetate, 2:1 v/v) afforded the product as a white solid (43 mg, 24%). mp: 78−80 °C. $^1$H NMR (400 MHz, DMSO-$d_6$) $\delta$ 10.53 (s, 1H), 7.83 (s, 1H), 7.63−7.58 (m, 2H), 7.53 (d, $J$ = 5.3 Hz, 2H), 7.50 (d, $J$ = 2.0 Hz, 3H), 7.44 (d, $J$ = 8.2 Hz, 1H), 7.16 (d, $J$ = 7.2 Hz, 1H), 7.05 (d, $J$ = 7.9 Hz, 1H), 5.19 (s, 2H), 3.78 (s, 2H). HRMS-ESI $m/z$ [M + H]$^+$ calcd for $C_{22}H_{16}F_4N_4O_3$: 428,1216, found: 428,1206.

**7-Bromo-2,3-dihydro-1*H*-inden-4-amine (B-19a).** A solution of 2,3-dihydro-1*H*-inden-4-amine (1.0 g, 10.5 mmol) and *N*-bromosuccinimide (1.87 g, 10.5 mmol) in dichloromethane (15 mL) was stirred at 25 °C for 16 h. After complete consumption of starting material (TLC monitoring), the mixture was concentrated *in vacuo*. Purification by column chromatography on silica gel (eluent: petroleum ether/ethyl acetate, 10:1 v/v) afforded the product as a white solid (0.6 g, 27%). mp: 64−66 °C. $^1$H NMR (300 MHz, DMSO-$d_6$) $\delta$ 6.97 (d, $J$ = 8.4 Hz, 1H), 6.35 (d, $J$ = 8.4 Hz, 1H), 5.01 (s, 2H), 2.75 (dt, $J$ = 12.6, 7.5 Hz, 4H), 1.99 (m, 2H). MS $m/z$ (ESI) [M + H]$^+$: 213.1.

**7-(4,4,5,5-Tetramethyl-1,3,2-dioxaborolan-2-yl)-2,3-dihydro-1*H*-inden-4-amine (B-19b).** Following the synthetic protocol for intermediate **B-11a**, a reaction of **B-19a** (600 mg, 2.83 mmol) and bis(pinacolato)diboron (863 mg, 3.40 mmol) afforded the product as a yellow solid (183 mg, 25%). mp: 116−118 °C. $^1$H NMR (300 MHz, DMSO-$d_6$) $\delta$ 7.20 (d, $J$ = 7.9 Hz, 1H), 6.81 (t, $J$ = 7.6 Hz, 1H), 5.22 (s, 2H), 2.93 (t, $J$ = 7.6 Hz, 2H), 2.77 (t, $J$ = 7.5 Hz, 2H), 1.93 (dd, $J$ = 7.4, 3.2 Hz, 2H), 1.24 (s, 12H). MS $m/z$ (ESI) [M + H]$^+$: 260.5.

**4-(7-Amino-2,3-dihydro-1*H*-inden-4-yl)benzo[*d*]isoxazol-3-amine (B-19c).** Following the synthetic protocol for intermediate **B-1a**, a reaction of **B-19b** (183 mg, 0.704 mmol) and 4-bromobenzo-[*d*]isoxazol-3-amine (100 mg, 0.469 mmol) afforded the product as a yellow solid (50 mg, 41%). mp: 100−102 °C. MS $m/z$ (ESI) [M + H]$^+$: 266.3.

**1-(7-(3-Aminobenzo[*d*]isoxazol-4-yl)-2,3-dihydro-1*H*-inden-4-yl)-3-(3-(trifluoromethoxy)phenyl)urea (19).** Following the synthetic protocol for compound 4, a reaction of **B-19c** (50 mg, 0.188 mmol) and 3-(trifluoromethoxy)aniline (72 mg, 0.408 mmol) afforded the product as a white solid (20 mg, 23%). mp: 190−192 °C; HPLC analysis, retention time, 4.456 min; peak area, 96.10%. $^1$H NMR (300 MHz, DMSO-$d_6$) $\delta$ 9.38 (s, 1H), 8.27 (s, 1H), 7.96 (d, $J$ = 8.2 Hz, 1H), 7.76 (s, 1H), 7.58 (dd, $J$ = 8.4, 7.1 Hz, 1H), 7.53−7.37 (m, 2H), 7.34−7.25 (m, 1H), 7.10 (t, $J$ = 7.0 Hz, 2H), 6.97 (dd, $J$ = 8.1, 2.2 Hz, 1H), 5.06 (s, 2H), 2.92 (s, 2H), 2.73 (s, 2H), 2.05 (s, 2H). HRMS-ESI $m/z$ [M + H]$^+$ calcd for $C_{24}H_{20}F_3N_4O_3$: 469.1482, found: 469.1471.

**7-Amino-4-bromo-2,3-dihydro-1*H*-inden-1-one (B-20a).** Following the synthetic protocol for intermediate **B-19a**, a reaction of 7-amino-2,3-dihydro-1*H*-inden-1-one (500 mg, 3.40 mmol) and N-bromosuccinimide (605 mg, 3.40 mmol) afforded the product as a yellow solid (560 mg, 91%). mp: 121−124 °C. $^1$H NMR (300 MHz, DMSO-$d_6$) $\delta$ 7.43 (d, $J$ = 8.7 Hz, 1H), 6.76 (s, 2H), 6.54 (d, $J$ = 8.7 Hz, 1H), 2.91−2.82 (m, 2H), 2.67−2.58 (m, 2H). MS $m/z$ (ESI) [M + H]$^+$: 182.7.

**7-Amino-4-(4,4,5,5-tetramethyl-1,3,2-dioxaborolan-2-yl)-2,3-dihydro-1*H*-inden-1-one (B-20b).** Following the synthetic protocol for intermediate **B-11a**, a reaction of **B-20a** (560 mg, 3.08 mmol) and bis(pinacolato)diboron (1.17 g, 4.62 mmol) afforded the product as a yellow solid (193 mg, 23%). mp: 110−113 °C. $^1$H NMR (300 MHz, DMSO-$d_6$) $\delta$ 7.54 (d, $J$ = 8.2 Hz, 1H), 6.96 (s, 2H), 6.52−6.46 (m, 1H), 3.10−3.03 (m, 2H), 2.57−2.52 (m, 2H), 1.17 (s, 12H). MS $m/z$ (ESI) [M + H]$^+$: 274.5.

**7-Amino-4-(3-aminobenzo[*d*]isoxazol-4-yl)-2,3-dihydro-1*H*-inden-1-one (B-20c).** Following the synthetic protocol for intermediate **B-1a**, a reaction of **B-20b** (193 mg, 0.707 mmol) and 4-bromobenzo[*d*]isoxazol-3-amine (100 mg, 0.469 mmol) afforded the product as a yellow oil (100 mg, 76.3%). $^1$H NMR (300 MHz, DMSO-$d_6$) $\delta$ 7.47 (dd, $J$ = 8.4, 0.9 Hz, 1H), 7.28−7.18 (m, 2H), 7.11 (dd, $J$ = 7.2, 0.9 Hz, 1H), 6.84 (s, 2H), 6.66 (d, $J$ = 8.3 Hz, 1H), 5.12 (s, 2H), 2.77 (s, 2H), 2.54 (d, $J$ = 5.7 Hz, 2H). MS $m/z$ (ESI) [M + H]$^+$: 280.3.

**1-(7-(3-Aminobenzo[*d*]isoxazol-4-yl)-3-oxo-2,3-dihydro-1*H*-inden-4-yl)-3-(3-(trifluoromethoxy)phenyl)urea (20).** Following the synthetic protocol for compound 4, a reaction of **B-20c** (100 mg, 0.358 mmol) and 3-(trifluoromethoxy)aniline (76 mg, 0.43 mmol) afforded the product as a white solid (33 mg, 19%). mp: 142−144 °C.$^1$H NMR (300 MHz, DMSO-$d_6$) $\delta$ 10.45 (s, 1H), 10.00 (s, 1H), 8.37 (d, $J$ = 8.5 Hz, 1H), 7.75 (s, 1H), 7.62−7.48 (m, 3H), 7.48−7.36 (m, 2H), 7.16 (d, $J$ = 7.0 Hz, 1H), 6.99 (d, $J$ = 7.4 Hz, 1H), 5.18 (s, 2H), 2.87 (s, 2H), 2.69 (t, $J$ = 5.6 Hz, 2H). HRMS-ESI $m/z$ [M + H]$^+$ calcd for $C_{24}H_{18}F_3N_4O_4$: 483.1275, found: 483.1275.

## Assessment of Inhibitory Activity against Kinase

The inhibitory activities of the synthesized compounds against RIPK1 kinase were evaluated using the ADP-Glo Kinase Assay kit (Promega, V9101), with RIPA-56 (MCE, HY-101032) employed as a positive control. The assay was performed in 384-well optiplates (PE, OptiPlate 384). Compounds were transferred acoustically (LABCYTE Echo 655) at 0.05 $\mu$L per well and serially diluted 3-fold across ten concentrations, with two replicates per concentration. Then, 5 $\mu$L of enzyme working solution was added to each well, followed by centrifugation at 1000 rpm for 1 min and incubation at 25 °C for 10 min. The reaction was initiated by adding 5 $\mu$L of ATP working solution and incubated at 25 °C for 240 min. Subsequently, 5 $\mu$L of ADP-Glo reagent was added and incubated for 40 min, followed by the addition of 10 $\mu$L of detection reagent and further incubation for 40 min. Luminescence signals were measured using a PHERAstar FSX microplate reader (BMG). Dose−response curves were fitted and $IC_{50}$ values were calculated using GraphPad Prism software.

## Assessment of Antinecroptotic Activity

In this study, a TSZ-induced necroptosis model was employed to evaluate the antinecroptotic activity of RIPK1 inhibitors. HT-29 cells were seeded in 384-well plates and allowed to adhere overnight. The cells were then treated with a necroptosis-inducing cocktail consisting of TSZ. After 30 min of TSZ stimulation, test compounds diluted in a series of concentrations were added, followed by further incubation for 24 h. Cell viability was assessed using the CCK-8 assay: CCK-8 reagent was added to each well, and after incubation, the absorbance at 450 nm was measured using a microplate reader. The $EC_{50}$ values were calculated using GraphPad Prism software to determine the potency of the compounds in inhibiting necroptosis.

## Assessment of Antiproliferative Activity

To assess the potential cytotoxicity of the compounds, an antiproliferation assay was further conducted. Human colorectal cancer


https://doi.org/10.1021/acs.jmedchem.5c03775
J. Med. Chem. XXXX, XXX, XXX−XXX

HT-29 cells or human embryonic kidney HEK 293T cells were seeded in 384-well plates and cultured overnight to allow adhesion. The cells were then treated with serially diluted compounds and incubated for 72 h. Cell proliferation was evaluated using the CCK-8 assay: CCK-8 reagent was added to each well, and after incubation, the absorbance at 450 nm was measured. Dose−response curves were generated and $IC_{50}$ values were calculated using GraphPad Prism software to evaluate the compounds' ability to inhibit cell proliferation.

## Kinase Profiling Assay

Test compounds were prepared in DMSO and dispensed into 384-well plates using acoustic liquid handling. The enzymatic activity of the target kinases was assessed using both HTRF and ADP-Glo detection technologies, following the respective optimized buffer conditions and standard incubation protocols for each platform. All fluorescence and luminescence signals were measured using a PHERAstar plate reader. The percentage inhibition for each compound was calculated relative to DMSO (negative control) and a known reference inhibitor (positive control).

## Pharmacokinetic Study of Compound 30 in Pats

The pharmacokinetic profile of compound **30** was evaluated in healthy male Sprague−Dawley rats randomly assigned to receive either an intravenous injection (1 mg/kg) or an oral administration (10 mg/kg). Blood samples were collected at predetermined time points postdosing, and the plasma concentration of the compound was determined using LC-MS/MS. Key pharmacokinetic parameters were subsequently calculated by analyzing the concentration−time data with a non-compartmental model via Phoenix WinNonlin software.

## Metabolic Stability Assessment of Compound 30 in Liver Microsomes

The metabolic stability of Compound **30** was assessed using an in vitro liver microsomal incubation system. The compound was incubated with rat or human liver microsomes at 37 °C in the presence of the cofactor NADPH. Samples were taken at various time points, and the remaining amount of the parent compound was quantified by LC-MS/MS. The *in vitro* half-life ($t_{1/2}$) and intrinsic clearance (CLint) were determined from the depletion curve to evaluate its metabolic stability.

## Acute Toxicity Test

The acute toxicity evaluation was carried out in ICR mice from Jiangsu Qinglongshan Biotechnology Co., Ltd. The mice were divided into (n = 6, randomly half male and half female for each group) the blank, vehicle control and treatment groups. After a 12-h fasting and no-water period, the tested compound was treated. The compound solution was prepared in a vehicle of 5% DMSO, 5% Tween 80 and 90% physiological saline. The treatment group received a single dose of 400 mg/kg by gavage, and other two groups were fed the saline and vehicle without the tested compound, respectively. General conditions of the mice such as skin color, fur color, breathing, secretions from the orifices, behavior activities, feeding, defecation and body weight were monitored daily thereafter for 14 days. At the end of the observation period, surviving animals were euthanized humanely with the aid of isoflurane for gross necropsy to identify any internal organ abnormalities. Then, the heart, spleen, liver, lungs and kidneys were collected, fixed (4% formalin), and stained with hematoxylin-eosin (HE) for histopathology analysis.

## Animals and Oncomelania Snails

Female C57BL/6 mice (SPF grade, 5−6 weeks old, 20 g) were purchased from SPF (Suzhou) Biotechnology Co., Ltd. *Schistosoma japonicum* (Jiangsu strain)-infected positive *Oncomelania hupensis* snails were provided by the Snail Room of the Jiangsu Institute of Parasitic Diseases. The animal experimental protocol involved in this study was reviewed and approved by the Experimental Animal Use and Management Ethics Committee of the Jiangsu Institute of Parasitic Diseases (Approval No.: JIPD-2023−010). All animals were housed and handled in accordance with animal experimental ethics.

## Establishment of Mouse Infection Model and Treatment Regimens

Forty-six C57BL/6 mice were divided into eight groups (healthy controls n = 5, other groups n = 6) to test intraperitoneal (5 and 10 mg/kg) and oral (50 and 100 mg/kg) administration of compound **30**. All mice except healthy controls were infected percutaneously with 15 ± 1 *S. japonicum* cercariae. At 5 weeks postinfection, parasites were cleared with praziquantel (250 mg/kg, oral gavage), followed by a 4-week regimen of **30**. After treatment, adult worms were harvested by perfusion. Livers were digested in 5% KOH for egg counting. The liver and spleen were weighed to calculate organ indices (organ weight/body weight × 100%). Body weight was recorded weekly.

## Serum Levels of Alanine Aminotransferase (ALT) and Aspartate Aminotransferase (AST) in Mice

After treating schistosome-infected mice with the above regimens, blood was collected via the submandibular method and stored overnight at 4 °C. Serum was collected by centrifugation at 2000× g. Serum levels of ALT and AST were detected using detection kits from Jiancheng Bioengineering Institute (Nanjing, China).

## Histopathological Sections

The right lobe of the liver was collected during dissection, fixed in 4% paraformaldehyde, and routinely dehydrated and embedded to prepare 4 $\mu$m sections. After deparaffinization and rehydration, sections were stained using HE and Masson staining kits from Science & Technology Co.,Ltd. (Beijing, China). At least five single egg granulomas were randomly selected from each mouse. And the area of a single egg granuloma was calculated using cellSens software after imaging with a microscope. At least five images were captured from each mouse and the percentage of collagen fiber area (the collagen area/total area) in the liver was calculated using ImageJ.

## Hepatic Hydroxyproline Content

Approximately 100 mg of liver tissue from each group was taken, and the hydroxyproline content in the liver was detected using a hydroxyproline detection kit from Jiancheng Bioengineering Institute (Nanjing, China) to reflect the collagen level in the liver.

## Hepatic Reactive Oxygen Species (ROS) Content

Approximately 50 mg of liver tissue from each mouse was fully homogenized, and the supernatant was taken. The level of ROS in the liver was detected using a kit probe method (Bestbio Biotechnology, Shanghai, China). The fluorescence intensity was measured using a microplate reader at an excitation wavelength of 488 nm and an emission wavelength of 530 nm. Another aliquot of the homogenate supernatant was taken for protein quantification using the BCA method. Tissue ROS intensity was calculated as fluorescence intensity (RFU)/protein concentration (mg protein) for normalization, removing the influence of sample size.

## Western Blot

Mouse liver tissues were taken from −80 °C and homogenized in RIPA lysis buffer containing protease inhibitors on ice. The homogenate was centrifuged at 12,000 rpm for 15 min at 4 °C to collect the supernatant. Protein concentration was determined using the BCA method. 30−100 $\mu$g of protein was taken for SDS-PAGE electrophoresis. After electrophoresis, proteins were transferred to a PVDF membrane. After transfer, the PVDF membrane was blocked with 5% skim milk at room temperature for 1 h, followed by incubation with primary antibodies against Collagen I, $\alpha$-SMA, RIPK1, RIPK3, MLKL, p-RIPK1, p-RIPK3, p-MLKL, Caspase 3, AKT, p-AKT, PI3K, p-PI3K, P65, p-P65, TNF-$\alpha$, F4/80 (Dilution ratio 1:3000, CST, Boston, USA) at 4 °C overnight. The membrane was washed with PBST (3 × 10 min). Then, it was incubated with an antirabbit secondary antibody (1:4000) at room temperature for 1 h, followed by PBST washes (3 × 10 min). The membrane was incubated with ECL substrate for 5 s, and images were captured using a chemiluminescence instrument (Bio-Rad, California, USA).


https://doi.org/10.1021/acs.jmedchem.5c03775
J. Med. Chem. XXXX, XXX, XXX−XXX

### PCR Array

Approximately 100 mg of liver tissue from each group was taken. Total RNA was extracted from the liver using TRIzol method. RNA was reverse-transcribed into cDNA using a first-strand cDNA synthesis kit (Vazyme, Nanjing, China). A high-throughput Mouse Inflammatory Cytokines & Receptors PCR Array plate (96-well, WC-MRNA0266-M, WcGene Biotech, Shanghai, China) was used to detect the relative mRNA expression levels of 90 target inflammatory factors and chemokines in liver tissue via qPCR. Subsequently, differential analysis of the mRNA expression levels of inflammatory factors and chemokines, and KEGG pathway analysis were performed.

### Transcriptome Sequencing

Approximately 100 mg of liver tissue was taken from the healthy control mice, *S. japonicum* infected mice, and *S. japonicum* infected mice treated with 100 mg/kg oral gavage (n = 3 mice per group). Samples were sent to Genedenovo Biotechnology Co., Ltd. (Guangzhou, China) for transcriptome sequencing. Differential gene expression analysis, GO enrichment analysis, and KEGG pathway analysis were performed.

### Detection of Cytokine Levels in Splenocyte Culture Supernatants

Spleens were taken from each mouse to prepare single-cell suspensions. Cells were seeded at $6 \times 10^5$ cells per well and stimulated with soluble egg antigen (SEA,10 $\mu$g/mL) for 72 h. Cell culture supernatants were collected, and the levels of TNF-$\alpha$, IL-17, IL-4, and IFN-$\gamma$ in the supernatants were detected using ELISA kits (Muti sciences Biotech, Hangzhou, China).

### Statistical Analysis

One-way analysis of variance (ANOVA) was used for comparisons among multiple groups in the experiments, and the *t* test was used for comparisons between two groups. GraphPad Prism 9.0 software was used for graphing, and IBM SPSS Statistics 25 software was used for statistical analysis. A *P*-value <0.05 was considered statistically significant.

### Molecular Docking and Conformation Preparation

The three-dimensional structure of **30** was generated and energy-minimized using the LigPrep module in Maestro 12.8. The crystal structures of the target proteins, RIPK1 (PDB: 4NEU) and RIPK3 (PDB: 7M3J), were retrieved from the Protein Data Bank. Each protein structure was prepared using the Protein Preparation Wizard module in Maestro 12.8, which included the removal of nonessential protein chains, residues, water molecules (except those critical for binding), and metal ions, followed by energy optimization. The optimized ligand then underwent Induced Fit Docking with the prepared protein structures. The highest-scoring conformation from each docking simulation was selected for subsequent molecular dynamics studies.

### Molecular Dynamics Simulation

All MD simulations and binding free energy calculations were performed using the AMBER 22. The simulation system was constructed with the tleap module, employing the ff99SB force field for the protein, the GAFF force field for the ligand, and the TIP3P model for water molecules. Counterions ($Na^+$ and $Cl^-$) were added to neutralize the system. Following system setup, restrained solvent minimization was conducted using 5000 steps of steepest descent followed by 5000 steps of conjugate gradient, after which the entire system was minimized. The system was then gradually heated to the target temperature over 2 ns under the NVT, followed by 5 ns of equilibration under the NPT. Production simulations were carried out for 500 ns under the NPT, with temperature controlled by Langevin dynamics and pressure regulated using the Berendsen barostat. A cutoff distance of 10.0 Å was applied for nonbonded interactions, and long-range electrostatic interactions were treated with the Particle Mesh Ewald (PME) method. Trajectory frames were saved every 2 ps for subsequent analysis.

### Binding Free Energy Calculation

The binding free energy of the ligand to RIPK1 was calculated using the MM/GBSA (Molecular Mechanics/Generalized Born Surface Area) method based on equilibrated trajectories extracted from the production simulation. A total of 2501 snapshots were uniformly extracted from the last 50 ns of the 500 ns trajectory for energy calculations. The GBneck2 model (igb = 5) was employed with a salt concentration of 0.10 M. The nonpolar solvation energy contribution was estimated using the LCPO method. In addition, per-residue energy decomposition was performed to evaluate the contribution of individual protein residues to the binding free energy.

### In Silico ADME Prediction

The membrane permeability of key compounds was predicted using the QikProp module (Schrödinger). Compounds were prepared using LigPrep and their properties were calculated in the normal mode. Predicted apparent Caco-2 cell permeability (QPPCaco) and MDCK cell permeability (QPPMDCK) were used as indicators of passive transcellular diffusion. The free energy of insertion into a neutral membrane (Membrane dG Insert) was also analyzed.

## ■ ASSOCIATED CONTENT

### Supporting Information

The Supporting Information is available free of charge at https://pubs.acs.org/doi/10.1021/acs.jmedchem.5c03775.

Predicted ADME properties for compounds **4**, **10**, **11**, **15**, and **30**; kinase panel selectivity of compound **30**; primary metabolites of compound **30** in rats; low-dose oral compound **30** and praziquantel on *S. japonicum*-induced hepatic injury and fibrosis in mice; RMSF/RMSD of compound **30** and RIPK1/3; NMR spectra, HRMS spectra and HPLC traces for all final compounds (PDF)

Molecular string file for all the final compounds (CSV)

Conformation of compound **30** in the final frame of the 500 ns molecular dynamics simulation with RIPK1 (PDB)

Conformation of compound **30** in the final frame of the 500 ns molecular dynamics simulation with RIPK3 (PDB)

## ■ AUTHOR INFORMATION


### Corresponding Authors

**Ya-Dong Chen** − *Laboratory of Molecular Design and Drug Discovery, China Pharmaceutical University, Nanjing 211198, P.R. China*; Email: chenyadong@gmail.com

**Li-Jun Song** − *National Health Commission Key Laboratory of Parasitic Disease Control and Prevention, Jiangsu Provincial Key Laboratory on Parasite and Vector Control Technology, Jiangsu Provincial Medical Key Laboratory, Jiangsu Institute of Parasitic Diseases, Wuxi 214064, P.R. China*; orcid.org/0000-0002-3897-5925; Email: songlijun@jipd.com

**Shuai Lu** − *School of Science, China Pharmaceutical University, Nanjing 211198, P.R. China*; orcid.org/0000-0002-0169-349X; Email: lu_shuai@cpu.edu.cn

### Authors

**Ju-Lu Lu** − *National Health Commission Key Laboratory of Parasitic Disease Control and Prevention, Jiangsu Provincial Key Laboratory on Parasite and Vector Control Technology, Jiangsu Provincial Medical Key Laboratory, Jiangsu Institute of Parasitic Diseases, Wuxi 214064, P.R. China*

**Qin-Di He** − *School of Science, China Pharmaceutical University, Nanjing 211198, P.R. China*




https://doi.org/10.1021/acs.jmedchem.5c03775
J. Med. Chem. XXXX, XXX, XXX−XXX

**Yi-Han Yang** − *School of Science, China Pharmaceutical University, Nanjing 211198, P.R. China*
**Jing-Ping Li** − *National Health Commission Key Laboratory of Parasitic Disease Control and Prevention, Jiangsu Provincial Key Laboratory on Parasite and Vector Control Technology, Jiangsu Provincial Medical Key Laboratory, Jiangsu Institute of Parasitic Diseases, Wuxi 214064, P.R. China*
**Si-Rui Mo** − *School of Pharmacy, Youjiang Medical University for Nationalities, Baise 533000, P.R. China*
**Li Liang** − *School of Science, China Pharmaceutical University, Nanjing 211198, P.R. China*
**Ya-Qi Zhang** − *School of Science, China Pharmaceutical University, Nanjing 211198, P.R. China*
**Si-Ming Jia** − *School of Science, China Pharmaceutical University, Nanjing 211198, P.R. China*
**Zi-Tian Cheng** − *School of Science, China Pharmaceutical University, Nanjing 211198, P.R. China*
**Jie Cheng** − *School of Science, China Pharmaceutical University, Nanjing 211198, P.R. China*
**Pei Yang** − *School of Science, China Pharmaceutical University, Nanjing 211198, P.R. China*
**Hong-Mei Li** − *School of Science, China Pharmaceutical University, Nanjing 211198, P.R. China*
**Tao Lu** − *State Key Laboratory of Natural Medicines, China Pharmaceutical University, Nanjing 210009, P.R. China*

Complete contact information is available at: https://pubs.acs.org/10.1021/acs.jmedchem.5c03775

### Author Contributions

#J.-L.L., Q.-D.H., Y.-H.Y., and J.-P.L. contributed equally to this work.

### Notes

The authors declare no competing financial interest.

## ■ ACKNOWLEDGMENTS

This work was supported by the Natural Science Foundation of Jiangsu Province and Guangxi Zhuang Autonomous Region (BK20231482 and 2025GXNSFAA069097), Key Projects of Jiangsu Provincial Health Commission (K2023042), Jiangsu Province Capability Improvement Project through Science, Technology, and Education (ZDXYS202207), and Qinglan Project of Jiangsu province for financial support (for S.L.). Y.Z. appreciates the National Innovation and Entrepreneurship Training Program for Undergraduate (202510316040). We acknowledge the Public Platform of Basic Chemical Experimental Center of the School of Science, and also thank P. Yang for the technical support. BioRender.com was used to create the graphical abstract and other schematic figures in this manuscript.

## ■ ABBREVIATIONS

$\alpha$-SMA,alpha-smooth muscle actin; ALT,alanine aminotransferase; AST,aspartate aminotransferase; CCK-8,Cell Counting Kit-8; CL,clearance; Clint,intrinsic clearance; Cmax,maximum concentration; Ctr,control; DAMPs,damage-associated molecular patterns; ECM,extracellular matrix; ELISA,enzyme-linked immunosorbent assay; F,bioavailability; HATU,1-[bis-(dimethylamino)methylene]-1*H*-1,2,3-triazolo[4,5-*b*]-pyridinium 3-oxide hexafluorophosphate; H&E,hematoxylin and eosin; HSCs,hepatic stellate cells; IC50,half-maximal inhibitory concentration; IL,interleukin; i.p.,intraperitoneal; i.v.,intravenous; KEGG,Kyoto Encyclopedia of Genes and Genomes; LC-MS/MS,liquid chromatography−tandem mass spectrometry; MD,molecular dynamics; MLKL,mixed lineage kinase domain-like protein; MM/GBSA,molecular mechanics/generalized Born surface area; MMP,matrix metalloproteinase; NMR,nuclear magnetic resonance; PI3K,phosphoinositide 3-kinase; p.o.,per os (oral administration); PVDF,polyvinylidene fluoride; RFU,relative fluorescence units; RIPK1,receptor-interacting protein kinase 1; RIPK3,receptor-interacting protein kinase 3; RMSD,root-mean-square deviation; ROS,reactive oxygen species; SAR,structure−activity relationship; SEA,soluble egg antigen; TGF-$\beta$,transforming growth factor beta; Tmax,time to maximum concentration; TNF-$\alpha$,tumor necrosis factor alpha; TSZ,TNF$\alpha$/Smac-mimetic/z-VAD-FMK

## ■ REFERENCES

(1) Taru, V.; Szabo, G.; Mehal, W.; Reiberger, T. Inflammasomes in chronic liver disease: Hepatic injury, fibrosis progression and systemic inflammation. *J. Hepatol.* **2024**, *81* (5), 895−910.
(2) Aydin, M. M.; Akçalı, K. C. Liver fibrosis. *Turk. J. Gastroenterol.* **2018**, *29* (1), 14−21.
(3) Rombouts, B.; van der Wijst, E.; Schoeters, P.; Driessen, A.; Steinhauser, T.; Vanwolleghem, T.; Kwanten, W.; Derdeyn, J.; Vonghia, L.; Francque, S. Unexplained portal hypertension and confusion in an elderly patient: a late presentation of congenital hepatic fibrosis. *Acta Gastroenterol. Belg.* **2025**, *88* (1), 75−78.
(4) Roehlen, N.; Crouchet, E.; Baumert, T. F. Liver Fibrosis: Mechanistic Concepts and Therapeutic Perspectives. *Cells* **2020**, *9* (4), 875.
(5) Pasparakis, M.; Vandenabeele, P. Necroptosis and its role in inflammation. *Nature* **2015**, *517* (7534), 311−320.
(6) Meier, P.; Legrand, A. J.; Adam, D.; Silke, J. Immunogenic cell death in cancer: targeting necroptosis to induce antitumour immunity. *Nat. Rev. Cancer* **2024**, *24* (5), 299−315.
(7) Ermolaeva, M. A.; Michallet, M. C.; Papadopoulou, N.; Utermöhlen, O.; Kranidioti, K.; Kollias, G.; Tschopp, J.; Pasparakis, M. Function of TRADD in tumor necrosis factor receptor 1 signaling and in TRIF-dependent inflammatory responses. *Nat. Immunol.* **2008**, *9* (9), 1037−1046.
(8) Mifflin, L.; Ofengeim, D.; Yuan, J. Y. Receptor-interacting protein kinase 1 (RIPK1) as a therapeutic target. *Nat. Rev. Drug Discovery* **2020**, *19* (8), 553−571.
(9) Murphy, J. M.; Czabotar, P. E.; Hildebrand, J. M.; Lucet, I. S.; Zhang, J. G.; Alvarez-Diaz, S.; Lewis, R.; Lalaoui, N.; Metcalf, D.; Webb, A. I.; et al. The Pseudokinase MLKL Mediates Necroptosis via a Molecular Switch Mechanism. *Immunity* **2013**, *39* (3), 443−453.
(10) Coulouarn, C.; Corlu, A.; Glaise, D.; Guénon, I.; Thorgeirsson, S. S.; Clément, B. Hepatocyte-Stellate Cell Cross Talk in the Liver Engenders a Permissive Inflammatory Microenvironment That Drives Progression in Hepatocellular Carcinoma. *Cancer Res.* **2012**, *72* (10), 2533−2542.
(11) Kim, J. W.; Kim, Y. J. The evidence-based multifaceted roles of hepatic stellate cells in liver diseases: A concise review. *Life Sci.* **2024**, No. 122547.
(12) Yan, M. C.; Xie, Y.; Yao, J.; Li, X. The Dual-Mode Transition of Myofibroblasts Derived from Hepatic Stellate Cells in Liver Fibrosis. *Int. J. Mol. Sci.* **2023**, *24* (20), 15469.
(13) Wang, Y.; Jiao, L.; Qiang, C.; Chen, C.; Shen, Z.; Ding, F.; Lv, L.; Zhu, T.; Lu, Y.; Cui, X. The role of matrix metalloproteinase 9 in fibrosis diseases and its molecular mechanisms. *Biomed. Pharmacother.* **2024**, No. 116116.
(14) Antar, S. A.; Ashour, N. A.; Marawan, M. E.; Al-Karmalawy, A. A. Fibrosis: Types, Effects, Markers, Mechanisms for Disease Progression, and Its Relation with Oxidative Stress, Immunity, and Inflammation. *Int. J. Mol. Sci.* **2023**, *24* (4), 4004.
(15) Xu, L. J.; Zhang, W. N.; Zhuang, C. L. Receptor-interacting protein kinase 1 (RIPK1) inhibitor: a review of the patent literature (2018-present). *Expert Opin. Ther. Pat.* **2023**, *33* (2), 101−124.

(16) Seo, J.; Nam, Y. W.; Kim, S.; Oh, D. B.; Song, J. Necroptosis molecular mechanisms: Recent findings regarding novel necroptosis regulators. *Exp. Mol. Med.* **2021**, *53* (6), 1007−1017.
(17) Patel, S.; Chen, H. F.; Varfolomeev, E.; Kwon, Y.; Ramaswamy, S.; Kohli, P. B.; Quinn, J. G.; Webster, J. D.; Mac, J. L.; Chen, Y.; et al. Discovery of Clinical Candidate GDC-8264, a Novel, Potent and Selective RIP1 Inhibitor for Amelioration of Tissue Damage and the Treatment of Inflammatory Diseases. *J. Med. Chem.* **2025**, *68*, 23050.
(18) Fang, J. J.; Yao, H. Z.; Zhuang, C. L.; Chen, F. E. Insight from Linker Investigations: Discovery of a Novel Phenylbenzothiazole Necroptosis Inhibitor Targeting Receptor-Interacting Protein Kinase 1 (RIPK1) from a Phenoxybenzothiazole Compound with Dual RIPK1/3 Targeting Activity. *J. Med. Chem.* **2023**, *66* (22), 15288−15308.
(19) Hofmans, S.; Devisscher, L.; Martens, S.; Van Rompaey, D.; Goossens, K.; Divert, T.; Nerinckx, W.; Takahashi, N.; De Winter, H.; Van der Veken, P.; et al. Tozasertib Analogues as Inhibitors of Necroptotic Cell Death. *J. Med. Chem.* **2018**, *61* (5), 1895−1920.
(20) Harris, P. A.; Bandyopadhyay, D.; Berger, S. B.; Campobasso, N.; Capriotti, C. A.; Cox, J. A.; Dare, L.; Finger, J. N.; Hoffman, S. J.; Kahler, K. M.; et al. Discovery of Small Molecule RIP1 Kinase Inhibitors for the Treatment of Pathologies Associated with Necroptosis. *ACS Med. Chem. Lett.* **2013**, *4* (12), 1238−1243.
(21) Hou, J.; Ju, J.; Zhang, Z. L.; Zhao, C.; Li, Z. H.; Zheng, J. Y.; Sheng, T.; Zhang, H. J.; Hu, L. K.; Yu, X. L.; et al. Discovery of potent necroptosis inhibitors targeting RIPK1 kinase activity for the treatment of inflammatory disorder and cancer metastasis. *Cell Death Dis.* **2019**, *10*, 493.
(22) Li, Y. S.; Xiong, Y.; Zhang, G.; Zhang, L. T.; Yang, W.; Yang, J.; Huang, L. Y.; Qiao, Z.; Miao, Z.; Liu, G. F.; et al. Identification of 5-(2,3-Dihydro-1H-indol-5-yl)-7H-pyrrolo[2,3-*d*]pyrimidin-4-amine Derivatives as a New Class of Receptor-Interacting Protein Kinase 1 (RIPK1) Inhibitors, Which Showed Potent Activity in a Tumor Metastasis Model. *J. Med. Chem.* **2018**, *61* (24), 11398−11414.
(23) Degterev, A.; Huang, Z. H.; Boyce, M.; Li, Y. Q.; Jagtap, P.; Mizushima, N.; Cuny, G. D.; Mitchison, T. J.; Moskowitz, M. A.; Yuan, J. Y. Chemical inhibitor of nonapoptotic cell death with therapeutic potential for ischemic brain injury. *Nat. Chem. Biol.* **2005**, *1* (2), 112−119.
(24) Wang, Z. W.; Zou, F. M.; Wang, A. L.; Yang, J.; Jin, R.; Wang, B. L.; Shen, L. J.; Qi, S.; Liu, J.; Liu, J.; et al. Repurposing of the FGFR inhibitor AZD4547 as a potent inhibitor of necroptosis by selectively targeting RIPK1. *Acta Pharmacol. Sin.* **2023**, *44* (4), 801−810.
(25) Li, Y. S.; Zhang, L. T.; Wang, Y. F.; Zou, J.; Yang, R. C.; Luo, X. L.; Wu, C. Y.; Yang, W.; Tian, C. Y.; Xu, H. X.; et al. Generative deep learning enables the discovery of a potent and selective RIPK1 inhibitor. *Nat. Commun.* **2022**, *13* (1), 6891.
(26) Yu, X. L.; Ma, H. K.; Li, B. H.; Ji, Y. T.; Du, Y. Y.; Liu, S. Y.; Li, Z. H.; Hao, Y. J.; Tian, S.; Zhao, C.; et al. A novel RIPK1 inhibitor reduces GVHD in mice via a nonimmunesuppressive mechanism that restores intestinal homeostasis. *Blood* **2023**, *141* (9), 1070−1086.
(27) Chen, X.; Zhuang, C.; Ren, Y.; Zhang, H.; Qin, X.; Hu, L.; Fu, J.; Miao, Z.; Chai, Y.; Liu, Z.; Zhang, H.; Cai, Z.; Wang, H.; et al. Identification of the Raf kinase inhibitor TAK-632 and its analogues as potent inhibitors of necroptosis by targeting RIPK1 and RIPK3. *Br. J. Pharmacol.* **2019**, *176* (12), 2095−2108.
(28) Tao, Q. Q.; Li, X. X.; Yu, H. W.; Zou, F. M.; Liu, J.; Liu, Q. W.; Wang, A. L.; Hu, C.; Wang, L.; Wang, W. C.; et al. Discovery of a 1*H*-Pyrazol-3-Amine Derivative as a Novel, Selective, and Orally Available RIPK1 Inhibitor for the Treatment of Inflammatory Disease. *J. Med. Chem.* **2025**, *68* (20), 21766−21785.
(29) Song, L. J.; Yin, X. R.; Guan, S. W.; Gao, H.; Dong, P. P.; Mei, C. J.; Yang, Y. Y.; Zhang, Y.; Yu, C. X.; Hua, Z. C. RIP3 deficiency attenuated hepatic stellate cell activation and liver fibrosis in schistosomiasis through JNK-cJUN/Egr1 downregulation. *Signal Transduct. Target. Ther.* **2022**, *7* (1), 193.
(30) Lei, Z. G.; Zhou, S.; Su, C.; Wu, G. L. Mechanisms underlying persistent liver fibrosis progression in Schistosoma-infected individuals post-treatment. *Infect. Dis. Poverty* **2025**, *14* (1), 78.
(31) Buonfrate, D.; Ferrari, T. C. A.; Adegnika, A. A.; Russell Stothard, J.; Gobbi, F. G. Human schistosomiasis. *Lancet* **2025**, *405* (10479), 658−670.
(32) Kamdem, S. D.; Moyou-Somo, R.; Brombacher, F.; Nono, J. K. Host Regulators of Liver Fibrosis During Human Schistosomiasis. *Front. Immunol.* **2018**, *9*, 2781.
(33) Lawlor, K. E.; Khan, N.; Mildenhall, A.; Gerlic, M.; Croker, B. A.; D'Cruz, A. A.; Hall, C.; Kaur Spall, S.; Anderton, H.; Masters, S. L.; Rashidi, M.; Wicks, I. P.; Alexander, W. S.; Mitsuuchi, Y.; Benetatos, C. A.; Condon, S. M.; Wong, W. W. L.; Silke, J.; Vaux, D. L.; Vince, J. E.; et al. RIPK3 promotes cell death and NLRP3 inflammasome activation in the absence of MLKL. *Nat. Commun.* **2015**, *6*, 6282.
(34) Degterev, A.; Ofengeim, D.; Yuan, J. Y. Targeting RIPK1 for the treatment of human diseases. *Proc. Natl. Acad. Sci. U. S. A.* **2019**, *116* (20), 9714−9722.
(35) Shi, Z. H.; Liu, F. T.; Tian, H. Z.; Zhang, Y. M.; Li, N. G.; Lu, T. Design, synthesis and structure-activity relationship of diaryl-ureas with novel isoxazol[3,4-*b*]pyridine-3-amino-structure as multi-target inhibitors against receptor tyrosine kinase. *Biorg. Med. Chem.* **2018**, *26* (16), 4735−4744.
(36) Shah, P.; Westwell, A. D. The role of fluorine in medicinal chemistry. *J. Enzym. Inhib. Med. Chem.* **2007**, *22* (5), 527−540.
(37) Pettersson, M.; Hou, X. J.; Kuhn, M.; Wager, T. T.; Kauffman, G. W.; Verhoest, P. R. Quantitative Assessment of the Impact of Fluorine Substitution on P-Glycoprotein (P-gp) Mediated Efflux, Permeability, Lipophilicity, and Metabolic Stability. *J. Med. Chem.* **2016**, *59* (11), 5284−5296.
(38) Song, J. Q.; Yang, R. Y.; Wei, R. Y.; Du, Y.; He, P. C.; Liu, X. W. Pan-cancer analysis reveals RIPK2 predicts prognosis and promotes immune therapy resistance via triggering cytotoxic T lymphocytes dysfunction. *Mol. Med.* **2022**, *28* (1), 47.
(39) Xia, Y.; Wang, H.; Shao, M.; Liu, X.; Sun, F. MAP3K19 Promotes the Progression of Tuberculosis-Induced Pulmonary Fibrosis Through Activation of the TGF-$\beta$/Smad2 Signaling Pathway. *Mol. Biotechnol.* **2024**, *66* (11), 3300−3310.
(40) Stammes, M. A.; Prevoo, H.; Ter Horst, M. C.; Groot, S. A.; Van de Velde, C. J. H.; Chan, A. B.; de Geus-Oei, L. F.; Kuppen, P. J. K.; Vahrmeijer, A. L.; Pasquale, E. B.; et al. Evaluation of EphA2 and EphB4 as Targets for Image-Guided Colorectal Cancer Surgery. *Int. J. Mol. Sci.* **2017**, *18* (2), 307.
(41) Katoh, M.; Loriot, Y.; Brandi, G.; Tavolari, S.; Wainberg, Z. A.; Katoh, M. FGFR-targeted therapeutics: clinical activity, mechanisms of resistance and new directions. *Nat. Rev. Clin. Oncol.* **2024**, *21* (4), 312−329.
(42) Zhang, J. C.; Yao, W.; Hashimoto, K. Brain-derived Neurotrophic Factor (BDNF)-TrkB Signaling in Inflammation-related Depression and Potential Therapeutic Targets. *Curr. Neuropharmacol.* **2016**, *14* (7), 721−731.
(43) Zhang, Q.; Wang, X. B.; Cao, S. J.; Sun, Y. J.; He, X. Y.; Jiang, B. K.; Yu, Y. Q.; Duan, J. S.; Qiu, F.; Kang, N. Berberine represses human gastric cancer cell growth in vitro and in vivo by inducing cytostatic autophagy via inhibition of MAPK/mTOR/p70S6K and Akt signaling pathways. *Biomed. Pharmacother.* **2020**, *128*, No. 110245.
(44) Gong, Q. C.; Ali, T.; Hu, Y.; Gao, R. Y.; Mou, S. N.; Luo, Y. H.; Yang, C. Y.; Li, A. X.; Li, T.; Hao, L. L.; et al. RIPK1 inhibition mitigates neuroinflammation and rescues depressive-like behaviors in a mouse model of LPS-induced depression. *Cell Commun. Signal.* **2024**, *22* (1), 427.
(45) Guo, Q.; Jin, Y. Z.; Chen, X. Y.; Ye, X. M.; Shen, X.; Lin, M. X.; Zeng, C.; Zhou, T.; Zhang, J. NF-$\kappa$B in biology and targeted therapy: new insights and translational implications. *Signal Transduct. Target. Ther.* **2024**, *9* (1), 53.
(46) Kim, D.; Leem, Y. H.; Park, J. S.; Park, J. E.; Park, J. M.; Kang, J. L.; Kim, H. S. RIPK1 Regulates Microglial Activation in Lipopolysaccharide-Induced Neuroinflammation and MPTP-Induced Parkinson's Disease Mouse Models. *Cells* **2023**, *12* (3), 417.


https://doi.org/10.1021/acs.jmedchem.5c03775
J. Med. Chem. XXXX, XXX, XXX−XXX